

PHYSICAL CHEMISTRY OF IONIC LIQUIDS: STRUCTURE AND PHOTOCHEMICAL REACTIONS

BY HEATHER YOONSOO LEE

A dissertation submitted to the
Graduate School—New Brunswick
Rutgers, The State University of New Jersey

In partial fulfillment of the requirements

For the degree of

Doctor of Philosophy

Graduate Program in Chemistry and Chemical Biology

Written under the direction of

Edward W. Castner, Jr.

Rutgers, The State University of New Jersey

and

James F. Wishart

Brookhaven National Laboratory

and approved by

New Brunswick, New Jersey

October, 2012

ABSTRACT OF THE DISSERTATION

Physical Chemistry of Ionic Liquids: Structure and Photochemical Reactions

by Heather Yoonsoo Lee

Dissertation Directors:

Edward W. Castner, Jr.

Rutgers, The State University of New Jersey

and

James F. Wishart

Brookhaven National Laboratory

Physical chemistry of ionic liquids (ILs) is investigated. First, ILs are used as solvents for photoinduced intramolecular electron-transfer (ET) reactions of a donor-bridge-acceptor compound. The solvation dynamic effect of the ILs on the intramolecular ET is compared with that in neutral solvents. The ET rates in ionic liquids are slower and very broadly distributed compared to narrowly distributed rates in the neutral solvents. In addition, the reaction kinetics in the ILs are dynamically heterogeneous. Dynamic heterogeneity, however, is not a unique quality to ILs; glass systems also show such behavior. To determine the degree to which this dynamic heterogeneity arises from, we examine the structural heterogeneity of ILs. We study the local structure of ILs using 2D NMR spectroscopy on the set of four homologous ILs. The results suggest intermolecular interactions between hydrogen atoms on the cation ether- chains and the fluorine atoms on the anions - such interaction is not found for the octyl-chained ILs. Lastly, physical and chemical properties of novel paramagnetic ionic liquids/solids are characterized. The crystal structures of these ionic compounds are solved and the magnetic properties are reported.

Acknowledgments

My path as a chemist actually started from an inorganic chemistry lab advised by **Prof. Isied**. It was through him that I got to know and work for Dr. Wishart (Brookhaven National Laboratory) who is my mentor and advisor even until today. It is also through Prof. Isied that I was introduced to my advisor and my ‘boss,’ Prof. Castner. When I wasn’t even considering applying to graduate school as a chemistry major, it was Prof. Isied who told me, “If you can play the violin as well as you do, you can do anything. I believe in you.” Thank you for pushing me to be where I am today. Thank you, Prof. Isied!

Boss, you really are THE GREATEST boss in the world. You are not just my advisor, mentor and my boss, but you became like a ‘cool dad’ to me. Perhaps, that is why sometimes I acted too comfortable around you, showing all my frustrations and emotions, and I apologize. But you, more than anyone, understood me, the sometimes crazy, blunt, overly energetic, and mood-swinging, real Heather Lee, and guided me to be where I am now. How many chemistry graduate students can say that they actually love their boss and would want to be around them? Probably not many! Thank you so much not just for your wisdom and knowledge in science but teaching me life lessons. If I can ever have a boss like you in the future, I would be the luckiest person, ever!

Dr. Wishart, your patience with me is probably one of the greatest things I am grateful for. When I broke the temperature sensor in the microwave (should I have not reminded you of that? Oops..), when my compound exploded in your TGA instrument, when I looked like a deer in a head light when you were talking to me... you kindly and patiently explained everything to me and told me everything is ok. Thank you, Dr. Wishart! I wouldn’t be here today without you.

I would like to thank my committee members, **Prof. Greenblatt** and **Prof. Case** for serving on my committee. Lots of thanks to **Dr. Murali**, for your help with my constant questions on NMR. **Prof. Herzog**, for your carbon dioxide dance that motivated me to survive through the p-chem class. Your class was the beginning of my journey in this field! **Dr. Emge**, for your ‘coolness’ in the hallway that always calms me down and, of course, for the awesome crystal structures! **Tomasz**, for those long nights of experiments and ASAP fun. Many thanks to all the co-authors in the publications for interesting discussions and insights. I would also like to thank all the scientists I met and talked to at conferences for their insightful discussions for my projects.

Joe! Your project was the inspiration for my project. So obviously, without your work (and your help... so much help!) I wouldn’t be here today. You’re seriously one of the smartest people I know. haha... I’m so lucky to have had you help me throughout this career. Thanks! Lots of thanks to **Jeremy, Jason, Ben**, and **Karen** who all have helped me many times with the laser.. especially when I came and bothered you claiming, ‘I lost the beam.’ **Tania** and **Cherry**, your presence was more than enough for me to want to come to the lab everyday. **The Castner Lab** was seriously one of the warmest, most welcoming lab, ever, because of you guys. Thanks, **Brenna**, for being an awesome lab ninja!

Mom, even though you didn’t understand why I have to go work everyday, and you still don’t know what I do... it is all because of you that I’m sanely standing here today. It is only through your constant reminder of what is most important in life that I was able to push through and be here today. I love you! **Dad**, you carried me on your back to be here since the undergraduate years. The moment I decided that I’m going to do chemistry instead of music, I knew it will be ok because I have you. Thank you and I

love you so much! **Insoo**, I tell you this all the time, but I am seriously so proud to have a sister like you. And even though you didn't read my paper (nor do I think you even tried to understand what I do), I will always be interested in what you're doing and the music you produce. I will always be your No.1 fan. Love ya!!! **Carl**, you are my 'safe place.' Without you, I don't know what I would have done when (very frequently) I was going crazy, wanted to quit, felt like crying, and felt overwhelmed with everything in my life. You're forever my Gomdolee and I will forever be your Tokki. Sarang hae!

For *Ionic Liquids and Solids with Paramagnetic Anions* project, we thank our colleagues Prof. Gene S. Hall for Raman and FT-IR spectra, Dr. Viktor Poltavets and Prof. Martha Greenblatt for SQUID magnetometer measurements, and Dr. Ashley L. Carbone and Prof. Kathryn E. Uhrich for use of their DSC instrumentation.

I thank the Graduate Assistant in Areas of National Need (GAANN) funding for 2010 academic year. I also gratefully acknowledge support from the National Science Foundation to Prof. Castner for the projects on ionic liquid structure and magnetic ionic liquids. The electron transfer work was supported by the U. S. Department of Energy Office of Basic Energy Sciences, Division of Chemical Sciences, Geosciences and Biosciences via Contract No. DE-AC02-98CH10886 with Brookhaven National Laboratory.

Jesus answered, "I am the way and the truth and the life. No one comes to the Father except through me." – John 14:6

List of Figures

1.1. Cations and anions used for commonly used to make ionic liquids. . . .	1
2.1. Potential energy diagram of electron-transfer reaction between a donor and acceptor in the normal regime	23
2.2. Jablonski diagrams for the photophysics of the electron-transfer process for a donor–bridge–acceptor complex in neutral solvents and ionic liquids	28
2.3. Structures of DMPD–Pro–C343, coumarin 343, ionic liquid cations Pyrr_{14}^{+} and N_{1444}^{+} , and anion NTf_2^{-}	29
2.4. ^1H NMR spectrum of DMPD–Pro–C343 molecule	30
2.5. Steady-state absorption spectra of DMPD–Pro–C343 in $\text{Pyrr}_{14}^{+}/\text{NTf}_2^{-}$, $\text{N}_{1444}^{+}/\text{NTf}_2^{-}$, CH_3CN and CH_3OH	31
2.6. Cyclic Voltammogram of ferrocene in four solvents	33
2.7. Steady-state emission spectra of DMPD–Pro–C343 in $\text{Pyrr}_{14}^{+}/\text{NTf}_2^{-}$, $\text{N}_{1444}^{+}/\text{NTf}_2^{-}$, CH_3CN and CH_3OH	34
2.8. Time-correlated single-photon counting system setup used for this study	36
2.9. Structure of coumarin 314	36
2.10. TCSPC transients for C314 and DMPD–Pro–C343 in $\text{Pyrr}_{14}^{+}/\text{NTf}_2^{-}$.	37
2.11. Optimized geometry of DMPD and coumarin343	41
2.12. Optimized geometry of DMPD–Pro–C343 using B3LYP/6- 311+G(d,p)	42
2.13. Cyclic staircase voltammograms of DMPD–Pro–C343 in four solvents .	43
2.14. Cyclic staircase voltammograms of coumarin 314 and DMPD in four solvents	43
2.15. Temperature dependent steady state emission spectra of DMPD–Pro– C343 in $\text{Pyrr}_{14}^{+}/\text{NTf}_2^{-}$ and $\text{N}_{1444}^{+}/\text{NTf}_2^{-}$	46

2.16. Temperature dependent steady state emission spectra of DMPD–Pro–C343 in CH ₃ OH and CH ₃ CN	47
2.17. Excitation wavelength dependent steady-state emission spectra of DMPD–Pro–C343 in Pyr ₁₄ ⁺ /NTf ₂ [–]	49
2.18. Excitation wavelength dependent steady-state emission spectra of DMPD–Pro–C343 in N ₁₄₄₄ ⁺ /NTf ₂ [–]	50
2.19. TCSPC transients for DMPD–Pro–C343 and C314 in CH ₃ CN at 293.2 K	52
2.20. TCSPC transients for DMPD–Pro–C343 in the ionic liquids and the neutral solvents at 293.2 K	53
2.21. TCSPC transients of DMPD–Pro–C343 in Pyr ₁₄ ⁺ /NTf ₂ [–] and N ₁₄₄₄ ⁺ /NTf ₂ [–] from 278.2 to 333.2 K	55
2.22. Distribution fits for DMPD–Pro–C343 in Pyr ₁₄ ⁺ /NTf ₂ [–] , N ₁₄₄₄ ⁺ /NTf ₂ [–] , CH ₃ OH, and CH ₃ CN	59
2.23. Arrhenius plots of DMPD–Pro–C343 electron-transfer rates in four solvents	60
2.24. Plot of ln(<i>k</i> _{ET,pk}) for electron transfer in DMPD–Pro–C343 <i>vs</i> ln(viscosity, cP) in the ionic liquids and the neutral solvents	63
2.25. Plot of ln(<i>k</i> _{ET,pk} <i>T</i> ^{1/2}) <i>vs</i> (1/ <i>T</i>) for intramolecular electron transfer of DMPD–Pro–C343 in the four solvents	64
3.1. Structures of the four ionic liquids studied using 2D NMR Overhauser effect spectroscopy.	80
3.2. The energy diagram for AX spin system.	82
3.3. The 2D NMR NOESY pulse sequence.	83
3.4. Basic 2D NMR HOESY pulse sequence developed by Rinaldi ³² and Yu and Levy. ^{33,34}	84
3.5. Pulse field gradient enhanced inverse-2D HOESY sequence developed by Bauer. ³⁵	85
3.6. Pulse field gradient enhanced inverse-HOESY sequence, improved Alam, <i>et al.</i> ³⁶	85

3.7. The complete 2D pulse field gradient enhanced inverse-HOESY sequence used in this study	86
3.8. Diagram of the flame sealed coaxial NMR tube sample set up	87
3.9. Isodensity plot of the $\{^1\text{H}-^1\text{H}\}$ -NOESY spectrum of $\text{P}_{2228}^+/\text{NTf}_2^-$. . .	90
3.10. Isodensity plot of the $\{^1\text{H}-^1\text{H}\}$ -NOESY spectrum of $\text{P}_{222(2\text{O}2\text{O}2)}^+/\text{NTf}_2^-$	91
3.11. Isodensity plot of the $\{^1\text{H}-^1\text{H}\}$ -NOESY spectrum of $\text{N}_{2228}^+/\text{NTf}_2^-$. . .	92
3.12. Isodensity plot of the $\{^1\text{H}-^1\text{H}\}$ -NOESY spectrum of $\text{N}_{222(2\text{O}2\text{O}2)}^+/\text{NTf}_2^-$	93
3.13. Contour plot of the $\{^{19}\text{F}-^1\text{H}\}$ -HOESY spectrum of $\text{P}_{2228}^+/\text{NTf}_2^-$	94
3.14. Contour plot of the $\{^{19}\text{F}-^1\text{H}\}$ -HOESY spectrum of $\text{P}_{222(2\text{O}2\text{O}2)}^+/\text{NTf}_2^-$	95
3.15. Contour plot of the $\{^{19}\text{F}-^1\text{H}\}$ -HOESY spectrum of $\text{N}_{2228}^+/\text{NTf}_2^-$. . .	96
3.16. Contour plot of the $\{^{19}\text{F}-^1\text{H}\}$ -HOESY spectrum of $\text{N}_{222(2\text{O}2\text{O}2)}^+/\text{NTf}_2^-$	97
3.17. Contour plot of the $\{^{31}\text{P}-^1\text{H}\}$ -HOESY spectrum of $\text{P}_{222(2\text{O}2\text{O}2)}^+/\text{NTf}_2^-$	98
3.18. Histogram of intensity of each representative proton peak from ^1H NMR at each mixing time (indicated by different colors) for $\text{P}_{2228}^+/\text{NTf}_2^-$ (top) and $\text{P}_{222(2\text{O}2\text{O}2)}^+/\text{NTf}_2^-$ (bottom)	101
3.19. Histogram of intensity of each representative proton peak from ^1H NMR at each mixing time (indicated by different colors) for $\text{N}_{2228}^+/\text{NTf}_2^-$ (top) and $\text{N}_{222(2\text{O}2\text{O}2)}^+/\text{NTf}_2^-$ (bottom)	102
3.20. Optimized geometry of $\text{P}_{2228}^+/\text{NTf}_2^-$	106
3.21. Optimized geometry of $\text{P}_{222(2\text{O}2\text{O}2)}^+/\text{NTf}_2^-$	106
3.22. Optimized geometry of $\text{N}_{2228}^+/\text{NTf}_2^-$	107
3.23. Optimized geometry of $\text{N}_{222(2\text{O}2\text{O}2)}^+/\text{NTf}_2^-$	107
3.24. Structure function of N_{2228}^+ , P_{2228}^+ , $\text{N}_{222(2\text{O}2\text{O}2)}^+$, and $\text{P}_{222(2\text{O}2\text{O}2)}^+$. .	109
4.1. Paramagnetic ionic liquids and solids.	120
4.2. Infrared spectra of $\text{bmim}^+/\text{FeCl}_4^-$, $\text{Pyrr}_{14}^+/\text{FeCl}_4^-$, $\text{N}_{4444}^+/\text{FeBrCl}_3^-$ and $\text{N}_{1444}^+/\text{FeCl}_4^-$	123
4.3. Molecular packing of $\text{Pyrr}_{14}^+/\text{FeCl}_4^-$	127
4.4. Molecular packing of $\text{N}_{1444}^+/\text{FeCl}_4^-$	128
4.5. Diagram of the unit cell of $\text{N}_{1444}^+/\text{FeCl}_4^-$	129

4.6. Raman spectra of $\text{bmim}^+/\text{FeCl}_4^-$, $\text{Pyrr}_{14}^+/\text{FeCl}_4^-$, $\text{N}_{4444}^+/\text{FeBrCl}_3^-$ and $\text{N}_{1444}^+/\text{FeCl}_4^-$	130
4.7. DSC scans of $\text{Pyrr}_{14}^+/\text{FeCl}_4^-$, $\text{N}_{1444}^+/\text{FeCl}_4^-$, and $\text{N}_{4444}^+/\text{FeBrCl}_3^-$.	131
4.8. $\chi_M T$ vs. T for $\text{N}_{1444}^+/\text{FeCl}_4^-$, $\text{Pyrr}_{14}^+/\text{FeCl}_4^-$ and $\text{N}_{4444}^+/\text{FeBrCl}_3^-$	134
4.9. Inverse χ_M vs. temperature for $\text{Pyrr}_{14}^+/\text{FeCl}_4^-$, $\text{N}_{1444}^+/\text{FeCl}_4^-$ and $\text{N}_{4444}^+/\text{FeBrCl}_3^-$	135

List of Tables

2.1. Donor-Acceptor Electronic Coupling from INDO/S CIS calculations . . .	40
2.2. Summary of thermodynamic, activation, and Marcus equation parameters for photoinduced charge separation in DMPD-Pro-C343.	42
2.3. Values for the dipole moments in the ground and excited electronic states for C314, C343, and DMPD-Pro-C343	44
2.4. Multi-Exponential Analysis of DMPD-Pro-C343 Emission Transients in Four Solvents at 293.2 K	56
2.5. Rates and relative amplitudes for emission transients of DMPD-Pro-C343 in CH ₃ OH	56
2.6. Rates and relative amplitudes for emission transients of DMPD-Pro-C343 in CH ₃ CN	56
2.7. Rates and relative amplitudes for emission transients of DMPD-Pro-C343 in N ₁₄₄₄ ⁺ /NTf ₂ ⁻	57
2.8. Rates and relative amplitudes for emission transients of DMPD-Pro-C343 in Pyr ₁₄ ⁺ /NTf ₂ ⁻	57
2.9. Values for the most probable electron-transfer rates k_{ET} in ns ⁻¹	58
3.1. Normalized effective integral value for each proton for each cation at different mixing times for P ₂₂₂₈ ⁺ /NTf ₂ ⁻ / and P _{222(2O2O2)} ⁺ /NTf ₂ ⁻ . . .	99
3.2. Normalized effective integral value for each proton for each cation at different mixing times for N ₂₂₂₈ ⁺ /NTf ₂ ⁻ / and N _{222(2O2O2)} ⁺ /NTf ₂ ⁻ . . .	100
3.3. Charges calculated from fits of the electrostatic potential to atom-centered charges, using the CHelpG algorithm of the four cations, P ₂₂₂₈ ⁺ , P _{222(2O2O2)} ⁺ , N ₂₂₂₈ ⁺ , and N _{222(2O2O2)} ⁺	108
4.1. Crystallographic data for N ₁₄₄₄ ⁺ /FeCl ₄ ⁻ and Pyr ₁₄ ⁺ /FeCl ₄ ⁻	123

4.2. DSC transition temperatures for the four ILs studied.	132
4.3. Magnetic properties of the novel paramagnetic ILs	134

Abbreviations and Terms

A: Acceptor

AM1: Austin Model 1

APS: Advanced Photon Source

bmim⁺: butylmethylimidazolium

BNL: Brookhaven National Laboratory

C153: coumarin 153

C314: coumarin 314

C343: coumarin 343

CIF: Crystallographic Information File

c: speed of light

C: Curie constant

CCD: charge-coupled device

CHARMM: chemistry at harvard molecular mechanism for macromolecular simulation

CI: configuration interaction singles

CSV: cyclic staircase voltammetry

CV: cyclic voltammetry

D: donor

DA : encounter complex

D-B-A: donor-bridge-acceptor complex

DCA⁻: dicyanamide

DCC: N,N'-dicyclohexylcarbodiimide

DFT: density functional theory

DIPEA: diisopropylethylamine

DMF: N,N-dimethylformamide

DMPD: 1-N,1-N-dimethyl-1,4-phenylenediamine

DSC : differential scanning calorimetry

E^0 : electrode potential

$E_{1/2}$: half-wave potential

$E_{1/\eta}$: activation energy for viscous flow

E_a : activation energy

E_T : solvent polarity

$E_{1/\eta}$: activation energies for viscous flow

$\Delta E_{0,0}$: electronic transition energy

ΔE_{12} : adiabatic excitation energy

Eq: equation

ESI⁺ :electrospray ionization

E_T : effective solvent polarity

ET: electron-transfer

F1: observed sensitive nucleus

F2: irradiated insensitive heteronucleus

Fc: ferrocene

FCWDS: Franck-Condon weighted density of states

FID: Free Induction Decay

Fig: Figure

FSDP: first sharp diffraction peak

FT-IR: Fourier-Transform Infrared

FW: formula weight

FWHM: Full-width at half-maximum

g : adiabaticity parameter

$g(\log\tau)$: distribution function time constant

ΔG : Gibbs free energy

ΔG^0 : driving force (reaction free energy)

ΔG^* : free energy barrier (free energy of activation)

GC: glassy carbon

h : Plank constant

\hbar : Plank consant/ 2π

H_{DA} : donor-acceptor electronic coupling

HPLC: high-performance liquid chromatography

HOBt: 1-hydroxybenzotriazole

HOESY: heteronuclear Overhauser effect spectroscopy

HOMO: highest occupied molecular orbital

IEFPCM: integral equation formalism polarizable continuum model

IL: Ionic Liquid

ImCl: 1-ethyl-3-methylimidazolium chloride

INDO: intermediate neglect of differential overlap semi-empirical electronic structure method

IRF: instrument response function

$I(t)$: transient intensity

k_B : Boltzmann constant

k_{ET} : rate of electron transfer

$k_{ET,NA}$: nonadiabatic electron-transfer rate

$k_{ET,pk}$: effective electron-transfer rate
 $k_{ET,SC}$: solvent-controlled or adiabatic electron-transfer rate
 k_{fl} : nonreactive excited-state decay
 k_{obs} : observed fluorescence decay rate
 k_{solv} : rate of solvation
 LUMO: lowest unoccupied molecular orbital
 MD: molecular dynamics
 MEF: multi-exponential function
 MS: Mass spectrometry
 N_{1444}^{+} : tributylmethyammonium
 N_{4444}^{+} : tetrabutylammonium
 N_{2228}^{+} : triethyloctylammonium
 $N_{222(2O2O2)}^{+}$: (2-ethoxyethoxy)ethyltriethylammonium
 N_A : Avagadros number
 NOE: nuclear Overhauser effect
 NOESY: nuclear Overhauser enhancement spectroscopy
 NLS: nonlinear least-square
 NMR: nuclear magnetic resonance
 NTf_2^{-} : bis-(trifluoromethylsulfonyl)amide
 PAR: Princeton Applied Research
 PFG: pulse field gradient
 Pro: proline
 $Pyrr_{14}^{+}$: 1-butyl-1-methylpyrrolidinium
 P_{2228}^{+} : triethyloctylphosphonium

$P_{222(2O_2O_2)}^+$: (2-ethoxyethoxy)ethyltriethylphosphonium

$Pyrr_{1,n}^+$: 1-alkyl-1-methylpyrrolidinium

r_B-r_A : internuclear distance for a two-spin system in nuclear Overhauser effect spectroscopy

R_{DA} : donor-acceptor distance

REE: red-edge effect

RF: Radio Frequency

S: electronic spin

SHG: Second-harmonic generation

$S(q)$: structure function

SQUID: superconducting quantum interference device

t: time

t1: evolution time

t2: acquisition time

T: temperature

$T_{coldcryst/anneal}$: crystalization/annealing transition temperature

T_g : glass transition temperature

T_m : melting temperature

T_{s-s} : solid to solid transition temperature

N_{4444}^+ : tetrabutylammonium

TCSPC: time-correlated single-photon counting

ZINDO: Zerner's intermediate neglect of differential overlap semi-empirical electronic structure method

β : magnitude of electron transfer interaction
 γ : gyromagnetic ratio
 ε_0 : vacuum permittivity
 η : viscosity
 θ : Weiss constant
 λ : reorganization energy
 $\lambda_{em,max}$: emission wavelength at maximum
 λ_{xray} : incident x-ray wavelength
 μ : dipole moment
 μ_B : Bohr magneton
 μ_{eff} : effective magnetic moment
 μ_{12} : adiabatic transition dipole moment
 $\Delta\mu_{12}$: difference in adiabatic state dipole moments
 ν : frequency
 τ : decay time constant
 τ_m : mixing time
 τ_{peak} : lifetime value from the peak of the distribution
 τ_s : solvation time
 τ_{solv} : solvent relaxation time
 χ : magnetic susceptibility
 χ_R^2 : reduced chi-square
 χ_M : molar magnetic susceptibility
 ω_{xy} : electrostatic work term

Table of Contents

Abstract	ii
List of Figures	vi
List of Tables	x
1. Introduction	1
1.1. Background and Context for This Research	1
1.2. Vision for this Research	3
1.2.1. Electron Transfer in Ionic Liquids	3
1.2.2. Structural Study of Ionic Liquids	5
1.2.3. Paramagnetic Ionic Liquids	6
1.3. Conclusions	8
2. A Comparison of Electron-Transfer Dynamics in Ionic Liquids and Neutral Solvents	21
2.1. Background on Electron Transfer	21
2.1.1. Marcus Theory	22
2.1.2. Electron Transfer in Ionic Liquids	25
2.2. Electron Transfer in Ionic Liquids <i>vs</i> Neutral Solvents	26
2.3. Experimental Methods	29
2.3.1. Synthesis and Characterization of DMPD-Pro-C343	29
2.3.2. Preparation of Spectroscopic Samples	30
2.3.3. Electrochemical Measurements	32
2.3.4. Time-Integrated Emission Spectroscopy	33
2.3.5. Time-Resolved Emission Spectroscopy	34

2.3.6.	TCSPC Data Analysis	35
2.4.	Results and Discussion	39
2.4.1.	Evaluation of Electron Donor-Acceptor Interactions	39
2.4.2.	Estimation of the Driving Forces for the Electron-Transfer Reactions	40
2.4.3.	Steady-State Fluorescence Spectroscopy of DMPD-Pro-C343	44
	Effect of Excitation Wavelength on Photoinduced Electron-Transfer of DMPD-Pro-C343	45
2.4.4.	Time-Resolved Measurements of Electron-Transfer Kinetics in DMPD-Pro-C343	51
2.4.5.	Analysis of the DMPD-Pro-C343 Emission Transients	52
	Discrete Multiexponential Model for the Analysis of Emission Transients of DMPD-Pro-C343	52
	Distributed Exponential Model for the Analysis of Emission Transients of DMPD-Pro-C343	57
2.4.6.	Analysis of the Observed Electron-Transfer Rates Using Marcus Theory	64
2.5.	Conclusions	66
3.	Differences in Intermediate Range Order Between NTf₂⁻-Anion Ionic Liquids with Alkyl- vs. Ether- Substituted Cations	78
3.1.	Background on Structural Ordering of Ionic Liquids	78
3.1.1.	2D NMR Overhauser Effect Spectroscopy	81
3.2.	Experimental Methods	86
3.2.1.	Sample Preparation for NMR Spectroscopy	86
3.2.2.	NMR Measurements	87
3.2.3.	Electronic Structure Calculations of the Cation Charges	88
3.3.	Results	88
3.3.1.	Results from Overhauser Effect from 2D NMR Spectroscopy	88

3.3.2. Results from the Electronic Structure Calculations on the Cations	105
3.3.3. X-ray Scattering Results	109
3.4. Discussion	110
3.5. Conclusions	111
4. Ionic Liquids and Solids with Paramagnetic Anions	119
4.1. Introduction	119
4.2. Experimental methods	120
4.2.1. Synthesis	120
New Ionic Compounds: $\text{Pyrr}_{14}^{+}/\text{FeCl}_4^{-}$ and $\text{N}_{1444}^{+}/\text{FeCl}_4^{-}$.	120
Preparation of other ionic compounds	122
4.2.2. X-Ray Structure Determination	122
4.2.3. Vibrational Spectroscopy	122
4.2.4. Thermal Measurements	124
4.2.5. Magnetic Properties	124
4.3. Results and Discussion	124
4.3.1. Raman spectra	126
4.3.2. Thermal properties	126
4.3.3. Magnetic properties	132
4.4. Conclusions	136
5. Summary and Future Directions	140
Appendix A. Appendix	152
A.1. Details of the TCSPC data analysis	152

Chapter 1

Introduction

1.1 Background and Context for This Research

Ionic liquids (ILs) are commonly defined as molten salts with a melting temperature below 100 °C that are entirely composed of ions.¹ Compared to conventional solvents, they have fascinating and unique characteristics, which enable their usage from energy storage to solvation of biomass. This has propelled an exponential growth in research interest about these liquids over the past decade.^{2–5} Some examples of how ILs differ from conventional solvents are that ILs generally have negligible volatility, controllable viscosities, and attractive electrochemical properties.^{3–6} These emerging classes of ILs have been called ‘designer solvents,’ or task-specific ILs,⁷ because they can be tailored to meet a desired task.⁸ The possibility of making up $\sim 10^{18}$ different ionic liquids⁹ using different combinations of cations and anions also provides for new materials. Common cations and anions used to make ionic liquids are shown in Fig.1.1.

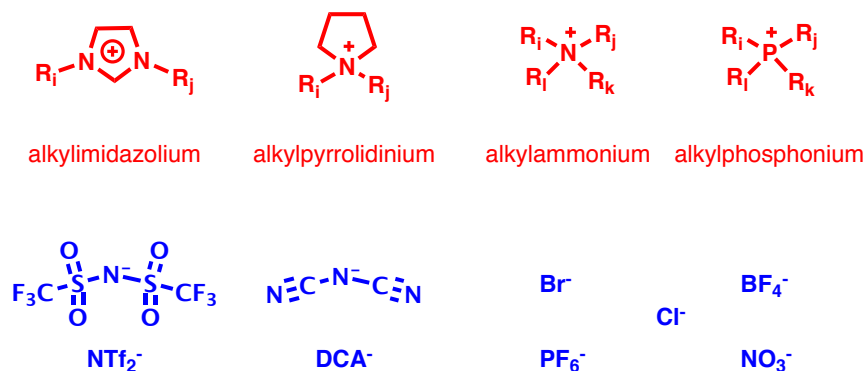


Figure 1.1: Cations (red) and anions (blue) commonly used to make ionic liquids.

The range of IL properties, which often exceed those of common solvents, give the ILs advantages for energy applications. The ionic composition of ILs make them

natural electrolytes, and they generally display broad electrochemical stability windows;¹⁰ 1-alkyl-1-methylazepanium bis(trifluoromethyl)sulfonylamide IL was reported to exhibit an electrochemical stability window between oxidation and reduction of 6.5 volts.¹¹ These properties of ILs make them attractive candidates as electrolytes in batteries.^{12,13} As a result, lithium batteries with IL electrolytes constitute an active field of research.^{14,15} Other rapidly evolving research areas use ILs for energy capture and storage media,^{13,16,17} double-layer capacitors,¹⁸ solar cells,^{19,20} and fuel cells.²¹ One of the useful properties of ILs is the low vapor pressure at ambient temperature, which arises from the strong Coulombic forces between the ions. The low volatility of ILs is ideal for applications such as batteries and solar cells to avoid solvent evaporation from polymer gel electrolytes, thus extending the durability of the device compared to conventional solvents.

In addition to the energy related applications, there are numerous other applications for these versatile liquids, including biomass processing such as the breakdown of lignocellulose^{22–24} and the destruction of algae for production of sugar and proteins. One of the most fascinating applications of ILs is found in nuclear technology.²⁵ For the extraction of uranium from water, tricaprylmethylammonium thiosalicylate IL has been tested and found to be highly efficient.²⁶ Ionic liquids based on 1-alkyl-3-methylimidazolium cations have been found to be useful in reprocessing highly radioactive nuclear fuel.²⁷ Consequently, the radiation chemistry of ILs is an important area of research because the ILs that are exposed to radiation will need to be reprocessed for recycling.^{3,28,29}

ILs have typical viscosities that range from 10 – 10,000 cP at ambient temperatures.³⁰ Accordingly, ILs show dynamical effects typical of glassy materials. Dynamical heterogeneity in ILs has been observed extensively in time-resolved fluorescence studies^{31–38} and in transient spectroscopy.³⁹ The factors that control dynamical heterogeneity, however, remain unresolved. The research presented here investigates these unanswered questions as part of this thesis. Another part of this thesis is concerned with the consequences of these dynamical effects on electron-transfer reactions, an essential component of many energy-related applications of ILs. It is not yet apparent to what extent dynamical and reactive heterogeneity can be ascribed to the heterogeneous

structures of ILs and how much of it is due to the well-known heterogeneous dynamics of glassy systems.^{6,39–43}

1.2 Vision for this Research

This thesis touches on several aspects of ILs research. A major part of this research is on photochemical reactions in ionic liquids, in particular, photoinduced electron-transfer reactions. Inspired by the work of Issa, *et al.*⁴⁴ we have explored the effects of ILs as the solvent for one of the most fundamental reactions in chemistry, electron transfer. We observed that reaction kinetics in ILs are dynamically heterogeneous. Intramolecular electron transfer studies of a donor-bridge-acceptor molecule required a solvent-controlled electron-transfer model for the IL solvent. The observation of heterogeneous reaction dynamics in ILs motivated us to ask the question of what factors cause this dynamical heterogeneity, leading us to investigate the structural ordering of ILs. We have studied both static and dynamic structural heterogeneity in ILs using various techniques to investigate what determines the structural ordering and how different components of ILs change the local structures.

1.2.1 Electron Transfer in Ionic Liquids

It is important to study charge transfer in ILs because ionic liquids are excellent media for electrochemical devices that collect, store, or utilize energy³ since they are inherent electrolytes with ion concentrations of 3~4 M. In order to use ILs optimally in such applications, it is essential to understand how these unconventional solvents affect electron-transfer reactions. This is not a simple task – the solvation environment of ILs is complex, combining strongly polar charged and dipolar interactions with hydrophobic ones. While pure ionic liquids have moderate static dielectric constants typically ranging from 8 to 15,⁴⁵ they often manifest stronger polar interactions when solvatochromic dyes are used to estimate the solvent polarity.^{46–49} This is because solvatochromic dyes may experience different local environments from the bulk average of the IL. In several cases, the effective local polarity of ILs is similar to that of neutral polar solvents like

CH_3CN and CH_3OH .^{46,47}

Reaction dynamics in ILs have also shown similarities to those in organic solvents. For example, thermodynamic quantities for a variety of neutral organic species dissolved in 1-hexyl-3-methyl imidazolium bis(trifluoromethylsulfonyl)amide are shown to be strongly correlated with the values for CH_3CN .⁴⁸ Shim and his coworkers have shown through molecular simulations that for the 1-butyl-3-methylimidazolium dicyanamide ionic liquid, the barrier crossing dynamics for a model diatomic reaction complex is similar to that in CH_3CN when Grote-Hynes analysis is applied.^{42,50,51} In addition, work by Lynden-Bell^{52,53} and Annapureddy⁵⁴ has shown that despite the generally higher viscosities of ionic liquids, the Marcus analysis of the free energy of reaction can still be applied.

Nonetheless, electron-transfer reactions in ILs are complicated for several reasons. As mentioned above, ILs typically have viscosities that are 10^2 - 10^3 higher than those of typical neutral organic solvents. Rates of bimolecular electron-transfer reactions will be affected by the limitations imposed by higher viscosities that lead to slower self-diffusion of the reactants.^{33,55,56} The higher viscosities also lead to slower overall solvent reorganization following charge redistribution, as illustrated by the numerous studies of solvation dynamics using time-resolved spectroscopy of solvatochromic fluorescence probes.^{32-38,49,57} Overall, the average solvation dynamics do track the shear viscosity of the solution, though with broad dispersion in response times. In a recent investigation, Sahu, *et al.* used a novel two-dimensional electronic spectroscopy method to investigate a photoinduced electron-transfer reaction that is coupled to an intramolecular isomerization in auramine O.³⁹ For ionic liquid solvents, substantial dynamic heterogeneity of the reaction rate was observed; their analysis revealed a distribution of reaction rates spanning two orders of magnitude that they attributed to a broad Gaussian distribution of reaction barrier heights. It was our aim to study the effect of ILs as solvents for photoexcited intramolecular electron-transfer reactions by choosing two different ionic liquids differing in viscosities, in an attempt to vary the rate of solvation dynamics.³¹ In Chapter 2, we discuss the findings of our research, comparing the solvation dynamics of ILs with those of common neutral solvents.

1.2.2 Structural Study of Ionic Liquids

Ionic liquids differ from simple salts (i.e. NaCl) in that they have low melting points and display different structural ordering. Unlike simple salts, ILs are molecularly disordered and lack long range ordering and behave like liquids in that the x-ray diffraction measurements of ILs typically show broad peaks. However, experimental results show that ILs possess short range structural ordering (charge-ordering) similar to molten salts and intermediate range ordering.⁵⁸⁻⁶³ It is intuitive that ILs will form charge ordering to maximize Coulombic interactions because of the high charge density ‘heads’ of the cations and anions. This leaves the low charge density ‘tails’ (such as alkyl chains) to occupy space elsewhere. The combination of these two types of interactions leads ILs to have intermediate range ordering.

Molecular dynamics simulations done by Kashyap, *et al.*^{64?} showed that the intermediate range ordering displayed by many ILs results from the combination of alternating charges and charge densities. The experimental data leading up to this research also supported this result. Hardacre, *et al.*⁶⁵ showed using neutron scattering that the structure of 1-alkyl-3-methylimidazolium hexafluorophosphate ILs ($[C_n\text{mim}][\text{PF}_6]$, $n = 4, 6, \text{ and } 8$) is dominated by the polar heads of cations and anions. The role of the nonpolar chains for structural ordering of ILs was emphasized when Canongia Lopes, *et al.*⁶⁶ reported the results from molecular simulations done on the same set of ILs reported by Hardacre, *et al.*. They reported that when $n=4$ or greater, the nonpolar alkyl chains start to aggregate and heterogeneous structural ordering is observed. Their results provided evidence that the intermediate range ordering comes from the amphiphilic nature while the short range ordering results from the electrostatic forces. More recently, Triolo, *et al.*⁶⁷ also used x-ray scattering to argue that the bulk morphology of ILs is defined by the chain segregation. Evidence of mesoscopic structural ordering formed by the tail segregation was also seen by observing the changes in bulk properties such as density and viscosity while the chain lengths are varied.^{66,68-71} However, Jeong, *et al.*⁷² has pointed out that such mesoscopic structural ordering is not a fixed static structuring, but rather a dynamical ordering and that different techniques

are necessary to interrogate the structural ordering of ILs at different time scales.

Using 2D NMR techniques, especially those using the nuclear Overhauser effect (explained in detail in Chapter 3), one can learn about the local structural ordering of ILs.^{73–75,75–78} Mele *et al.* used 2D NMR, combined with computational simulations, and reported certain cation-anion interactions of imidazolium and pyrrolidinium ILs.^{76,78} They reported that the fluorine atoms on the NTf_2^- anion interact more strongly with certain hydrogen atoms on the cation, such as those on the imidazolium or pyrrolidinium ring, than other hydrogen atoms, such as those on the nonpolar tail. Their results also confirmed that nanoscale segregation of the cation-anion polar head groups occurs for the ILs studied. They indicated that such aggregation is possibly due to strong H–F intermolecular interactions between the cation and the anion. We thus attempted to use 2D NMR methods to elucidate the reasons for the difference in the structural ordering, demonstrated through x-ray scattering results,⁷⁹ of non-polar octyl-chained cations and cations with the tails replaced by polar substituents. Detailed discussions along with the results of this study are presented in Chapter 3.

1.2.3 Paramagnetic Ionic Liquids

The final study reported here was inspired by the work of Hayashi and Hamaguchi^{80,81} where the magnetic properties of ferric-based magnetic ionic liquids were reported, in an attempt to find a new class of magnetic materials that can be applied as nanomagnets. An interesting class of ionic liquids is paramagnetic ionic liquids, which include the world’s first ‘magnetic soap.’⁸² For example, paramagnetic ionic liquids based on iron-gallium⁸³ and iron⁸⁴ anions were reported by Yoshida, *et al.* and Hamaguchi and co-workers have published several articles on the $\text{bmim}^+/\text{FeCl}_4^-$ paramagnetic IL.^{80,81,85,86} Abbott, *et al.* reported ionic liquids with the FeCl_4^- anion paired with both trimethylethanolammonium and dimethylphenylethanolammonium cations.⁸⁷ Del Sesto, *et al.* have reported a series of paramagnetic ionic liquids having tetraalkylphosphonium or alkylmethylimidazolium cations paired with tetrahedral or octahedral symmetry transition metal anions, for which the metal is iron, cobalt, manganese or gadolinium.⁸⁸

Fluids with macroscopic paramagnetic or ferromagnetic responses have been of great interest especially for their potential applications and have been created using several methods. One method involves dissolving or suspending paramagnetic or ferromagnetic particles in a solvent. Magnetorheological fluids are normally made by dispersing magnetic particles (such as iron oxides) in a carrier fluid, which then permits control of the bulk viscosity by external magnetic fields.⁸⁹ A parallel application is the stirring of non-magnetic particles by the rotation induced in a paramagnetic ionic liquid ($\text{bmim}^+/\text{FeCl}_4^-$) as it responds to a rotating external magnetic field.⁹⁰ In a related manner, paramagnetic $\gamma\text{-Fe}_2\text{O}_3$ and CoFe_2O_4 nanoparticles can be added to non-magnetic ionic liquids to create a paramagnetic fluid.⁹¹ The synthesis of molecular magnets, including cyano-bridged magnetic nanoparticles, can be optimized by using ionic liquids as the reaction solvent.⁹² Catalytic processes such as aryl Grignard cross-coupling reactions⁹³ and Friedel-Crafts reactions in mesoporous silica⁹⁴ have been enhanced by replacing the traditional FeCl_3 catalyst by ionic liquid catalysts such as $\text{bmim}^+/\text{FeCl}_4^-$. Development of magnetic ionic liquids is especially of interest for application purposes because of their negligible vapor pressure compared to volatile organic solvents, which is the base for most magnetic fluids.

Fe(III) -containing ILs are especially interesting because of their paramagnetic nature that combines the properties of conventional ferrofluids with those of ILs. Kozlova, *et al.* reported a paramagnetic ionic liquid with an anion containing Co(II) , $(\text{bmim}^+)_2/\text{CoBr}_4^{2-}$.⁹⁵ Several other salts based on the FeCl_4^- anion have been reported with melting temperatures just above 100 °C.^{96–100} Mudring and coworkers have prepared and characterized paramagnetic ionic liquids with transition metals and lanthanides.^{101,102} Although the higher spin moments of certain f -block elements can produce ionic liquids with stronger magnetism, the low cost and relative abundance of iron make Fe-based magnetic ILs attractive subjects for continued study. In Chapter 4, we discuss the development of similar Fe(III) -based novel paramagnetic ionic liquids and solids and present their crystallographic and magnetic data.

1.3 Conclusions

Ionic liquids provide virtually limitless research areas and applications because of their remarkably versatile properties. While many industries and engineers are looking for ways to apply these new classes of materials, investigating the fundamental physico-chemical properties of these liquids must be ongoing. As the field of ILs is still in an early stage of development, there are on occasion more questions than answers arising from these findings. Some of the fundamental questions are the cause and consequences of the dynamical heterogeneity that many ILs display. We attempted to answer this question by observing the reaction heterogeneity of intramolecular electron transfer in a donor-bridge-acceptor molecule, then studying the structural ordering of the ILs using different techniques to search for structural heterogeneity. Given that ILs are complex, the bigger aim of such fundamental studies should be constructing models to represent and understand what controls these phenomena in ILs. Perhaps the same models and approximations used for the neutral solvents can be applied to ILs, but if so, what are the assumptions we must make and at what point do they break down? It is our hope that the findings reported here act as a stepping stone and a guide for the future of ionic liquid research and development.

Bibliography

- [1] J. S. Wilkes. A short history of ionic liquids-from molten salts to neoteric solvents. *Green Chem.*, 4:73–80, 2002.
- [2] W. L. Hough and R. D. Rogers. Ionic liquids then and now: From solvents to materials to active pharmaceutical ingredients. *Bull. Chem. Soc. Jpn.*, 80:2262–2269, 2007.
- [3] J. F. Wishart. Energy applications of ionic liquids. *Energy Environ. Sci.*, 2:956–961, 2009.
- [4] N. V. Plechkova and K. R. Seddon. Applications of ionic liquids in the chemical industry. *Chem. Soc. Rev.*, 37:123–150, 2008.
- [5] E. W. Castner, Jr. and J. Wishart. Spotlight on ionic liquids. *J. Chem. Phys.*, 132:120901, 2010.
- [6] E. W. Castner, Jr., C. J. Margulis, M. Maroncelli, and J. F. Wishart. Ionic liquids: Structure and photochemical reactions. *Annu. Rev. Phys. Chem.*, 62:85–105, 2011.
- [7] J. H. Davis, Jr. and P. A. Fox. From curiosities to commodities: ionic liquids begin the transition. *Chem. Commun.*, 2003:1209–1212, 2003.
- [8] M. Freemantle. Designer solvents - ionic liquids may boost clean technology development,. *Chem. Eng. News*, 76:32–37, 1998.
- [9] R. D. Rogers and K. R. Seddon. Ionic liquids - solvents of the future? *Science*, 302:792–793, 2003.

- [10] M. Armand, F. Endres, D. MacFarlane, H. Ohno, and B. Scrosati. Ionic-liquid materials for the electrochemical challenges of the future. *Nature Materials*, 8:621, 2009.
- [11] T. Belhocine, S. A. Forsyth, H. Q. N. Gunaratne, M. Nieuwenhuyzen, A. V. Puga, K. R. Seddon, G. Srinivasan, and K. Whiston. New ionic liquids from azepane and 3-methylpiperidine exhibiting wide electrochemical windows. *Green. Chem.*, 13:59–63, 2011.
- [12] M. Galinski, A. Lewandowski, and I. Stepniak. Ionic liquids as electrolytes. *Electrochem.*, 51:5567–5580, 2006.
- [13] D. R. MacFarlane, M. Forsyth, P. C. Howlett, J. M. Pringle, J. Sun, G. Annat, W. Neil, and E. I. Izgorodina. Ionic liquids in electrochemical devices and processes: Managing interfacial electrochemistry. *Acc. Chem. Res.*, 40:1165–1173, 2007.
- [14] A. Lewandowski and A. Swiderska-Mocek. Ionic liquids as electrolytes for Li-ion batteries-an overview of electrochemical studies. *J. Power Sources*, 194:601–609, 2009.
- [15] H. Nakagawa, S. Izuchi, K. Kuwana, T. Nukuda, and Y. Aihara. Liquid and polymer gel electrolytes for lithium batteries composed of room-temperature molten salt doped by lithium salt. *J. Electrochem. Soc.*, 150:A695–A700, 2003.
- [16] S. M. Zakeeruddin and M. Graetzel. Solvent-free ionic liquid electrolytes for mesoscopic dye-sensitized solar cells. *Adv. Funct. Mater.*, 19:2187, 2009.
- [17] R. F. de Souza, J. C. Padilha, R. S. Goncalves, and J. Dupont. Room temperature dialkylimidazolium ionic liquid-based fuel cells. *Electrochem. Comm.*, 5:728, 2003.
- [18] C. Nanjundiah, S. F. McDevitt, and V. R. Koch. Differential capacitance measurements in solvent-free ionic liquids at Hg and C interfaces. *J. Electrochem. Soc.*, 144:3392–3397, 1997.

- [19] N. Papageorgiou, Y. Athanassov, M. Armand, P. Bonhote, H. Pettersson, A. Azam, and M. Gratzel. Power from the sun: the advent of mesoscopic solar cells. *J. Electrochem. Soc.*, 143:3099–3108, 1996.
- [20] H. Matsumoto, T. Matsuda, T. Tsuda, R. Hagiwara, Y. Ito, and Y. Miyazaki. The application of room temperature molten salt with low viscosity to the electrolyte for dye-sensitized solar cell. *Chem. Lett.*, 1:26–27, 2001.
- [21] M. Doyle, S. K. Choi, and G. Proulx. High-temperature proton conducting membranes based on perfluorinated ionomer membrane-ionic liquid composites. *J. Electrochem. Soc.*, 147:34–37, 2000.
- [22] R. P. Swatloski, S. K. Spear, J. D. Holbrey, and R. D. Rogers. Dissolution of cellulose with ionic liquids. *J. Am. Chem. Soc.*, 124:4974–4975, 2002.
- [23] D. A. Fort, R. C. Remsing, R. P. Swatloski, P. Moyna, G. Moyna, and R. D. Rogers. Can ionic liquids dissolve wood? Processing and analysis of lignocellulosic materials with 1-n-butyl-3-methylimidazolium chloride. *Green Chem.*, 9:63–69, 2007.
- [24] A. Ohno, H. Hashimoto, K. Nakajima, M. Suzuki, and K. Kimura. Observation of surface structure of 1-butyl-3-methylimidazolium hexafluorophosphate using high-resolution Rutherford backscattering spectroscopy. *J. Chem. Phys.*, 130:204705, 2009.
- [25] X. Sun, H. Luo, and S. Dai. Ionic liquids-based extraction: A promising strategy for the advanced nuclear fuel cycle. *Chem. Rev.*, 112:2100–2128, 2012.
- [26] M. Srncik, D. Kogelnig, A. Stojanovic, W. Korner, R. Krachler, and G. Wallner. Uranium extraction from aqueous solutions by ionic liquids. *Appl. Radiat. Isot.*, 12:2146–2149, 2009.
- [27] A. E. Bradley, C. Hardacre, M. Nieuwenhuyzen, W. R. Pitner, D. Sanders,

- K. R. Seddon, and R. C. Thied. A structural and electrochemical investigation of 1-alkyl-3-methylimidazolium salts of the nitratodioxouranate(VI) anions $[(\text{UO}_2(\text{NO}_3)_2)_2(\mu_4\text{-C}_2\text{O}_4)]^{2-}$, $[\text{UO}_2(\text{NO}_3)_3]^{-}$, and $[\text{UO}_2(\text{NO}_3)_4]^{2-}$. *Inorg. Chem.*, 43:2503–2514, 2004.
- [28] J. F. Wishart. “*Ionic liquid radiation chemistry*” in *Ionic Liquids: COILED for Action (in press)*. Wiley, Ltd., 2012.
- [29] J. F. Wishart. Radiation chemistry of ionic liquids: Reactivity of primary species. In R. D. Rodgers and K. R. Seddon, editors, *Ionic Liquids as Green Solvents: Progress and Prospects*, volume 856 of *ACS Symposium Series*, pages 381–396. 2003.
- [30] D. S. Viswanath, T. K. Ghosh, D. H. L. Parasad, N. V.K. Dutt, and K. Y. R. Rani. *Viscosity of Liquids*. Springer, 2007.
- [31] H. Y. Lee, J. B. Issa, S. S. Isied, E. W. Castner, Jr., Y. Pan, C. L. Hussey, K. S. Lee, and J. F. Wishart. A comparison of electron-transfer dynamics in ionic liquids and neutral solvents. *J. Phys Chem. C*, 116:5197–5208, 2012.
- [32] H. Jin, G. A. Baker, S. Arzhantsev, J. Dong, and M. Maroncelli. Solvation and rotational dynamics of coumarin 153 in ionic liquids: Comparisons to conventional solvents. *J. Phys. Chem. B*, 117:7291–7302, 2007.
- [33] A. Paul and A. Samanta. Solute Rotation and Solvation Dynamics in an Alcohol-Functionalized Room Temperature Ionic Liquid. *J. Phys. Chem. B*, 111:4724–4731, 2007.
- [34] S. Sarkar, R. Pramanik, D. Seth, P. Setua, and N. Sarkar. Photoinduced electron transfer (PET) from n,n-dimethylaniline to 7-amino coumarin dyes in a room temperature ionic liquid (RTIL): Slowing down of electron transfer rate compared to conventional solvents. *Chem. Phys. Lett.*, 477:102–108, 2009.

- [35] A. M. Funston, T. A. Fadeeva, J. F. Wishart, and E. W. Castner, Jr. Fluorescence probing of temperature-dependent dynamics and friction in ionic liquid local environments. *J. Phys. Chem. B*, 111:4963–4977, 2007.
- [36] E. W. Castner, Jr., J. F. Wishart, and H. Shirota. Intermolecular dynamics, interactions, and solvation in ionic liquids. *Acc. Chem. Res.*, 40:1217–1227, 2007.
- [37] H. Jin, X. Li, and M. Maroncelli. Heterogeneous solute dynamics in room-temperature ionic liquids. *J. Phys. Chem. B*, 111:13473–13478, 2007.
- [38] M. Maroncelli, X.-X. Zhang, M. Liang, D. Roy, and N. P. Ernstring. Measurements of the complete solvation response of coumarin 153 in ionic liquids and the accuracy of simple dielectric continuum predictions. *Faraday Discuss.*, 154:409–424, 2012.
- [39] K. Sahu, S. J. Kern, and M. A. Berg. Heterogeneous reaction rates in an ionic liquid: Quantitative results from two-dimensional multiple population-period transient spectroscopy. *J. Phys. Chem. A*, 115:7984–7993, 2011.
- [40] J. Habasaki and K. L. Ngai. Heterogeneous dynamics of ionic liquids from molecular dynamics simulations. *J. Chem. Phys.*, 129:194501, 2008.
- [41] Y. Wang, W. Jiang, T. Yan, and G. A. Voth. Understanding ionic liquids through atomistic and coarse-grained molecular dynamics simulations. *Acc. Chem. Res.*, 40:1193–1199, 2007.
- [42] Y. Shim, D. Jeong, S. Manjari, M. Y. Choi, and H. J. Kim. Solvation, solute rotation and vibration relaxation, and electron-transfer reactions in room-temperature ionic liquids. *Acc. Chem. Res.*, 40:1130–1137, 2007.
- [43] C. Khurmi and M. A. Berg. Dispersed kinetics without rate heterogeneity in an ionic liquid measured with multiple population-period transient spectroscopy. *J. Phys. Chem. Lett.*, 1:161–164, 2010.
- [44] J. B. Issa, A. S. Salameh, Jr. E. W. Castner, J. F. Wishart, and S. S. Isied. Conformational analysis of the electron-transfer kinetics across oligoproline peptides

- using N,N-Dimethyl-1,4-benzenediamine donors and pyrene-1-sulfonyl acceptors. *J. Phys. Chem. B*, 111:6878–6886, 2007.
- [45] H. Weingärtner, P. Sasisanker, C. Daguenet, P. J. Dyson, I. Krossing, J. M. Slattery, and T. Schubert. The dielectric response of room-temperature ionic liquids: Effect of cation variation?. *J. Phys. Chem. B*, 111:4775–4780, 2007.
- [46] K. A. Fletcher, I. A. Storey, A. E. Hendricks, S. Pandey, and S. Pandey. Behavior of the solvatochromic probes Reichardt’s dye, pyrene, dansylamide, Nile Red and 1-pyrenecarbaldehyde within the room-temperature ionic liquid bmimPF₆. *Green Chem.*, 3:210–215, 2001.
- [47] S. N. V. K. Aki, J. F. Brennecke, and A. Samanta. How polar are room-temperature ionic liquids? *Chem. Commun.*, 5:413–414, 2001.
- [48] P. K. Mandal and A. Samanta. Fluorescence studies in a pyrrolidinium ionic liquid: Polarity of the medium and solvation dynamics. *J. Phys. Chem. B*, 109:15172–15177, 2005.
- [49] R. Karmakar and A. Samanta. Solvation dynamics of coumarin-153 in a room-temperature ionic liquid. *J. Phys. Chem. A*, 106:4447–4452, 2002.
- [50] Y. Shim and H. J. Kim. Free energy and dynamics of electron-transfer reactions in a room temperature ionic liquid. *J. Phys. Chem. B*, 111:4510, 2007.
- [51] Y. Shim and H. J. Kim. Adiabatic electron transfer in a room-temperature ionic liquid: Reaction dynamics and kinetics. *J. Phys. Chem. B*, 113:12964–12972, 2009.
- [52] R. M. Lynden-Bell. Does marcus theory apply to redox processes in ionic liquids? a simulation study. *Electrochem. Commun.*, 9:1857, 2007.
- [53] R. M. Lynden-Bell. Can marcus theory be applied to redox processes in ionic liquids? A comparative simulation study of dimethylimidazolium liquids and acetonitrile. *J. Phys. Chem. B*, 111:10800, 2007.

- [54] H. V. R. Annapureddy and C. J. Margulis. Controlling the outcome of electron transfer reactions in ionic liquids. *J. Phys. Chem. B*, 113:12005–12012, 2009.
- [55] N. Ito, S. Arzhantsev, M. Heitz, and M. Maroncelli. Solvation dynamics and rotation of coumarin 153 in alkylphosphonium ionic liquids. *J. Phys. Chem. B*, 108:5771–5777, 2004.
- [56] R. C. Vieira and D. E. Falvey. Photoinduced electron-transfer reactions in two room-temperature ionic liquids: 1-butyl-3-methylimidazolium hexafluorophosphate and 1-octyl-3-methylimidazolium hexafluorophosphate. *J. Phys. Chem. B*, 111:5023–5029, 2007.
- [57] P. K. Chowdhury, M. Halder, L. Sanders, T. Calhoun, J. L. Anderson, D. W. Armstrong, X. Song, and J. W. Petrich. Dynamic solvation in room-temperature ionic liquids. *J. Phys. Chem. B*, 108:10245–10255, 2004.
- [58] C. Hardacre, J. D. Holbrey, C. L. Mullan, Youngs T. G. A., and D. T. Bowron. Small angle neutron scattering from 1-alkyl-3-methylimidazolium hexafluorophosphate ionic liquids ($[C_n\text{mim}][\text{PF}_6]$, $n = 4, 6$, and 8). *J. Chem. Phys.*, 133:74510, 2010.
- [59] S. M. Urahata and M. C. C. Ribeiro. Structure of ionic liquids of 1-alkyl-3-methylimidazolium cations: A systematic computer simulation study. *J. Chem. Phys.*, 120:1855–1863, 2004.
- [60] M. G. Del Popolo and G. A. Voth. On the structure and dynamics of ionic liquids. *J. Phys. Chem. B*, 108:1744–1752, 2004.
- [61] C. Schröder, T. Rudas, and O. Steinhauser. Simulation studies of ionic liquids: Orientational correlations and static dielectric properties. *J. Chem. Phys.*, 125:244506, 2006.
- [62] C. Schröder, T. Rudas, G. Neumayr, S. Benkner, and O. Steinhauser. On the collective network of ionic liquid/water mixtures. I. Orientational structures. *J. Chem. Phys.*, 127:234503, 2007.

- [63] C. Schröder, M. Haberler, and O. Steinhauser. On the computation and contribution of conductivity in molecular ionic liquids. *J. Chem. Phys.*, 128:134501, 2008.
- [64] H. K. Kashyap, J. J. Hettige, H. V. R. Annapureddy, and C. J. Margulis. Saxs anti-peaks reveal the length-scales of dual positive-negative and polar-apolar ordering in room-temperature ionic liquids. *Chem. Comm.*, 48:5103–5105, 2012.
- [65] C. Hardacre, J. D. Holbrey, S. E. J. McMath, D. T. Bowron, and A. K. Soper. Structure of molten 1,3-dimethylimidazolium chloride using neutron diffraction. *J. Chem. Phys.*, 118:273–278, 2003.
- [66] J. N. Canongia Lopes and A. A. H. Padua. Nanostructural organization in ionic liquids. *J. Phys. Chem. B*, 110:3330–3335, 2006.
- [67] O. Russina and A. Triolo. New experimental evidence supporting the mesoscopic segregation model in room temperature ionic liquids. *Faraday Discuss.*, 154:97–109, 2012.
- [68] H. Tokuda, K. Hayamizu, K. Ishii, M. A. B. H. Susan, and M. Watanabe. Physico-chemical properties and structures of room temperature ionic liquids. 2. Variation of alkyl chain length in imidazolium cations. *J. Phys. Chem. B*, 109:6103–6110, 2005.
- [69] Y. T. Wang, S. Izvekov, T. Y. Yan, and G. A. Voth. Multiscale coarse-graining of ionic liquids. *J. Phys. Chem. B*, 110:3564–3575, 2006.
- [70] W. Zheng, A. Mohammend, L. G. Hines, Jr., D. Xiao, O. J. Martinez, R. A. Bartsch, S. L. Simon, O. Russina, A. Triolo, and E. L. Quitevis. Effect of cation symmetry on the morphology and physicochemical properties of imidazolium ionic liquids. *J. Phys. Chem. B.*, 115:6572, 2011.
- [71] R. Raju and S. Balasubramanian. Role of cation symmetry in intermolecular structure and dynamics of room temperature ionic liquids: Simulation studies. *J. Phys. Chem. B.*, 114:6455, 2010.

- [72] D. Jeong, M. Y. Choi, H. J. Kim, and Y. Jung. Fragility, stokes, einstein violation, and correlated local excitations in a coarse-grained model of an ionic liquids. *Phys. Chem. Chem. Phys.*, 12:2001–2010, 2010.
- [73] R. A. Mantz, P. C. Trulove, R. T. Carlin, and R. A. Osteryoung. ROESY NMR of basic ambient-temperature chloroaluminate ionic liquids. *Inorg. Chem.*, 34:3846–3847, 1995.
- [74] P. J. Dupont, A. Z. Suarez, R. F. De Souza, R. A. Burrow, and J. P. Kintzinger. C–H-pi interactions in 1-n-butyl-3-methylimidazolium tetraphenylborate molten salt: Solid and solution structures. *Chem. Eur. J.*, 6:2377–2381, 2000.
- [75] N. E. Heimer, R. E. Desl Sesto, and R. Carper. Evidence for spin diffusion in a H,H-NOESY study of imidazolium tetrafluoroborate ionic liquids. *Magn. Reson. Chem.*, 42:71–75, 2004.
- [76] A. Mele, C. D. Tran, and S. H. D. Lacerda. The structure of a room-temperature ionic liquid with and without trace amounts of water: The role of C-H center dot center dot center dot O and C-H center dot center dot center dot F interactions in 1-n-butyl-3-methylimidazolium tetrafluoroborate. *Angew. Chem., Int. Ed.*, 42:4364–4366, 2003.
- [77] D. Nama, P. G. A. Kumar, P. S. Pregosin, T. J. Geldbach, and P. J. Dyson. H-1, F-19-HOESY and PGSE diffusion studies on ionic liquids: The effect of co-solvent on structure. *Inorg. Chem. Acta*, 359:1907–1911, 2006.
- [78] F. Castiglione, M. Moreno, G. Raos, A. Famulari, A. Mele, G. B. Appetecchi, and S. Passerini. Structural organization and transport properties of novel pyrrolidinium-based ionic liquids with perfluoroalkyl sulfonylimide anions. *J. Phys. Chem. B*, 113:10750–10759, 2009.
- [79] A. Triolo, O. Russina, R. Caminiti, H. Shirota, H. Y. Lee, C. S. Santos, N. S. Murthy, and E. W. Castner, Jr. Comparing intermediate range order for alkyl- vs. ether-substituted cations in ionic liquids. *Chem. Comm.*, 48:4959–4961, 2012.

- [80] S. Hayashi and H. O. Hamaguchi. Discovery of a magnetic ionic liquid [bmim]FeCl₄. *Chemistry Letters*, 33:1590–1591, 2004.
- [81] S. Hayashi, S. Saha, and H.-o. Hamaguchi. A new class of magnetic fluids: bmim[FeCl₄] and nbmim[FeCl₄] ionic liquids. *IEEE Transactions on Magnetics*, 42:12–14, 2006.
- [82] P. Brown, A. Bushmelev, C. P. Butts, J. Cheng, J. Eastoe, I. Grillo, R. K. Heenan, and A. M. Schmidt. Magnetic control over liquid surface properties with responsive surfactants. *Angew. Chem.*, 51:2414–2416, 2012.
- [83] Y. Yoshida, A. Otsuka, G. Saito, S. Natsume, E. Nishibori, M. Takata, M. Sakata, M. Takahashi, and T. Yoko. Conducting and magnetic properties of 1-ethyl-3-methylimidazolium (EMI) salts containing paramagnetic irons: Liquids [EMI](MCl₄)-Cl-III] (M = Fe and Fe_{0.5}Ga_{0.5}) and solid [EMI]₍₂₎[(FeCl₄)-Cl-II]. *Bul. Chem. Soc. Jpn.*, 78:1921–1928, 2005.
- [84] Y. Yoshida and G. Saito. Influence of structural variations in 1-alkyl-3-methylimidazolium cation and tetrahalogenoferrate(III) anion on the physical properties of the paramagnetic ionic liquids. *J. Mat. Chem.*, 16:1254–1262, 2006.
- [85] M. Okuno, H. Hamaguchi, and S. Hayashi. Magnetic manipulation of materials in a magnetic ionic liquid. *Appl. Phys. Lett.*, 89:132506, 2006.
- [86] O. Yamamuro, Y. Minamimoto, Y. Inamura, S. Hayashi, and H. O. Hamaguchi. Heat capacity and glass transition of an ionic liquid 1-butyl-3-methylimidazolium chloride. *Chem. Phys. Lett.*, 423:371–375, 2006.
- [87] A. P. Abbott, G. Capper, D. L. Davies, and R. Rasheed. Ionic liquids based upon metal halide/substituted quaternary ammonium salt mixtures. *Inorg. Chem.*, 43:3447–3452, 2004.
- [88] R. E. Del Sesto, T. M. McCleskey, A. K. Burrell, G. A. Baker, J. D. Thompson, B. L. Scott, J. S. Wilkes, and P. Williams. Structure and magnetic behavior of transition metal based ionic liquids. *Chem. Comm.*, pages 447–449, 2008.

- [89] C. Guerrero-Sanchez, T. Lara-Ceniceros, E. Jimenez-Regalado, M. Rasa, and U. S. Schubert. Magnetorheological fluids based on ionic liquids. *Adv. Mater.*, 19:1740 – 1747, 2007.
- [90] H. Morimoto, T. Ukai, Y. Nagaoka, N. Grobert, and T. Maekawa. Tumbling motion of magnetic particles on a magnetic substrate induced by a rotational magnetic field. *Phys. Rev.*, 78:021403–1 – 021403–7, 2008.
- [91] F. C. C. Oliveira, L. M. Rossi, R. F. Jardim, and J. C. Rubim. Magnetic fluids based on gamma-Fe₂O₃ and CoFe₂O₄ nanoparticles dispersed in ionic liquids. *J. Phys. Chem. C*, 113:8566–8572, 2009.
- [92] G. Clavel, J. Larionova, Y. Guari, and C. Guérin. Synthesis of cyano-bridged magnetic nanoparticles using room-temperature ionic liquids. *Chem. Eur. J.*, 12:3798 – 3804, 2006.
- [93] K. Bica and P. Gaertner. An iron-containing ionic liquid as recyclable catalyst for aryl grignard cross-coupling of alkyl halides. *Org. Lett.*, 8:733 – 735, 2006.
- [94] G. Wang, N. Yu, L. Peng, R. Tan, H. Zhao, D. Yin, H. Qiu, Z. Fu, and D. Yin. Immobilized chloroferrate ionic liquid: An efficient and reusable catalyst for synthesis of diphenylmethane and its derivatives. *Catal. Lett.*, 123:252–258, 2008.
- [95] S. A. Kozlova, S. P. Verevkin, A. Heintz, T. Peppel, and M. Kockerling. Paramagnetic ionic liquid 1-butyl-3-methylimidazolium tetrabromidocobaltate(II): Activity coefficients at infinite dilution of organic solutes and crystal structure. *J. Chem. Eng. Data*, 54:1524–1528, 2009.
- [96] D. Wyrzykowski, T. Maniecki, A. Pattek-Janczyk, J. Stanek, and Z. Warnke. Thermal analysis and spectroscopic characteristics of tetrabutylammonium tetrachloroferrate(III). *Therm. Acta*, 435:92–98, 2005.
- [97] D. Wyrzykowski, R. Kruszynski, T. Maniecki, and Z. Warnke. Synthesis and

- physiochemical characteristics of new tetrachloroferrates(III) with dimethylammonium cation: X-ray crystal structure of bis(dimethylammonium) chloride tetrachloroferrate(III). *J. Inorg. Gen. Chem.*, 633:285–289, 2007.
- [98] D. Wyrzykowski, R. Kruszynski, J. Klak, J. Mrozinski, and Z. Warnke. Synthesis and physiochemical characteristics of new tetrachloroferrates(III) with dimethylammonium cation: X-ray crystal structure of bis(dimethylammonium) chloride tetrachloroferrate(III). *J. Inorg. Gen. Chem.*, 633:2071, 2007.
- [99] D. Wyrzykowski, T. Maniecki, Maria Gazda, E. Stycze, and Z. Warnke. Thermal properties of tetrabutylammonium bromotrichloro-, tribromochloro- and tetrabromoferrates(III). *J. Therm. Anal. Calorim.*, 3:893–897, 2007.
- [100] D. Wyrzykowski, R. Kruszynski, J. Mrozinski, and Z. Warnke. Structural and magnetic characteristics of tetramethylammonium tetrahalogenoferrates(III). *Inorg. Chim. Acta*, 361:262–268, 2008.
- [101] B. Mallick, B. Balke, C. Felser, and A.-V. Mudring. Dysprosium room-temperature ionic liquids with strong luminescence and response to magnetic fields. *Angew. Chem. Int. Ed.*, 47:7635–7638, 2008.
- [102] S. Tang, A. Babai, and A.-V. Mudring. Europium-based ionic liquids as luminescent soft materials. *Angew. Chem. Int. Ed.*, 47:7631–7634, 2008.

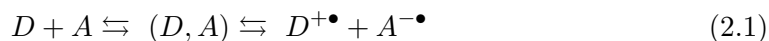
Chapter 2

A Comparison of Electron-Transfer Dynamics in Ionic Liquids and Neutral Solvents

2.1 Background on Electron Transfer

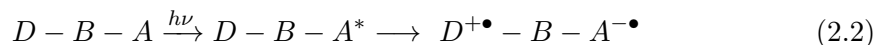
Electron-transfer (ET) reactions have long occupied the attention of leading research groups because of their importance in the biochemistry of life and in technologies for energy capture, storage and use.^{1–7} In particular, intramolecular electron-transfer reactions play critical roles in photosynthesis and respiration, and they are particularly useful for studying the fundamentals of electron transfer because the geometry and coupling of the donor and acceptor groups are often well constrained. To study such systems, many researchers have designed synthetic donor-bridge-acceptor (D–B–A) complexes to serve as controllable models to analyze the factors that control electron transfer, including driving force, reorganization energy, electronic coupling, and dynamical effects.^{5,8–14} Within electron-transfer proteins, peptide residues often serve as bridges in D–B–A systems. Because they are widely available, polypeptides containing proline residues have been especially useful tools for this purpose because the rigidity of the secondary amino acid proline restricts the range of stable polypeptide conformations compared to other amino acids.⁹

Electron-transfer processes can be described as transportation of an electron from a donor (D) to an acceptor (A), and, in general, can be described by the mechanism in Eq. 2.1,



where D represents a donor, A , an acceptor, and (D, A) is the encounter complex within

which the electron transfer occurs. Intramolecular electron-transfer systems, such as D-B-A complexes can be considered as a special type of fixed encounter complex. They are attractive to study because they separate the electron-transfer process from the diffusional process of the reactants and the energy required to form the encounter complex. After photoexcitation in such a system, the acceptor provides a driving force for the electron to leave the donor and travel across the bridge to reduce the excited-state A* acceptor as illustrated below:



where $h\nu$ represents the exciting laser photon energy of frequency, ν .

2.1.1 Marcus Theory

In the 1950s and 1960s, Marcus¹⁵ and other theorists formulated an electron-transfer model emphasizing the role of the structural reorganization of the redox centers and the environment (solvent) surrounding the electron-transfer reaction. This was later developed into quantum mechanical interpretation by Jortner and Bixon.^{16,17} An electron-transfer reaction in the nonadiabatic normal regime can be depicted with a potential energy diagram of the reactant and product as functions of nuclear reorganization coordinates shown in Figure 2.1. The dotted lines in the cross section represent the electronic coupling matrix element H_{DA} between the reactant and the product; ΔG^* is the free energy barrier; ΔG^0 is the driving force of the reaction; and λ is the total reorganization energy of the reaction.

The nonadiabatic (weak electronic coupling) electron-transfer rate can also be defined using the Marcus theory,^{2,3}

$$k_{ET,NA} = \frac{2\pi}{\hbar} |H_{DA}|^2 \frac{1}{\sqrt{4\pi \lambda k_B T}} \exp\left(\frac{-\Delta G^*}{k_B T}\right), \quad (2.3)$$

which is divisible into configurations from the electronic coupling H_{DA} and the Franck-Condon weighted density of states (FCWDS).¹⁸ The FCWDS contains the energetics part of the equation that describes the probability of the donor-acceptor system to reach

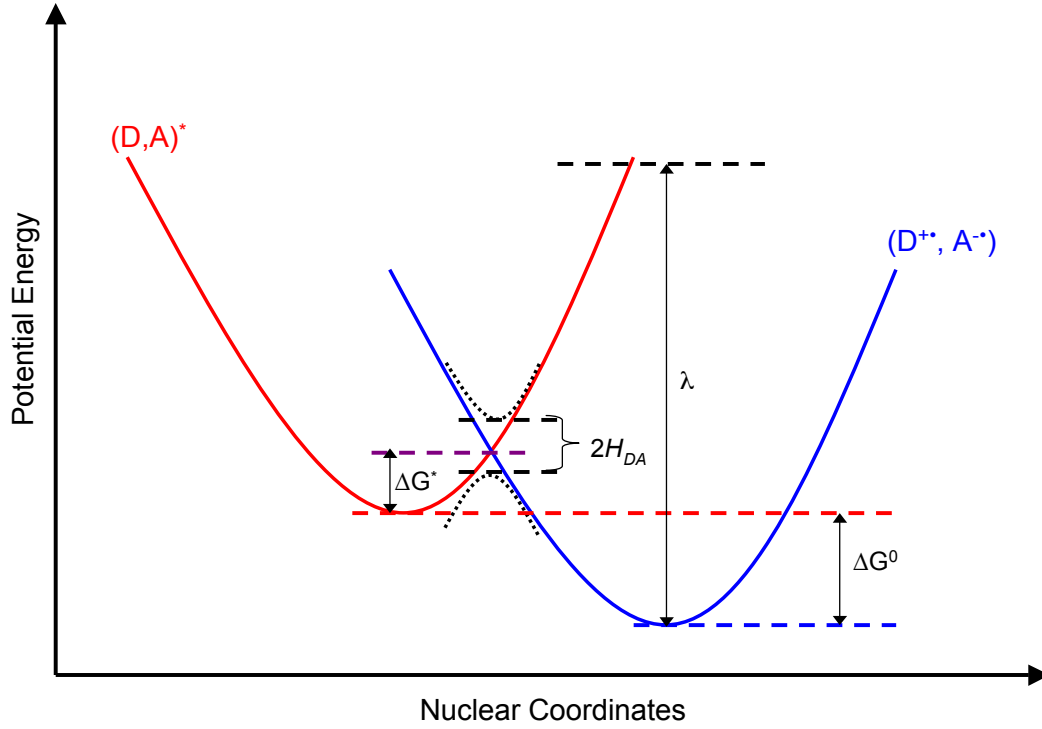


Figure 2.1: Potential energy diagram of electron-transfer reaction between a reactant (D, A) and product (D^+ , A^-) in the normal regime, inspired by Marcus.^{2,3}

the transition state in terms of the nuclear coordinates. Quantum mechanically, the FCWDS describes the overlap of the vibrational states of the donor and the acceptor (see Figure 8 in Ref. 19). Classically, the FCWDS term of the Marcus equation depends on activation energy and the temperature, T . The reaction free energy of activation ΔG^* is defined by

$$\Delta G^* = \frac{(\lambda + \Delta G^0)^2}{4\lambda} \quad (2.4)$$

where λ is the total reorganization energy for the reaction and ΔG^0 is the reaction free energy. Eq. 2.4 reveals that the probability of the reaction is the highest when the driving force $-\Delta G^0$ and the reorganization energy λ are equal. The normal regime of ET reaction is defined as $-\Delta G < \lambda$ and the inverted regime is defined as the region where $-\Delta G > \lambda$ (see for example illustration in Ref. 20).

The classical Marcus equation has been modified quantum mechanically over the

years by many researchers including Jortner¹⁶ and more recently by Subotnik.²¹ Basically, observing the Marcus ET rate equation, one can see that as the driving force $-\Delta G^0$ is increased, the ET rate increases until the maximum rate is reached when $-\Delta G^0$ is equal to λ . After that plateau of ET rate, the ET rate decreases again with increased $-\Delta G^0$. This phenomena, when $-\Delta G^0 > \lambda$, as discussed before, is called the inverted regime and occurs as the product potential well is lowered. The inverted regime is common to intramolecular ET because of the high frequency intramolecular vibrations that the ET molecule possesses.

In the first part of the Marcus equation, the electronic coupling factor H_{DA} , is a function of the electronic coupling of donor and acceptor states and thus depends on the distance and relative orientation variables and their fluctuations.²² For a long distance electron transfer (>5 Å), H_{DA} is closely dependent on the distance of the donor-acceptor; for shorter electron-transfer distances, H_{DA} correlates more strongly with angular orientations than with distance.²³ Recent studies have revealed the importance of the angular orientations, especially for D-B-A electron-transfer compounds containing peptides, because of the effect of their conformational changes on electronic coupling H_{DA} values.^{7,24}

To obtain the donor-acceptor electronic coupling matrix element H_{DA} , the Generalized Mulliken-Hush method²⁵ is used because the method offers an effective and straightforward way for calculating the electronic coupling matrix element for charge-transfer processes. The electronic coupling for a two-state model is defined by

$$H_{DA} = \frac{\mu_{12}\Delta E_{12}}{\left[(\Delta\mu_{12})^2 + 4(\mu_{12})^2\right]^{\frac{1}{2}}}, \quad (2.5)$$

where H_{DA} is the electronic coupling matrix element for nonadiabatic states, ΔE_{12} is the adiabatic excitation energy, which can be obtained experimentally, μ_{12} is the adiabatic transition dipole moment, and $\Delta\mu_{12}$ is the difference in adiabatic state dipole moments. More generally, the electronic coupling for three and more states have been obtained by the model developed by Cave and Newton.²²

For the case of strong electronic coupling (adiabatic regime) the solvent-controlled or adiabatic Marcus equation is used:

$$k_{ET,SC} = \frac{1}{\tau_s} \sqrt{\frac{\lambda}{16\pi k_B T}} \exp\left(\frac{-\Delta G^*}{k_B T}\right), \quad (2.6)$$

where the nonadiabatic Marcus equation (Eq. 2.3) and the adiabatic, solvent-controlled equation (Eq. 2.6) are related via the adiabaticity parameter,

$$g = (4\pi/\hbar)(|H_{DA}|^2 \tau_s/\lambda), \quad (2.7)$$

where the nonadiabatic limit is given by $g \ll 1$, and for strong electronic coupling, the adiabatic or solvent-controlled rate regime is obtained for $g \gg 1$.²⁶ In this equation, τ_s is the solvation time, time that takes the solvent (the environment around the charge transfer) to react to the change.

2.1.2 Electron Transfer in Ionic Liquids

Of the many reasons for studying electron-transfer reactions in ionic liquids (ILs), perhaps foremost is the fact that they are excellent solvents for electrochemistry. The cyclic voltammogram for one of the ionic liquids discussed herein, $\text{Pyr}_{14}^+/\text{NTf}_2^-$, shows a window of 5.3 V between oxidation and reduction of the constituent cation and anion.²⁷ The solvation environment of ionic liquids is complex, combining strongly polar charged and dipolar with hydrophobic interactions. While pure ionic liquids have moderate bulk static dielectric constants typically ranging from 8 to 15,²⁸ they can manifest more strongly polar interactions when results from solvent polarity indicator studies are considered.^{29–32} In several cases, the effective polarity is shown to be similar to neutral solvents like CH_3CN and CH_3OH .^{29,30}

Electron-transfer reactions in ionic liquids are complex for many reasons. Ionic liquids typically have viscosities that are up to thousand times higher than typical organic solvents. The higher viscosities lead to higher activation enthalpy for the solvent

fluidity and slow down the overall solvent reorganization, which is observed in time-resolved spectroscopy of solvatochromic fluorescence studies.^{32–38} In addition to the slower solvation responses observed in ILs, the solvation dynamics in ionic liquids is much more heterogeneous, occurring on timescales that extend up to several ns at temperatures below ambient.^{37,39–41}

The potential effects of ionic liquid media on electron-transfer processes are several fold. First, the ionic environment will alter the thermodynamic stabilities of reactant and product states (driving force) and the work required to bring them to the transition state (reorganization energy). Second, the slower dynamics of solvation in ILs mean that in the cases where the time scales overlap, electron transfer will be occurring over a distribution of solvation states, with a distribution of free energies and reorganization energies. In the extreme case where electron transfer is much faster than solvation, the system should behave like a glass with a much lower effective dielectric constant than the liquid state. Third, it has been shown by experiments and molecular dynamics calculations that ionic liquids are heterogeneous on the molecular scale.^{37,41,42} It is possible that probe molecules may be found in a distribution of environments that will lead to distributed dynamics and kinetics. Each of the above factors will be explored by facets of this work. The energetic profile of electron-transfer reactions in ILs can be inferred by using electrochemical measurements of the reduction potentials of the donor and acceptor and estimated excited state energies to determine the driving force. In addition, temperature-dependent electron-transfer kinetics are studied to obtain activation parameters in order to estimate the reorganization energy.

2.2 Electron Transfer in Ionic Liquids *vs* Neutral Solvents

To make a clearer distinction between the solvent effects on the electron-transfer process in ionic liquids *vs* neutral solvents, we have chosen to eliminate the differences arising from transport phenomena by studying an intramolecular donor–bridge–acceptor (D–B–A) system in two ionic liquids and two neutral solvents. The ionic liquids have the same bis-(trifluoromethylsulfonyl)amide (NTf₂[−]) anion, one with the 1-butyl-1-methylpyrrolidinium (Pyr₁₄⁺) cation and the other with the tributylmethylammonium

(N_{1444}^+) cation; the neutral solvents are CH_3CN and CH_3OH . This choice of solvents makes a set of four liquids with ostensibly similar polarities as estimated from solvent polarity indicators but with very different chemical natures such as molecular sizes and viscosities ranging from <0.3 to $>10^3$ cP for the temperature range 285–324 K. For example, using Reichardt’s betaine-30 dye in $\text{Pyrr}_{14}^+/\text{NTf}_2^-$ and $\text{N}_{1444}^+/\text{NTf}_2^-$, we obtain the effective solvent polarity $E_T(30) = 48.6$ and 46.7 kcal mol $^{-1}$, respectively, whereas for CH_3CN and CH_3OH the values are 45.6 and 55.4 kcal mol $^{-1}$, respectively.^{43,44} The higher $E_T(30)$ value for CH_3OH reflects the known sensitivity of the betaine-30 dye to hydrogen bonding.^{43,44}

The different characteristics of the photophysics and excited-state reactivity of our D–B–A system in neutral solvents *vs* ionic liquids are highlighted in Figure 2.2. The case for the D–B–A photophysics in neutral solvents with low viscosities and fast solvation dynamics is shown in the Jablonski diagram on the left side of the figure. Following vertical excitation, solvent reorganization about the strongly dipolar excited state occurs quite rapidly and electron transfer proceeds from the relaxed state to form the charge-separated product $\text{D}^{+\bullet} - \text{B} - \text{A}^{-\bullet}$. This sequence applies whenever the rate of solvation k_{solv} is much faster than the rate of electron transfer k_{ET} , which is the case for our D–B–A system in CH_3CN and CH_3OH .⁴⁵ The Jablonski diagram on the right side of Figure 2.2 provides a simplified perspective of what happens with our D–B–A system in ionic liquids, where the rates for solvation and electron-transfer are similar ($k_{\text{solv}} \sim k_{\text{ET}}$) and charge separation occurs from a temporally evolving distribution of partially relaxed states.

The solvation dynamics in the two ionic liquids studied here are known to be heterogeneous with nonexponential responses spanning time scales from sub-ps to tens of ns.³⁷ Maroncelli and co-workers have shown similar behavior for a wide variety of ionic liquids.^{40,41,46,47} The slower relaxation of the excited state caused by solvent reorganization in ILs leads to a range of states from which the electron-transfer reaction can originate. The energy landscape controlling the electron-transfer process thus becomes time-dependent. Accordingly, even if the overall averaged polarities of the ionic liquids are similar to those for the neutral solvents, the fact that solvation proceeds over

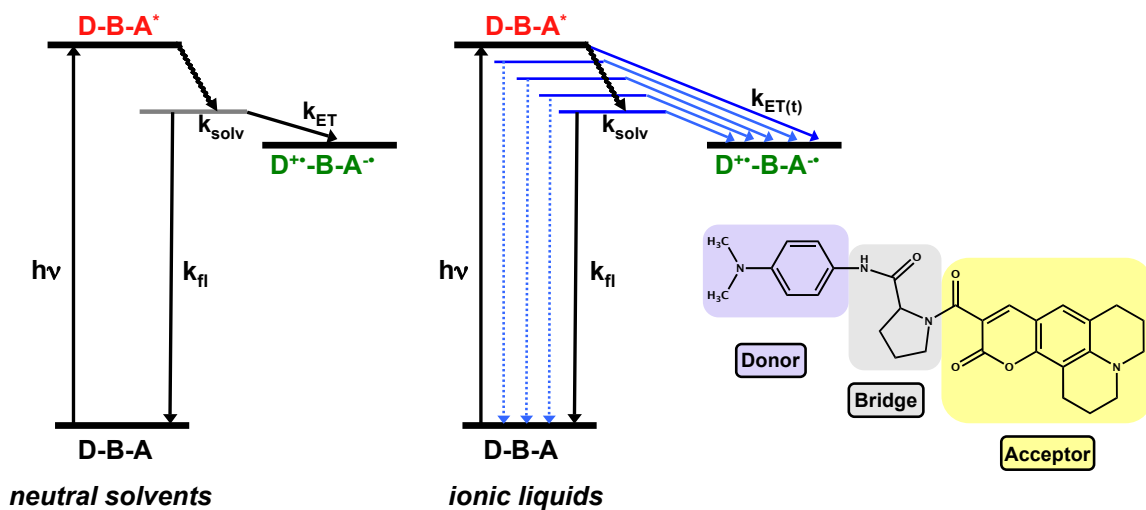


Figure 2.2: Jablonski diagrams for the photophysics of the electron-transfer process for a donor-bridge-acceptor complex in neutral solvents (left) and ionic liquids (right).

time scales that span several orders of magnitude changes the dynamical landscape for the intramolecular electron-transfer reaction. The D-B-A system studied is shown in Figure 2.3; it comprises the 1-N,1-N-dimethyl-1,4-phenylenediamine (DMPD) donor tethered to a proline (Pro) bridge linked to a coumarin 343 (C343) excited-state acceptor, hereafter referred to as DMPD-Pro-C343. As described below, the differences in the one-electron potentials for DMPD donor oxidation $E^0(\text{D}^+/\text{D})$ and C343 acceptor ground-state reduction $E^0(\text{A}/\text{A}^-)$ are 1.0–1.2 V in the four solvents. Because the optical transition energies of the photoexcited C343 acceptor are close to 2.76 eV in all four solvents, this results in free energies for the charge-separation reaction of about -1.6 to -1.9 eV (see following discussions). While photoinduced charge separation in donor-acceptor molecules is usually followed by charge recombination,⁴⁸ we will only discuss the forward charge-separation reaction here, since we have studied the electron-transfer reaction kinetics by measuring the reductive quenching of the photoexcited C343 acceptor emission.

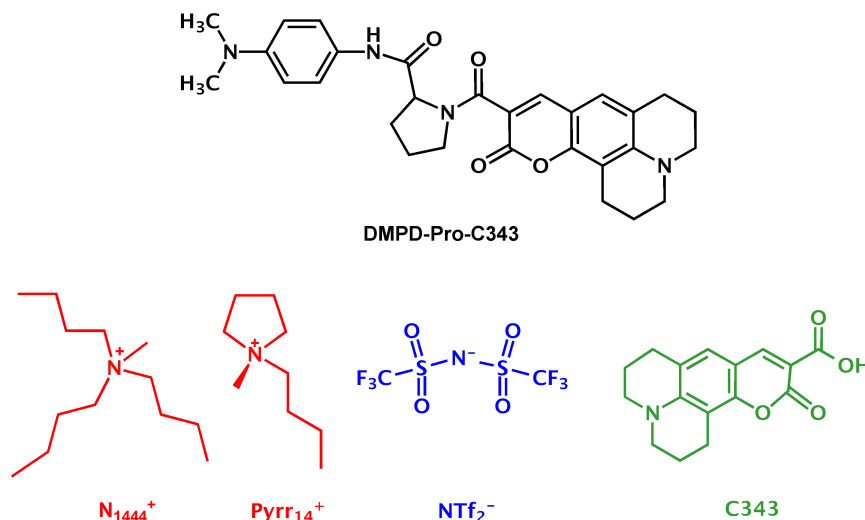


Figure 2.3: DMPD-Pro-C343 (D-B-A complex), coumarin 343, ionic liquid cations Pyr_{14}^+ and N_{1444}^+ , and anion NTf_2^- .

2.3 Experimental Methods

2.3.1 Synthesis and Characterization of DMPD-Pro-C343

All peptide coupling reagents, 1-hydroxybenzotriazole (HOBt), N,N'-dicyclohexylcarbodiimide (DCC), and ethyldiisopropylamine (DIPEA), were purchased from Sigma Aldrich and used as received. The HPLC grade solvents CH_2Cl_2 , CH_3CN , CH_3OH , and toluene were purchased from Sigma Aldrich and used without further purification. Silica gel with pore sizes of 60 Å (230–400 mesh) was purchased from Sigma Aldrich. Coumarins 343 and 314 were purchased from Acros Organics and used as received. 1H NMR spectra were collected using a Varian 400 MHz spectrometer. For mass spectroscopy, a Finnigan LCQ DUO electrospray mass spectrometry instrument with atmospheric pressure ionization source set to detect positive ions was used. The sample was dissolved in methanol with the addition of 2–3 drops of glacial acetic acid for protonation. MS, (ESI $^+$) $[M + H^+]$ Calcd: 501.2; Found: 501.2.

DMPD-Pro-C343 was prepared using standard peptide synthesis methods.⁴⁹ Pro-DMPD was prepared as previously described by Issa *et al.*⁹ Pro-DMPD (40 mg, 0.166 mmol), coumarin 343 (50 mg, 0.175 mmol), DCC (36 mg, 0.175 mmol), HOBt (26 mg, 0.185 mmol), and DIPEA (0.50 mL, 2.87 mmol) were combined in 20 mL of CH_2Cl_2

and stirred overnight. The solvent was then removed by rotary evaporation, and the residue was purified using stationary phase, flash column chromatography with silica gel; dichloromethane/toluene (30/70% by volume) followed by methanol/dichloromethane (5/95%) was used to elute the pure compound. The final mass of DMPD-Pro-C343 obtained was 35 mg (43% yield). DMPD-Pro-C343 evidently decomposes in solution at sustained temperatures above 343 K. This was indicated by color changes of the sample and by disappearance of the parent ion peak in the electrospray-ionization mass spectrum. To avoid sample decomposition, we therefore confined our spectroscopic experiments to the temperature range between 278 and 333 K. The ^1H NMR is shown below in Figure 2.4. ^1H NMR, 400 MHz, CDCl_3 , (ppm): 1.58 (m, 1H); 1.68 (m, 1H); 1.83-2.35 (m-m, 6H); 2.75 (t, 2H); 2.90 (s, 6H); 2.91 (t, 2H); 3.32 (t, 4H); 3.46 (m, 2H); 4.9 (dd, 1H); 6.68 (d, 2H); 6.90 (s, 1H); 7.58 (d, 2H); 7.81 (s, 1H); 9.08 (s, 1H).

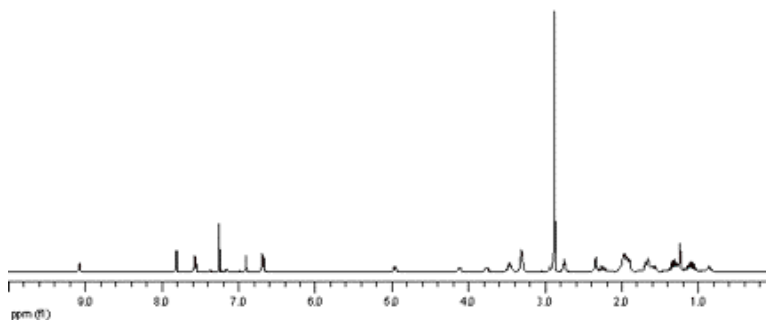


Figure 2.4: ^1H NMR spectrum of DMPD-Pro-C343 molecule.

2.3.2 Preparation of Spectroscopic Samples

High purity $\text{N}_{1444}^+/\text{NTf}_2^-$ was purchased from IoLiTec. Reichardt's dye (betaine-30) was purchased from Sigma Aldrich. The neat ionic liquid $\text{Pyrr}_{14}^+/\text{NTf}_2^-$ was a gift from Dr. Marie Thomas, Brookhaven National Laboratory. It was synthesized using the method of Burrell et al.⁵⁰ which enables production of ILs with greatly suppressed autofluorescence compared to other preparation methods. The negligible autofluorescence of both ILs was checked using UV-vis and fluorescence spectroscopy. All samples were directly prepared in 4-10 mm fused silica cuvettes (Type-505FL, NSG Precision Cells). The concentration of the samples was adjusted for absorbance values less than

0.1 at the excitation wavelengths. Absorption spectra were measured with a Cary-Varian model 50 spectrophotometer. The absorption maxima for DMPD-Pro-C343 at room temperature were 422 nm ($\text{Pyrr}_{14}^+/\text{NTf}_2^-$), 425 nm ($\text{N}_{1444}^+/\text{NTf}_2^-$), 420 nm (CH_3CN), and 426 nm (CH_3OH) as shown in Figure 2.5. The water content of each IL sample was measured to be < 30 ppm using a Denver Instruments Model 260 coulometric Karl Fischer titrator. The samples were evacuated for < 24 hrs. and then backfilled with argon. To maintain low water content in the spectroscopy samples, the cuvettes were covered with rubber septa and sealed with beeswax.

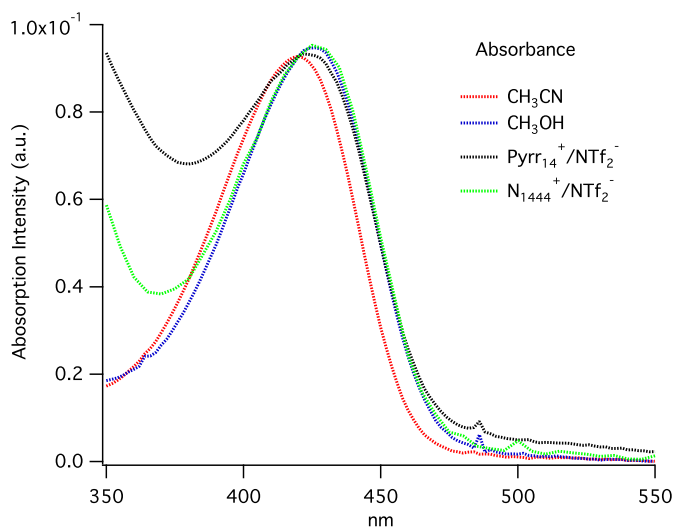


Figure 2.5: Steady-state absorption spectra of DMPD-Pro-C343 in $\text{Pyrr}_{14}^+/\text{NTf}_2^-$, $\text{N}_{1444}^+/\text{NTf}_2^-$, CH_3CN and CH_3OH at ambient temperature.

2.3.3 Electrochemical Measurements

All of the electrochemical measurements were done at The University of Mississippi by Ms. Yunfeng Pan, under the direction of Prof. Hussey. Cyclic staircase voltammetry (CSV) experiments were carried out with a Princeton Applied Research (PAR) Model 263A potentiostat/galvanostat controlled with PAR Model 270 electrochemical software at a step size of 2 mV, as described previously.⁵¹ Measurements were performed in a BASi VC-2 voltammetry cell assembly, which was partially immersed in a water bath with the temperature maintained at 298.2 ± 0.1 K. The small Pt wire counter-electrode provided with this commercial cell was replaced with a much larger surface area Pt foil electrode constructed in-house. The working electrode was a BASi MF-2013 glassy carbon (GC) disk electrode (3.2 mm dia.), and the reference electrode was a BASi MF-2062 nonaqueous Ag^+/Ag electrode. All potentials are reported versus $E_{1/2}$ of the ferrocenium/ferrocene (Fc^+/Fc) couple measured versus this reference electrode in each solvent, as shown below in Figure 2.6. The voltammograms reported herein were collected at a scan rate of 50 mV s^{-1} . Positive feedback resistance compensation was employed during all experiments. The voltammetry cell was sparged with ultra pure N_2 before each experiment, and a continuous blanket of N_2 was maintained above each solution during the measurements. The preparation and purification of $\text{Pyrr}_{14}^+/\text{NTf}_2^-$ and $\text{N}_{1444}^+/\text{NTf}_2^-$ used for the electrochemical experiments were described in a recent article.⁵¹ CH_3CN and CH_3OH (both Fisher Certified ACS) were dried by distillation from CaH_2 and $\text{Mg}(\text{OMe})_2$, respectively. The supporting electrolyte for experiments conducted with the conventional organic solvents was 0.1 M tetrabutylammonium hexafluorophosphate.

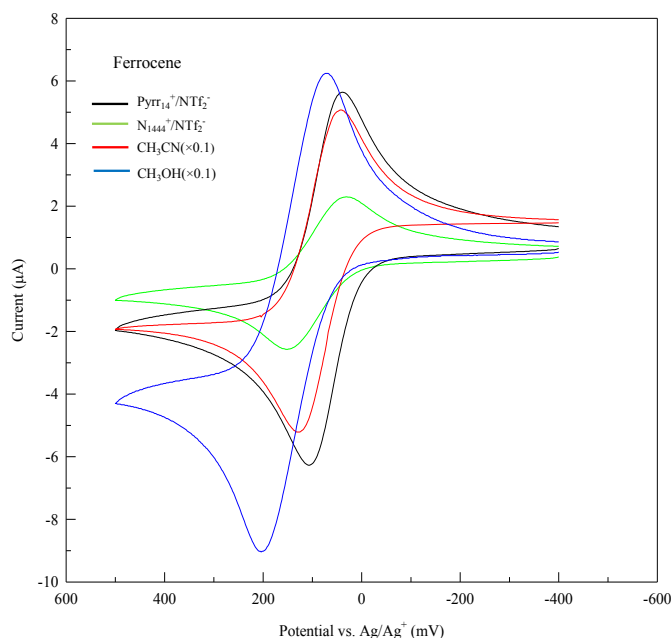


Figure 2.6: Cyclic Voltammogram of ferrocene in the four solvents. Observed $E_{1/2}$ values are 73 mV (Pyr₁₄⁺/NTf₂⁻), 92 mV (N₁₄₄₄⁺/NTf₂⁻), 85 mV (CH₃CN) and 138 mV (CH₃OH) versus the Ag^{+/0} reference electrodes.

2.3.4 Time-Integrated Emission Spectroscopy

A Spex Fluoromax-3 fluorometer was used to measure steady-state fluorescence excitation and emission spectra. Each sample was excited at its absorbance maximum, and both the excitation and emission slits were set for 1.0 nm optical bandpass. Emission maxima for DMPD-Pro-C343 at room temperature were 479 nm (Pyr₁₄⁺/NTf₂⁻), 472 nm (N₁₄₄₄⁺/NTf₂⁻), 478 nm (CH₃CN), and 481 nm (CH₃OH). The normalized steady-state emission spectra are available in Figure 2.7.

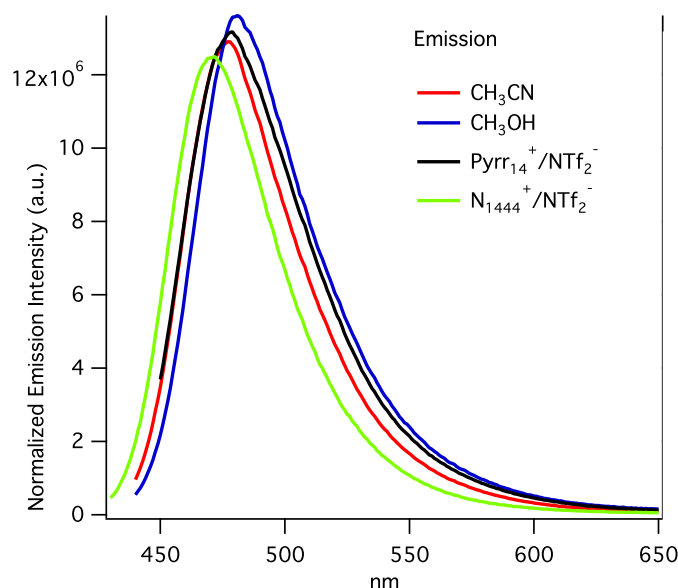


Figure 2.7: Steady-state emission spectra of DMPD-Pro-C343 in $\text{Pyr}_{14}^+/\text{NTf}_2^-$, $\text{N}_{1444}^+/\text{NTf}_2^-$, CH_3CN and CH_3OH at ambient temperature.

2.3.5 Time-Resolved Emission Spectroscopy

The time-resolved emission data were measured using the time-correlated single-photon counting (TCSPC) technique with a the Spectra Physics Tsunami Ti/sapphire laser with frequency doubled output (430 nm) as the excitation source. A Pockels cell was used to select pulses at 13.7 MHz. The 4096-channel Becker and Hickl SPC-630 TCSPC instrument processes the signals from a Hamamatsu R3809-50U microchannel plate photomultiplier. The equipment used for this study is shown schematically in Figure 2.8; a more detailed description of this apparatus has been described previously.^{23,52–54} The experimental time window was set to 70 ns to capture the complete transient including decay to baseline levels, and the instrument response was typically 70–90 ps (fwhm). The excitation wavelengths of DMPD-Pro-C343 used for time-resolved emission spectra were selected to minimize excess vibronic energy in the excited state while avoiding photoselection of states that would likely display red-edge excitation effect phenomena. On the basis of the steady-state fluorescence results, an excitation wavelength of 430 nm was chosen for DMPD-Pro-C343 TCSPC experiments in each of the four solvents.

Detailed discussion on Stokes shift analysis is described in the following sections. Emission wavelengths for TCSPC experiments on DMPD-Pro-C343 were chosen to be 481 nm ($\text{Pyrr}_{14}^+/\text{NTf}_2^-$), 490 nm ($\text{N}_{1444}^+/\text{NTf}_2^-$), and 480 nm (CH_3CN and CH_3OH). The goal in selecting these particular emission wavelengths was to minimize the contributions that arise from the time-dependent fluorescence Stokes shift that occurs for solvatochromic molecules.³⁷ Coumarin 314 (C314, the ethyl ester of C343; structure shown in Figure 2.9) was estimated to be a sufficiently close solvatochromic model system for the DMPD-Pro-C343 molecule by virtue of its structural similarity to C343. Thus, for each of the two ILs, the fluorescence Stokes shift for C314 was characterized by measuring 10–15 emission wavelengths at room temperature. In each decay, a fast component was identified in the dynamics that had a relatively large amplitude - a rapid decay for the bluest wavelengths and a rapid rise time for the reddest wavelengths. Following a multiexponential analysis of each of these decays, we determined that a five-exponential model function was required to fit the extreme red and blue wavelengths, while a nearly single-exponential response was observed for only a single wavelength near the center of the emission spectrum. This central wavelength balances the rapid decays against the rapid rise times, leading to a nearly exponential response that thus minimizes the effects from solvation dynamics. This is the wavelength that was used for the electron transfer experiments on DMPD-Pro-C343. We note that, while the solvation dynamics are strongly temperature-dependent, the central point of the solvation response is not, so the central wavelength described above does not vary noticeably with temperature.

2.3.6 TCSPC Data Analysis

The TCSPC transients for DMPD-Pro-C343 are strongly nonexponential on all observed time scales. Thus, the simple approach of measuring the intramolecular reductive quenching rate by observing an exponential decay profile faster than the excited-state lifetime of coumarin 314, the nonreactive model for DMPD-Pro-C343, is not sufficient for analyzing the electron-transfer kinetics. We adopt two approaches to model the

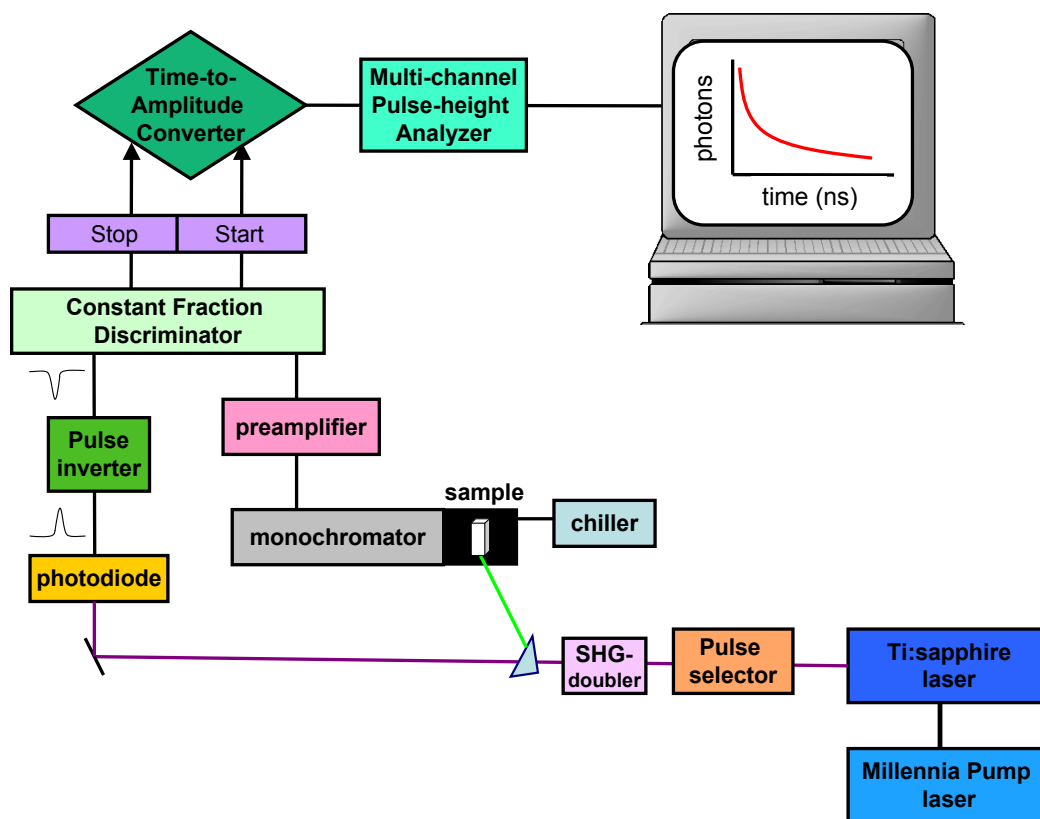
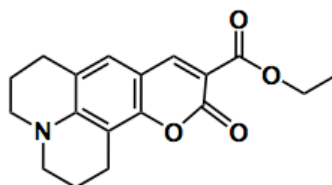


Figure 2.8: Time-correlated single-photon counting system setup used for this study, inspired by Becker and Hickl.⁵⁵ (SHG: Second-harmonic generation)



C314

Figure 2.9: Coumarin 314 (C314) is the ethyl ester of C343. It was selected as a suitable control molecule (than untruncated C343) to compare its redox and photophysical properties with the prolyl-C343 moiety of the DMPD-Pro-C343 electron transfer system, while lacking the ability to undergo intramolecular electron transfer.

fluorescence dynamics. Numerical methods for fitting the data to both models were implemented in MATLAB.⁵⁶ The first method uses the standard multiexponential model with a convolute-and-compare algorithm to incorporate the measured instrument temporal response into the analysis. Up to five exponential decay terms were used to fit to the TCSPC transient intensity $I(t)$, given by

$$I(t) = \sum_{j=1}^5 A_j \int_0^{t_f} e^{-(t-p)/\tau_j} R(p) dp \quad (2.8)$$

where t means time, τ_j is the decay time constant for the j th exponential function, A_j is the amplitude of the j th exponential function, and R represents the instrument response function, which vanishes outside the interval $[0, t_j]$. Fits are deemed satisfactory when the reduced residuals oscillate randomly about zero and the reduced chi-squared value χ_R^2 is in the range from 1.00 to 1.04. Typical TCSPC transients and their reduced residuals are shown in Figure 2.10.

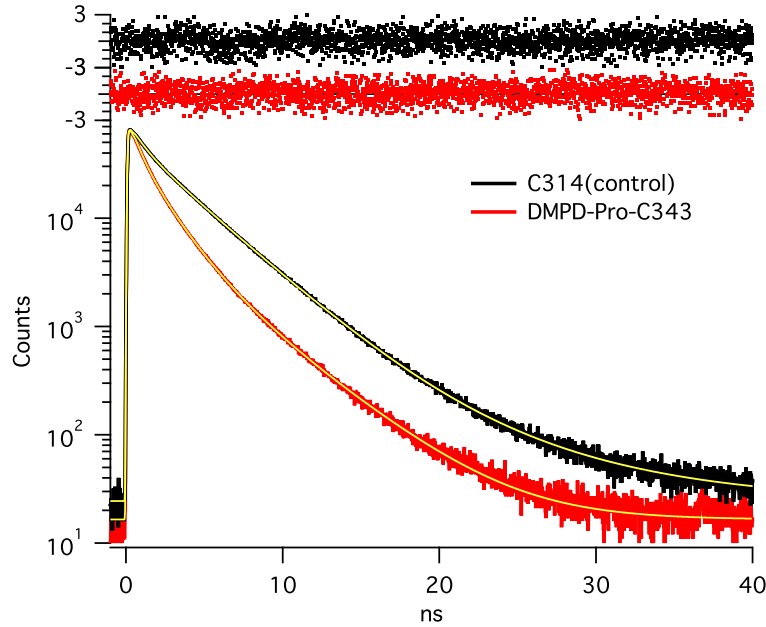


Figure 2.10: TCSPC transients for C314 (control) and DMPD-Pro-C343 in $\text{Pyrr}_{14}^+/\text{NTf}_2^-$ at 293.2 K, using 430 nm laser excitation and 470nm (C314) and 481nm (DMPD-Pro-C343) emission. The TCSPC data are shown in black for C314 and red for DMPD-Pro-C343, with the best fits to five-exponential models shown in yellow lines and with the reduced residuals plotted at the top.

Because the fluorescence decay time constants span two orders of magnitude with an approximately log-spaced distribution of rates, we also fitted the TCSPC transients

to a distribution model. Distribution models are widely used to analyze fluorescence dynamics in a variety of systems.⁵⁷ Following Steinbach, the distribution model is fit to the time-dependent intensity function below

$$I(t_i) = \int_{-\infty}^{\infty} g(\log\tau) \left(\int_0^{t_f} e^{-(t-p)/\tau} R(p) dp \right) d \log\tau \quad (2.9)$$

where $g(\log\tau)$ is the distribution function of decay time constants τ .⁵⁷ In this study, a linear combination of Gaussian functions was assumed as the functional form for $g(\log\tau)$. The fit to this model can be minimized using the value of the reduced chi-squared value parameter χ_R^2 ; however, Steinbach and others have shown that a regularizer incorporating both a maximum entropy and a reduced chi-squared term leads to stable distribution fits.^{57–59} Using the optimized distribution fits initially seeded by the five-exponential decay model leads to distribution fits with reduced chi-squared values also in the range from 1.00 to 1.04. Thus, both multiple-exponential and distribution fit models provide statistically excellent representations of the excited-state decays of DMPD–Pro–C343. The distribution fits provide a qualitative understanding of the similarities and differences in the analyses of electron-transfer quenching of the DMPD–Pro–C343 excited state. At the same time, the discrete five-exponential model is convenient for discriminating between the part of the overall decay that can be assigned to electron transfer *vs* the small to modest contribution to the emission transient that arises from molecules that do not undergo electron transfer within the excited state lifetime. The MATLAB fitting code for both the discrete and distributed exponential fits was tested by comparing with results from our previously validated convolute-and-compare code implemented in Igor Pro⁶⁰ and described previously.³⁷ Additional validation of the fitting software is done by recovering the input parameters for simulated nonexponential data with added Poisson noise. Details about the distribution fitting method are provided in the Appendix.

2.4 Results and Discussion

2.4.1 Evaluation of Electron Donor-Acceptor Interactions

The following calculations of H_{DA} were done by Joe B. Issa. There are several theoretical methods for evaluating the donor-acceptor electronic coupling H_{DA} .^{22,61–63} For these studies, we evaluated H_{DA} using the three-state generalized Mulliken-Hush model that incorporates the dipole moments of the diabatic ground, photoexcited, and charge separated states and the transition dipole matrix elements between these states.²² These states are labeled in Figure 2.2 as ground state (D–B–A, black), photoexcited state (D–B–A*, red), and charge separated state (D⁺•–B–A[–]•, green). Values for the energies, permanent state dipole moments, and transition dipole matrix elements for our system were obtained from single-point CIS calculations using the semi-empirical INDO/S Hamiltonian.⁶⁴ The geometries for the single-point calculations were obtained from semi-empirical optimizations using the AM1 Hamiltonian.⁶⁵

To address the question of how much the value of H_{DA} will vary with solvent, we will consider the two extremes of no solvent (gas phase) and of aqueous solution. Two standard choices are available for implementing solvation models in electronic structure calculations: inclusion of specific solvent molecules or the use of a dielectric cavity model such as the default polarized continuum model used in Gaussian 09, IEFPCM.⁶⁶ To include explicit water molecules in the simulation, a periodic box of 1,500 water molecules containing one DMPD–Pro–C343 molecule was used. The minimized structure of DMPD–Pro–C343 obtained by molecular mechanics energy minimization at 300 K using the CHARMM/Bio+ force field⁶⁷ was either used directly with no solvent model (for comparison with the gas-phase result), with the IEFPCM dielectric cavity model, or with a periodic box of 1,500 water solvent molecules. Results from the four H_{DA} calculations are given in Table 2.1. Re-optimization of the gas-phase structure to the most probable minimum energy structure in aqueous solution using B3LYP/6-311+G(d,p) in Gaussian 09 provided H_{DA} values of 120 *vs* 121 cm^{–1}, respectively; however, inclusion of either the dielectric cavity or explicit water solvent models lead to increases in H_{DA} of about 50 and 100%, respectively.

Table 2.1: Donor-Acceptor Electronic Coupling from INDO/S CIS calculations.^a

Opt. Method (solvent model)	CIS solvent model	H_{DA} (cm ⁻¹)
AM1 (none)	none	120 ^b
CHARMM/Bio+ (periodic box)	none	121 ^c
AM1 (PCM, H ₂ O, $\epsilon_R=78$)	PCM (H ₂ O, $\epsilon_R=78$)	186 ^c
CHARMM/Bio+ (periodic box)	periodic box	231 ^c

^a DMPD-Pro-C343 molecule optimized in a box of 1,500 water molecules, 300 K, CHARMM/Bio+ force field.⁶⁷

^b The resonance integral for oxygen is -54.00 eV, and one electron center energy is -15.88 eV.

^c The resonance integral for oxygen is -34.00 eV and one electron center energy is -17.28 eV.⁶⁸

All values of the electronic coupling H_{DA} were calculated using the ZINDO-MN 1.2 program.^{64,65,68} The values of ΔE_{12} , μ_{12} , and $\Delta\mu_{12}$ used as input for the three-state GMH model⁶⁹ were obtained from electronic-structure calculations using the INDO/S semi-empirical Hamiltonian, where H_{DA} was calculated using the three-state generalized Mulliken-Hush model.²² The value calculated for H_{DA} was at least 120 cm⁻¹. The estimated adiabatic threshold calculated using Zusmans method²⁶ is 120-150 cm⁻¹ for CH₃CN, which indicates that the electron-transfer reaction within the DMPD-Pro-C343 system is likely to be in the adiabatic regime. These values are similar to the estimates of 150 cm⁻¹ used previously for chemically similar systems.²³ Given the large estimated value of H_{DA} for the expected equilibrium conformation, the possibility of intramolecular conformational gating of electron transfer is unlikely for this D-B-A complex.

2.4.2 Estimation of the Driving Forces for the Electron-Transfer Reactions

The driving force for photoinduced electron transfer from DMPD to the coumarin 343 excited state within the D-B-A complex is given by

$$\Delta G^0 = N_A \{e[E^0(D^{+\bullet}/D) - E^0(A/A^{-\bullet})] + w_{D^{+\bullet}A^{-\bullet}} - w_{DA}\} - \Delta E_{0,0} \quad (2.10)$$

where N_A is Avogadro's number, $[E^0(D^{\bullet+}/D) - E^0(A/A^{\bullet-})]$ is the difference between the donor oxidation and acceptor reduction potentials, and the $\Delta E_{0,0}$ term represents the electronic transition energy from the ground state to the vibrationally equilibrated excited state.⁷⁰ The electrostatic work terms $w_{xy} = e^2 z_x z_y / (4\pi\epsilon_0 R_{DA})$ account for the Coulombic interactions between the donor and acceptor in their original and charge-separated states, where z_x and z_y are the respective charges, ϵ_0 is the vacuum permittivity, and R_{DA} is the donor-acceptor distance. Since the donor and acceptor are originally uncharged, $w_{DA} = 0$. The dielectric constant ϵ_s for the ionic liquids is taken for the sake of argument to be 12²⁸ and $\epsilon_s = 33$ and 36, respectively, for CH₃OH and CH₃CN at 298 K.^{71,72} A donor-acceptor distance of 10.4 Å was obtained from the geometry-optimized model using DFT-B3LYP/6-311+G(d,p) in the gas phase, as shown in Figure 2.12. The centers of mass for the donor and acceptor moieties were chosen from separately geometry-optimized DMPD and C343 molecules using the same level of calculation, as shown in Figure 2.11.

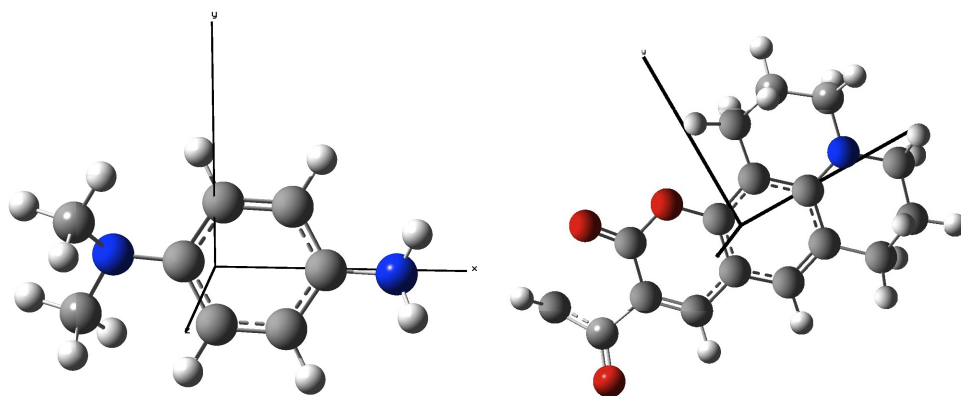


Figure 2.11: DMPD and coumarin 343 geometry was obtained from DFT calculations at the B3LYP/6-311+G(d,p) level of theory.

The oxidation and reduction processes of the DMPD-Pro-C343 complex were examined in each of the four solvents using cyclic staircase voltammetry (CSV) in order to obtain $[E^0(D^{\bullet+}/D) - E^0(A/A^{\bullet-})]$ (see Figure 2.13). In addition to the intact D-B-A complex, CSV data for the model compounds coumarin 314 and 1-*N*,1-*N*-DMPD were obtained for comparison purposes (see Figure 2.14). All of the CSV data in Figure 2.13 and 2.14 are plotted versus the Fc^+/Fc couple in each respective solvent as reported in

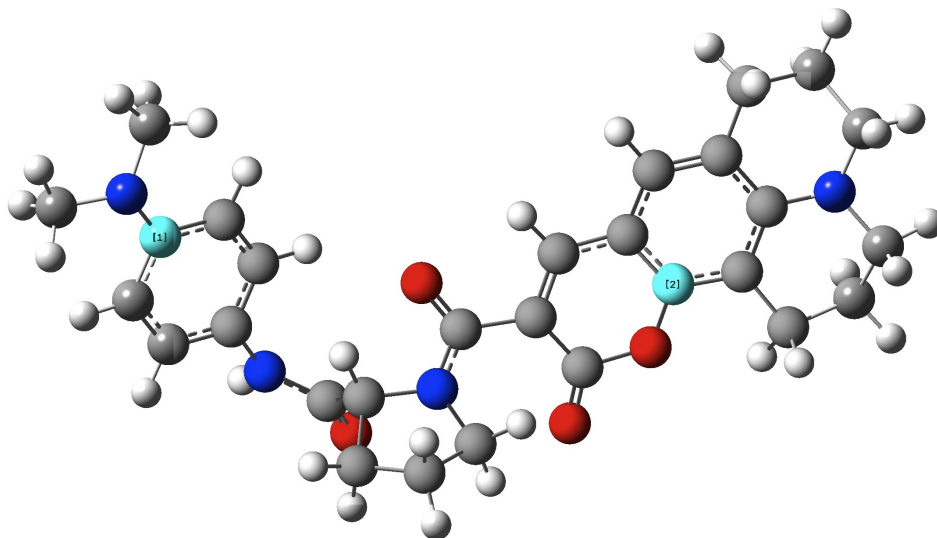


Figure 2.12: DMPD-Pro-C343 geometry optimized using B3LYP/6-311+G(d,p) in Gaussian 09.⁶⁶ The distance measured between the two light blue atoms labeled [1] and [2] is 10.4 Å; these atoms are the ones nearest the center of mass for DMPD and C343, respectively.

Figure 2.6. Compared to the model complexes, the DMPD-Pro-C343 complex shows a coumarin reduction wave at significantly lower potential in each solvent, and the oxidation waves in CH₃CN and CH₃OH appear to be involved with some type of surface process at the glassy carbon electrode. Since the nonideality of the DMPD-Pro-C343 complex electrochemistry makes it hard to define the E^0 values for each redox wave, the differences in the voltammetric peak potentials of the reduction waves and corresponding first oxidation waves in Figure 2.13 were used to obtain an approximation of the $[E^0(D^{+\bullet}/D) - E^0(A/A^{-\bullet})]$ values for DMPD-Pro-C343. The results are collected in Table 2.2, and they show that the potential differences vary from 1.0 to 1.2 V across these four solvents. The other parameters in Table 2.2 will be discussed subsequently.

Table 2.2: Thermodynamic, Activation, and Marcus Equation Parameters for Photoinduced Charge Separation in DMPD-Pro-C343.

Solvent	ΔE_{D-A}^0 (V)	$\Delta E_{0,0}$ (eV)	$w_{D^{+\bullet}A^{-\bullet}}$ (eV)	ΔG_{est}^0 (eV)	$E_{a,ET}$ (eV)	ΔG^*	λ (eV)	λ_o (eV)	$E_{1/\eta}$ (eV)
Pyrr ₁₄ ⁺ /NTf ₂ ⁻	0.99	2.77	-0.115	-1.90	0.173	0.184	1.03	0.145	0.344 ^a
N ₁₄₄₄ ⁺ /NTf ₂ ⁻	1.01	2.76	-0.115	-1.87	0.156	0.169	1.03	0.175	0.527 ^a
CH ₃ OH	1.01	2.76	-0.042	-1.79	0.079	0.092	1.14	0.166	0.083 ^b
CH ₃ CN	1.19	2.75	-0.038	-1.60	0.070	0.083	1.02	0.179	0.113 ^b

^a Reference Funston2007

^b Reference Viswanath2007

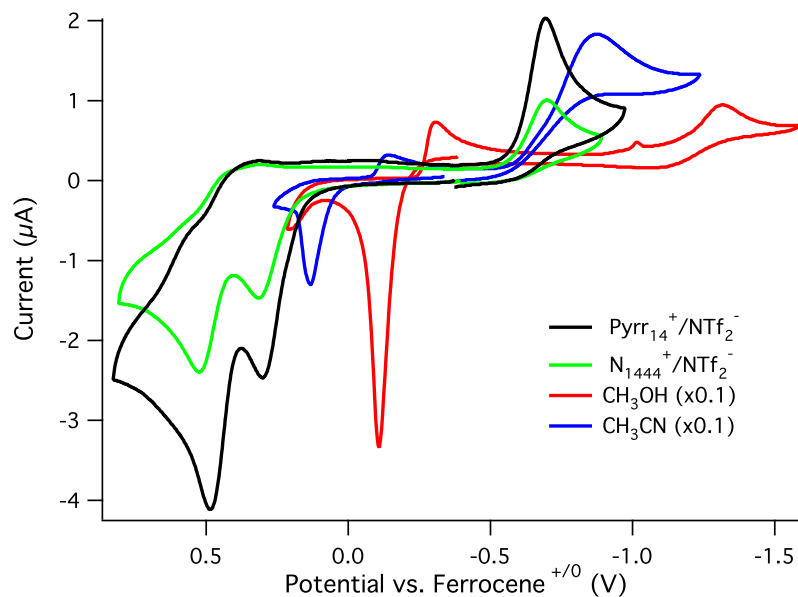


Figure 2.13: Cyclic staircase voltammograms of DMPD-Pro-C343 in $\text{Pyrr}_{14}^+/\text{NTf}_2^-$, $\text{N}_{1444}^+/\text{NTf}_2^-$, CH_3CN and CH_3OH . All scans are referenced to the $E_{1/2}$ values of the ferrocenium/ferrocene couple in each respective solvent.

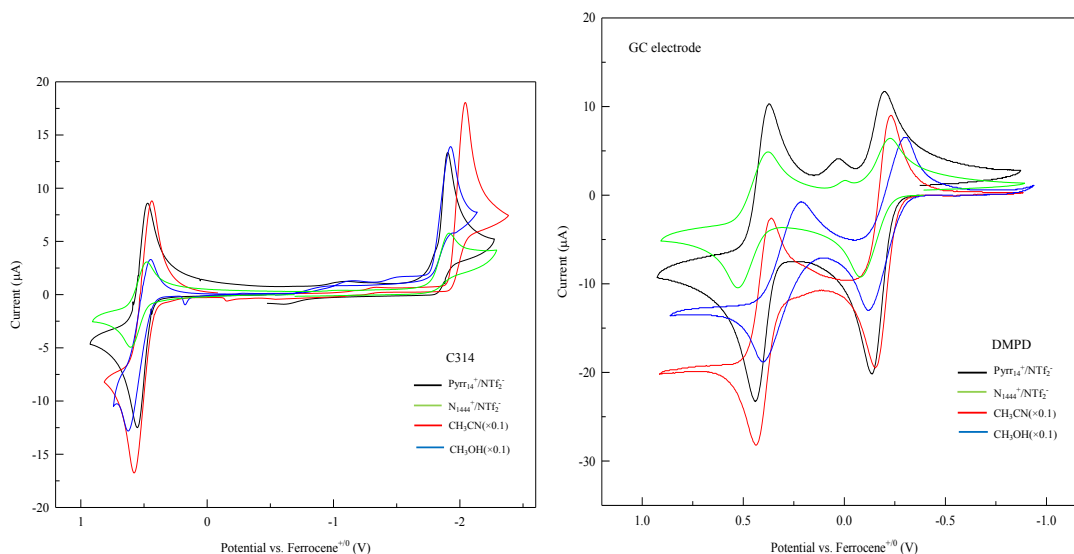


Figure 2.14: Cyclic staircase voltammograms of coumarin 314 and DMPD in $\text{Pyrr}_{14}^+/\text{NTf}_2^-$, $\text{N}_{1444}^+/\text{NTf}_2^-$, CH_3CN and CH_3OH . The scan rate was 50 mV s^{-1} and the potential step size was 2 mV. All scans are referenced to the ferrocenium/ferrocene couple.

2.4.3 Steady-State Fluorescence Spectroscopy of DMPD-Pro-C343

Steady-state fluorescence spectra of DMPD-Pro-C343 display solvatochromic behavior similar to coumarin 343⁷³ and other 7-aminocoumarins such as coumarin 153.⁴⁵ The differences in peak frequencies for absorption and emission of DMPD-Pro-C343 at room temperature are 2820 cm⁻¹ (Pyrr₁₄⁺/NTf₂⁻), 2340 cm⁻¹ (N₁₄₄₄⁺/NTf₂⁻), 2890 cm⁻¹ (CH₃CN), and 2680 cm⁻¹ (CH₃OH). The observed shift is smaller in the case of N₁₄₄₄⁺/NTf₂⁻ because the average solvation time in that ionic liquid at room temperature is comparable to the C343 emission lifetime. The cause of the positive solvatochromic shift is the increase in dipole moment on going from the polar ground state to the more polar excited state. The ground and excited state dipole moments were calculated for DMPD-Pro-C343, C343 and C314 using INDO/S with AM1 geometry optimization with ArgusLab⁷⁴ and solvation model parameters for CH₃CN (see Table 2.3 for complete results). The ground-state values are 10.4 D (DMPD-Pro-C343) and 10.5 D (C343). For each of these two molecules, the dipole moment not only increases in magnitude on photoexcitation to the first singlet excited state but also changes direction. The relevant number to consider then is the magnitude of the change in dipole moment, $\Delta\mu = |\vec{\mu}_{es} - \vec{\mu}_{gs}|$; these are 5.83 D (DMPD-Pro-C343) and 8 (C343).⁴¹

Table 2.3: Values for the dipole moments in the ground and excited electronic states are listed together with the magnitudes of their vector differences for C314, C343 and DMPD-Pro-C343.

Molecule	Solvent	$ \vec{\mu}_{g.s.} $	$ \vec{\mu}_{e.s.} $	$ \vec{\mu}_{e.s.} - \vec{\mu}_{g.s.} $
C314	None	9.18	15.6	7.05
C314	CH ₃ CN	11.1	18.7	8.21
C343	None	8.57	14.7	6.72
C343	CH ₃ CN	10.5	18.0	8.13
DMPD-Pro-C343	None	9.94	13.4	5.39
DMPD-Pro-C343	CH ₃ CN	10.4	14.2	5.83

These results were obtained from calculations done using the INDO-MN program⁶⁸ on geometries optimized using the AM1 Hamiltonian run using ArgusLab 4.0.⁷⁴

The temperature-dependent fluorescence excitation spectra of DMPD-Pro-C343 in

the two ionic liquids are different than those for the two neutral solvents (see Figures 2.15 and 2.16). In the studied ionic liquids, DMPD-Pro-C343 shows similar emission maxima shifts with those of coumarin 153,³⁷ with the emission spectra maxima generally red shifting with increasing temperature. We note that the shift of emission spectrum of $\text{Pyrr}_{14}^+/\text{NTf}_2^-$ at 271 K could be due to a phase change (Henderson and Passerini have reported the melting point of 270 K for $\text{Pyrr}_{14}^+/\text{NTf}_2^-$.⁷⁵) As the temperature is increased, the bluer side of the emission spectra starts to contribute less, red shifting the emission spectra. This is an evidence that the solvation time plays a great role for viscous solvents such as ILs. The solvent relaxation in CH_3OH and CH_3CN is complete within a few ps.⁴⁵ Since the solvation time scales in these solvents are very short relative to the excited-state lifetime, the time-integrated emission spectra are dominated by emission from the fully solvated excited state. The peak emission wavelengths are nearly temperature-independent, and variation of the excitation wavelengths does not lead to an observed shift in the peak of the emission spectra. Solvation dynamics in ionic liquids span a broader range of time scales that extend up to several nanoseconds at lower temperatures.^{37,40,46,47} As the temperature increases, the solvation dynamics in the ionic liquids become faster than the emission time window defined by the electron transfer in DMPD-Pro-C343, so the integrated emission spectra become further red-shifted.

Effect of Excitation Wavelength on Photoinduced Electron-Transfer of DMPD-Pro-C343

The red-edge effect (REE) is a red-shift of emission maxima with the increasing excitation wavelength observed in glass-like assemblies at low-temperatures. This behavior is caused by either the inhomogeneous distribution of energetically different dipolar molecules in the glass-like media, producing an absorption spectrum that is inhomogeneously broadened or by heterogeneous relaxation processes from excited states of the dipolar molecules. A good review of red-edge effects was written by Demchenko.⁷⁶ The REEs of an imidazolium based IL have been described both experimentally and theoretically by other groups including Samanta *et al.*^{42,77} and Hu and Margulis.^{78–80}

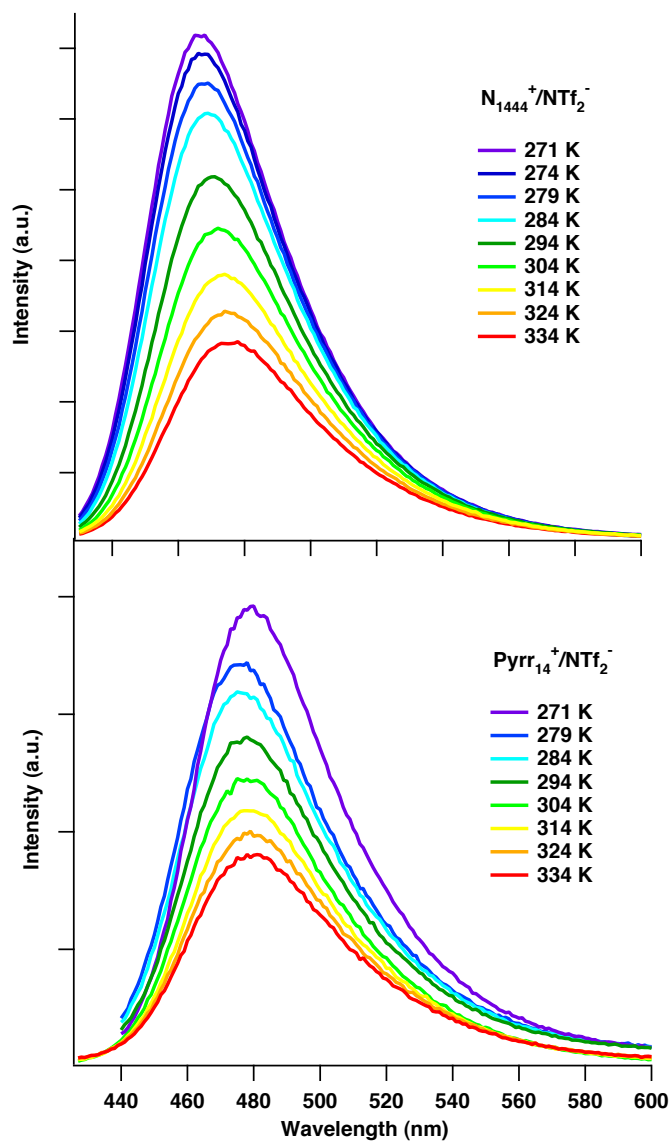


Figure 2.15: Temperature dependent steady state emission spectra of DMPD-Pro-C343 in $Pyrr_{14}^+ / NTf_2^-$ (top) and N_{1444}^+ / NTf_2^- (bottom) for Stokes shift analysis.

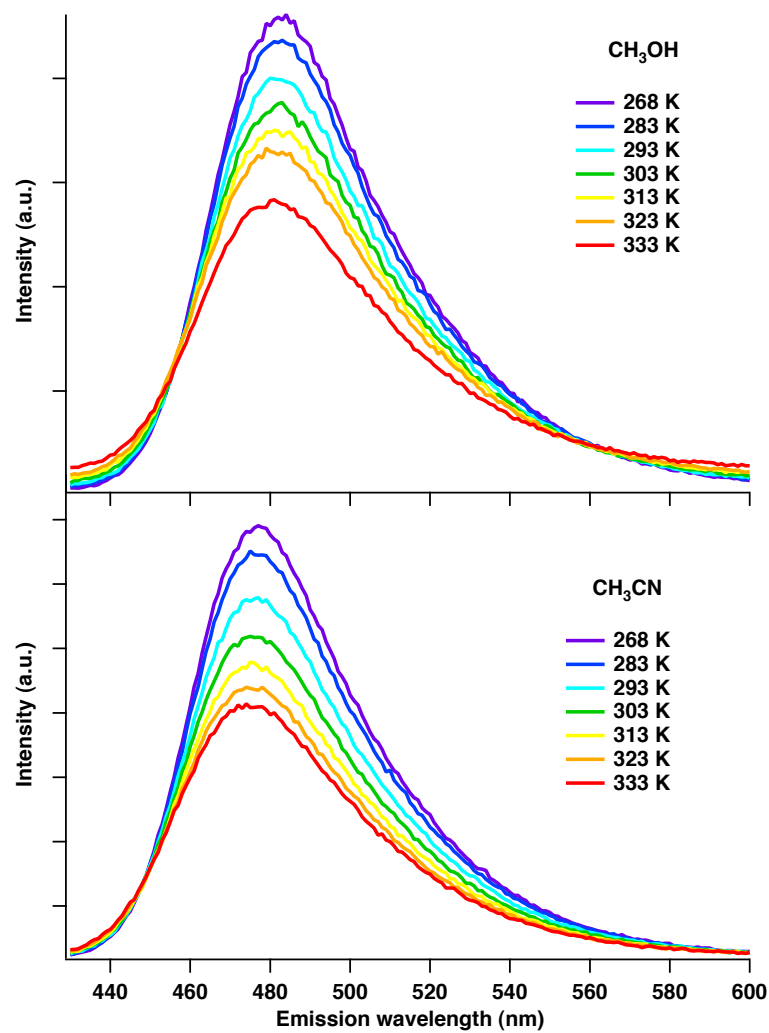


Figure 2.16: Temperature dependent steady state emission spectra of DMPD-Pro-C343 in CH_3OH (top) and CH_3CN (bottom) for Stokes shift analysis.

Excitation wavelength dependent steady-state emission spectra for DMPD-Pro-C343 in the two ionic liquids are shown in Figure 2.17 for $\text{Pyrr}_{14}^+/\text{NTf}_2^-$ and 2.18 for $\text{N}_{1444}^+/\text{NTf}_2^-$. The energy difference is calculated by subtracting the emission maximum when excited at lowest wavelength from the emission maximum excited at highest wavelength. The DMPD-Pro-C343 molecules in both ionic liquids, $\text{Pyrr}_{14}^+/\text{NTf}_2^-$ and $\text{N}_{1444}^+/\text{NTf}_2^-$, exhibit red shift in emission $\lambda_{em,max}$ when compared to the emission spectra taken with the lowest excitation wavelength (370 nm) and the highest excitation wavelength (460 nm). The differences in $\lambda_{em,max}$ in $\text{Pyrr}_{14}^+/\text{NTf}_2^-$ are 486.6 cm^{-1} , 350.2 cm^{-1} , and 216.6 cm^{-1} for emission spectra taken at 270 K, 296 K, and 334 K, respectively. In $\text{N}_{1444}^+/\text{NTf}_2^-$, the shift in emission $\lambda_{em,max}$ is 718.4 cm^{-1} , 401.5 cm^{-1} , and 220.2 cm^{-1} in $\text{N}_{1444}^+/\text{NTf}_2^-$ for 270 K, 296 K, and 334 K. The REE of DMPD-Pro-C343 is more dramatic than the REE that has been shown by common chromophores in other viscous liquids^{42,76,77} as a result of electron transfer between the donor and acceptor of this D-B-A electron-transfer molecule

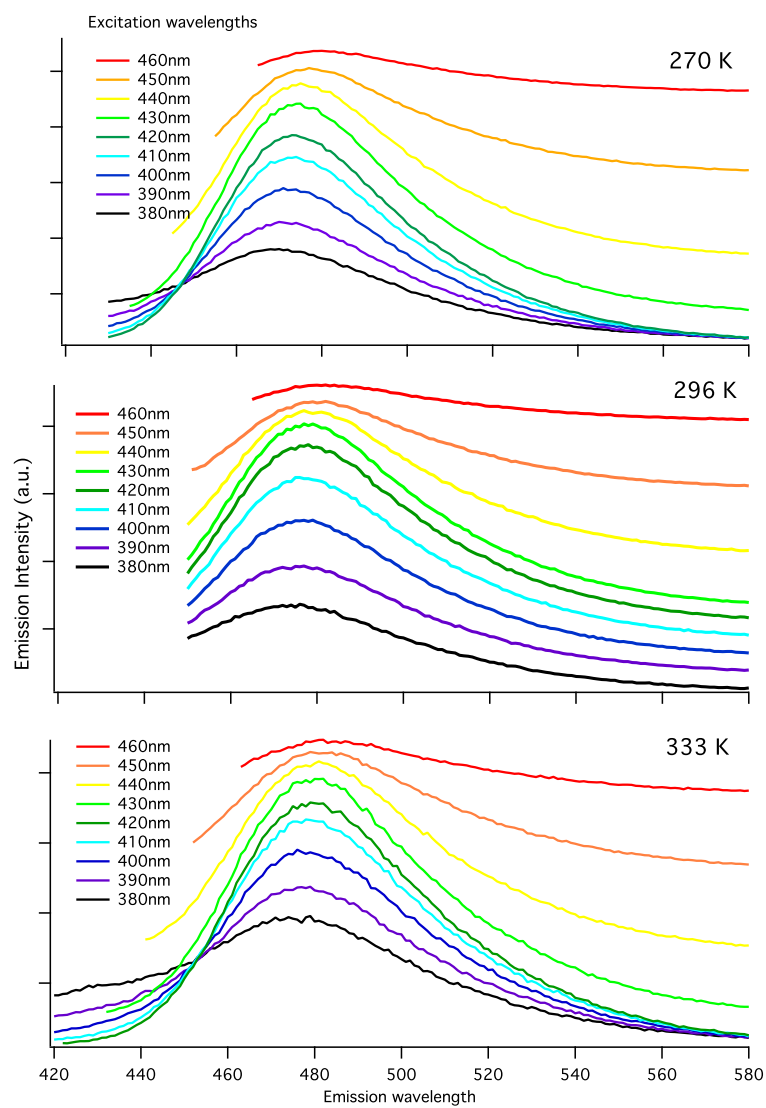


Figure 2.17: Excitation wavelength dependent steady-state emission spectra of DMPD-Pro-C343 in $\text{Pyr}_{14}^+/\text{NTf}_2^-$.

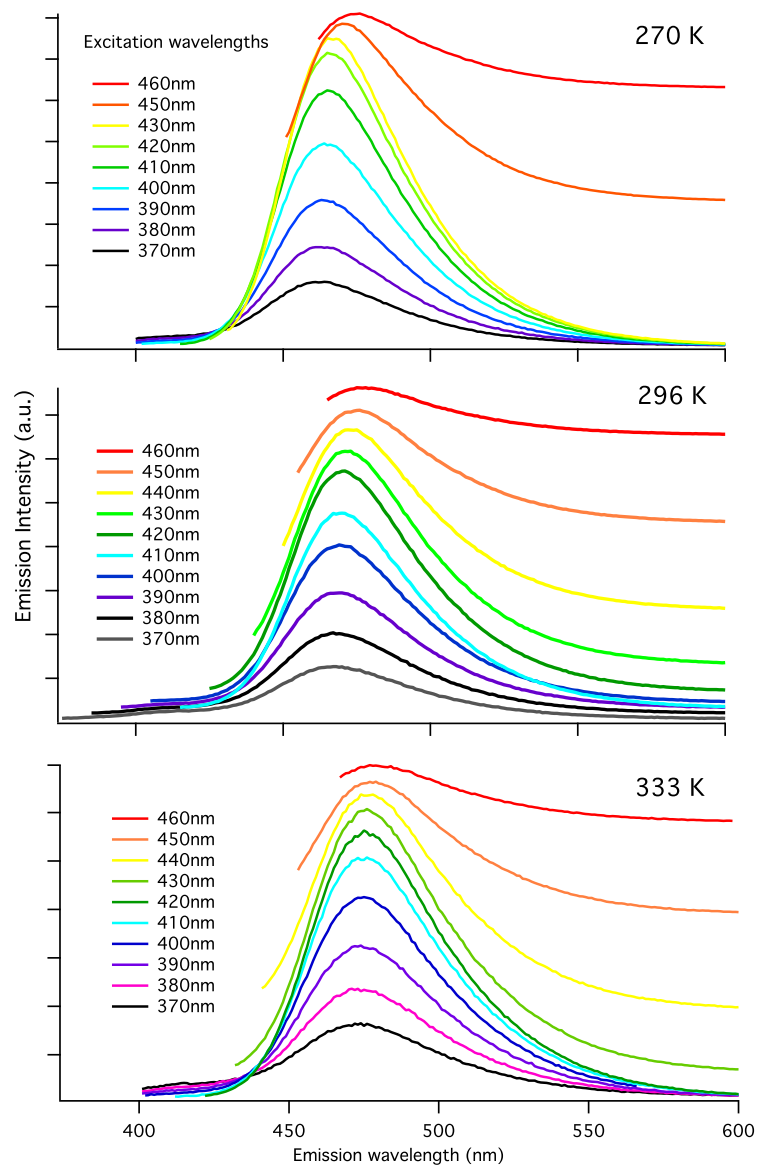


Figure 2.18: Excitation wavelength dependent steady-state emission spectra of DMPD-Pro-C343 in N_{1444}^+/NTf_2^- .

2.4.4 Time-Resolved Measurements of Electron-Transfer Kinetics in DMPD-Pro-C343

Typical TCSPC fluorescence decay transients with the residuals for the five-exponential fit for DMPD-Pro-C343 and coumarin 314 (C314, control compound) in the IL $\text{Pyrr}_{14}^+/\text{NTf}_2^-$ were shown in Figure 2.10. For comparison, the fluorescence transients that for DMPD-Pro-C343 and C314 in CH_3CN are shown in Figure 2.19. Qualitatively, the transient for C314 is single exponential and for DMPD-Pro-C343 is double exponential, even though both were fit to five exponentials for analysis. The TCSPC fluorescence decay transients for DMPD-Pro-C343 in the four solvents at 293.2 K are shown in Figure 2.20. It is apparent from the transients that the emission decays are nonexponential for the ILs, though they are dominated by a single exponential decay rate for the neutral solvents. There is a residual slower time constant observed in DMPD-Pro-C343 of about 4 ns. We believe that this slowest relaxation process results from a small fraction ($\sim 1\%$) of molecules that do not participate in electron transfer within the excited state lifetime; this lifetime is similar to that of the non-reactive model compound, coumarin 314, in each of the four solvents. The evidence for the effect of solvation on the ET kinetics of DMPD-Pro-C343 is further supported by the fact that DMPD-Pro-C343 is a system with a constrained geometry. This was confirmed by optimizing the geometry of DMPD-Pro-C343 from two different initial geometries in which the pyrrolidine ring is either up or down, by using the optimization methods mentioned above. In both cases, they gave the same optimized geometry with the pyrrolidine ring puckered up. Issa *et al.*⁹ have also shown that, in DMPD-Pro-pyrene, a similar proline-bridged D-B-A system, the conformation for which the proline ring nitrogen is above the ring plane was identified as the single low energy conformation, providing only one favorable pathway for the ET process. Park *et al.*⁸¹ have also shown that, although there are two conformations for the coumarin-proline system in solution, generally one was predominant in polar solvents. This means that the observed nonexponential ET kinetics are unlikely to arise from different pathways within the DMPD-Pro-C343 molecule resulting from conformation changes. Instead,

the nonexponential ET kinetics likely results from the distributed solvation responses to the photoexcited DMPD-Pro-C343 that occur in different solvent environments. Typical effective solvation time constants are ~ 400 ps for $\text{Pyrr}_{14}^+/\text{NTf}_2^-$ and ~ 5 ns for $\text{N}_{1444}^+/\text{NTf}_2^-$ at room temperature, though these averages result from a broad distribution of solvation rates.^{37,41}

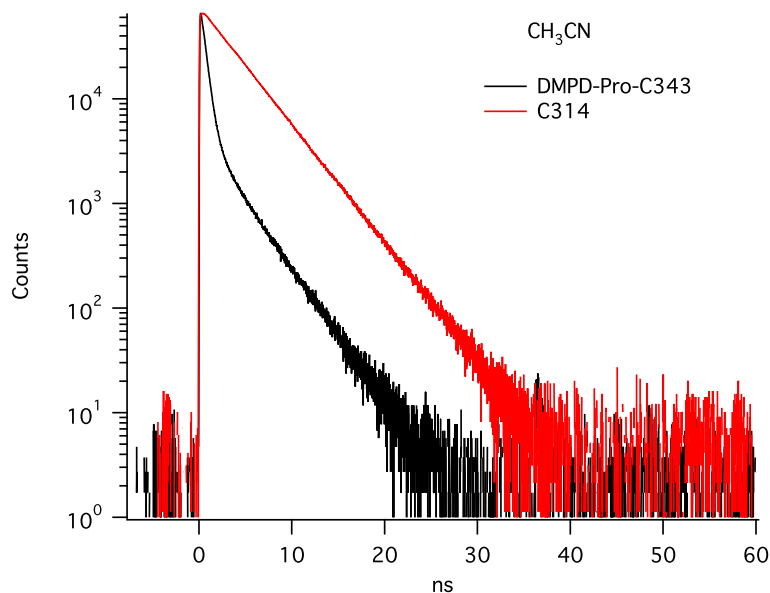


Figure 2.19: TCSPC transients for DMPD-Pro-C343 (black) and C314 (red) in CH_3CN at 293.2 K, using 430 nm laser excitation. Emission wavelengths were 480 nm for DMPD-Pro-C343 and 395 nm for C314.

2.4.5 Analysis of the DMPD-Pro-C343 Emission Transients

The kinetics underlying the temperature-dependent emission transients for DMPD-Pro-C343 are analyzed in detail using both the discrete multiexponential model, Eq. 2.8, and the distribution of exponentials model, Eq. 2.9. Both models provide excellent statistics for the fits to the DMPD-Pro-C343 emission transients.

Discrete Multiexponential Model for the Analysis of Emission Transients of DMPD-Pro-C343

The DMPD-Pro-C343 emission transients in the four solvents at 293.2 K shown in Figure 2.20 were analyzed according to Eq. 2.8, and the relative amplitudes and rate constants from multiexponential analysis are listed in Table 2.4. The observed fluorescence

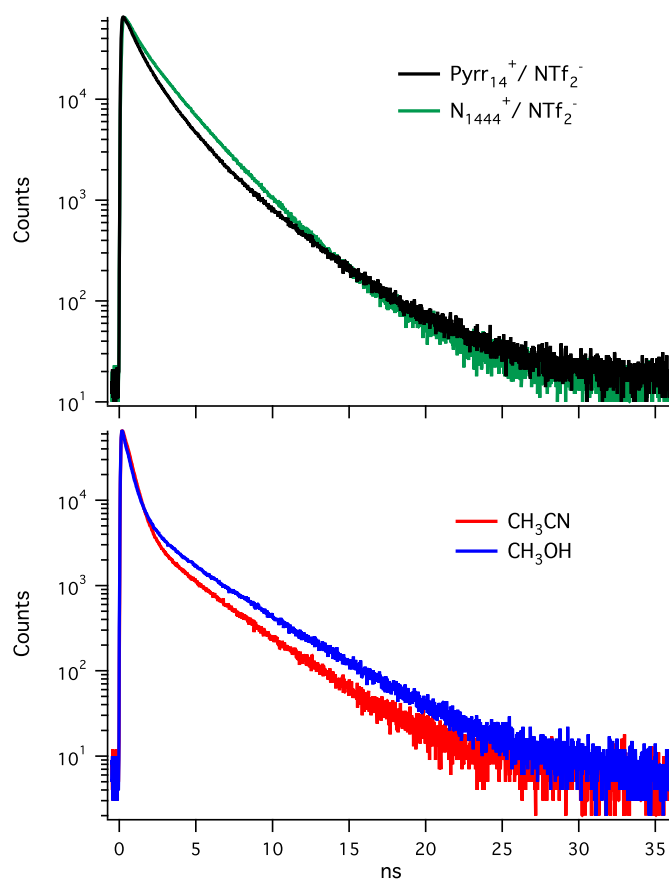


Figure 2.20: TCSPC transients for DMPD-Pro-C343 in the ionic liquids (top) and the neutral solvents (bottom) at 293.2 K, using 430 nm laser excitation. Emission wavelengths were 481 nm ($\text{Pyrr}_{14}^+ / \text{NTf}_2^-$), 490 nm ($\text{N}_{1444}^+ / \text{NTf}_2^-$), and 480 nm (CH_3CN and CH_3OH).

decay rates k_{obs} for DMPD-Pro-C343 have contributions from both electron-transfer quenching $\langle k_{ET} \rangle$ and a small population of excited states that is unlikely to undergo electron transfer $\langle k_{fl} \rangle$:

$$\langle k_{obs} \rangle = \langle k_{ET} \rangle + \langle k_{fl} \rangle \quad (2.11)$$

The average electron-transfer rate $\langle k_{ET} \rangle$ may be calculated from the weighted sum of the fastest three rates k_1 , k_2 , and k_3 (in Table 2.4). The average rate for nonreactive excited-state decay is given by $\langle k_{fl} \rangle$, the weighted sum of k_4 and k_5 , and has typical values of about $3 \times 10^8 \text{ s}^{-1}$. We assign these slowest processes to fluorescence arising from nonreactive DMPD-Pro-C343 molecules due to their similarity to the lifetimes of the nonreactive coumarin 314 model compound. We observe that the average electron-transfer rate $\langle k_{ET} \rangle$ of DMPD-Pro-C343 in the two selected ionic liquids is about half that observed for the two neutral solvents studied for comparison, CH_3CN and CH_3OH . It is clear that the ET rates are lower in the ILs. This difference results from a combination of several factors; among them, as we will discuss later, the ET processes in the ILs are farther into the Marcus inverted region. The temperature dependences of the photoinduced ET processes in DMPD-Pro-C343 were also studied in the ILs and neutral solvents. The resulting fluorescence transients are shown in Figure 2.21, and the relative amplitudes and rate constants for multiexponential fitting according to Eq. 2.8 are listed below in Tables 2.5 – 2.8. The significant temperature dependence of the fastest emission decay component is apparent, suggesting that it is indeed caused by an activated electron-transfer process. On the other hand, the slowest component of the emission decay is nearly invariant with temperature over the range studied, which is consistent with its assignment as an intrinsic excited-state decay process of the C343 dye, as observed in Figure 2.20 for CH_3CN and CH_3OH .

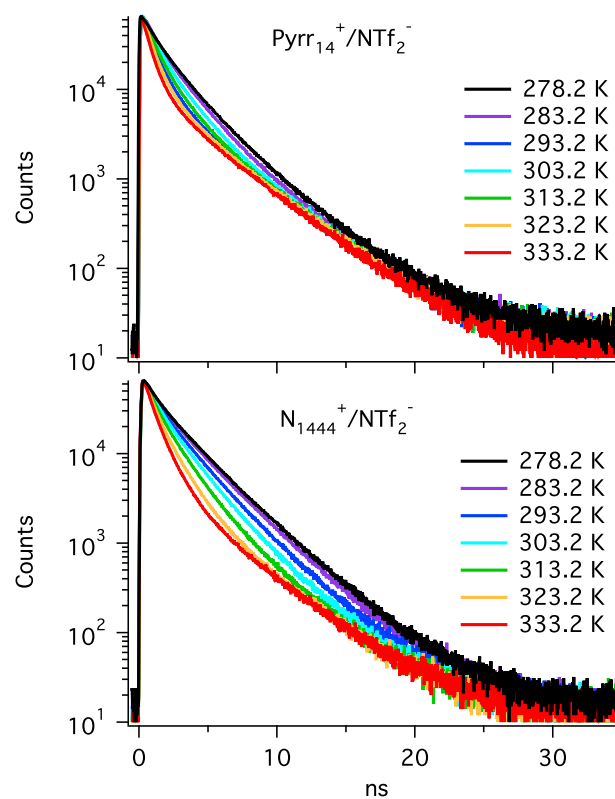


Figure 2.21: TCSPC transients of DMPD-Pro-C343 in $\text{Pyrr}_{14}^+/\text{NTf}_2^-$ (top) and $\text{N}_{1444}^+/\text{NTf}_2^-$ (bottom) from 278.2 to 333.2 K, using 430 nm laser excitation. Emission is observed at 481 nm ($\text{Pyrr}_{14}^+/\text{NTf}_2^-$) and 490 nm ($\text{mtba}/\text{NTf}_2^-$).

Table 2.4: Multi-Exponential Analysis of DMPD-Pro-C343 Emission Transients in Four Solvents at 293.2 K.^a

Solvent	A ₁	k ₁	A ₂	k ₂	A ₃	k ₃	A ₄	k ₄	A ₅	k ₅	<k _{ET} >
Pyrr ₁₄ ⁺ /NTf ₂ ⁻	0.110	5.6	0.385	1.4	0.407	0.58	0.098	0.26	0.000	0.041	1.4
N ₁₄₄₄ ⁺ /NTf ₂ ⁻	0.093	4.6	0.229	1.9	0.335	0.63	0.336	0.36	0.007	0.17	1.1
CH ₃ OH	0.093	15	0.474	3.2	0.351	1.7	0.031	0.54	0.050	0.25	3.6
CH ₃ CN	0.090	12	0.848	2.0	0.000	0.96	0.027	0.53	0.036	0.28	2.8

^a Amplitudes A_i are normalized, and rates are in units of ns⁻¹.

Table 2.5: Rates and relative amplitudes for emission transients of DMPD-Pro-C343 in CH₃OH.

T	Rel. A ₁	k ₁	Rel. A ₂	k ₂	Rel. A ₃	k ₃	Rel. A ₄	k ₄	Rel. A ₅	k ₅
278.2	0.125	11.2	0.512	2.57	0.293	1.335	0.0323	0.376	0.0376	0.240
283.2	0.163	15.7	0.556	2.60	0.218	1.283	0.0306	0.355	0.0330	0.238
293.2	0.093	15.4	0.474	3.22	0.351	1.741	0.0313	0.543	0.0502	0.252
303.2	0.095	18.1	0.525	3.53	0.307	1.807	0.0272	0.488	0.0463	0.250
313.2	0.117	12.4	0.601	3.42	0.201	1.906	0.0301	0.660	0.0515	0.258
323.2	0.104	11.3	0.600	3.90	0.224	2.028	0.0246	0.515	0.0466	0.254
333.2	0.092	10.3	0.593	4.30	0.242	2.340	0.0235	0.592	0.0494	0.260

Temperatures are reported in K, amplitudes A_i are normalized and rates are in units of ns⁻¹.

Table 2.6: Rates and relative amplitudes for emission transients of DMPD-Pro-C343 in CH₃CN.

T	Rel. A ₁	k ₁	Rel. A ₂	k ₂	Rel. A ₃	k ₃	Rel. A ₄	k ₄	Rel. A ₅	k ₅
278.2	0.1033	11.123	0.8388	2.472	0.0160	0.619	0.0417	0.296	0.0001	0.078
283.2	0.0839	10.798	0.8301	1.854	0.0408	0.821	0.0451	0.294	0.0001	0.079
293.2	0.0897	11.688	0.8482	2.041	0.0000	0.957	0.0266	0.527	0.0356	0.278
303.2	0.0860	10.908	0.8466	2.290	0.0216	0.807	0.0453	0.305	0.0006	0.132
313.2	0.1033	11.123	0.8388	2.472	0.0160	0.619	0.0417	0.296	0.0001	0.078
323.2	0.1005	10.981	0.8390	2.743	0.0135	0.882	0.0414	0.327	0.0056	0.216
333.2	0.0837	12.302	0.5935	3.285	0.2715	2.479	0.0254	0.408	0.0258	0.266

Temperatures are reported in K, amplitudes A_i are normalized and rates are in units of ns⁻¹.

Table 2.7: Rates and relative amplitudes for emission transients of DMPD–Pro–C343 in $\text{N}_{1444}^+/\text{NTf}_2^-$.

T	Rel. A_1	k_1	Rel. A_2	k_2	Rel. A_3	k_3	Rel. A_4	k_4	Rel. A_5	k_5
278.2	0.0863	5.243	0.2785	1.800	0.5551	0.526	0.0761	0.281	0.0040	0.178
283.2	0.1481	3.414	0.1706	1.528	0.3804	0.524	0.2976	0.315	0.0034	0.237
293.2	0.0933	4.593	0.2286	1.870	0.3346	0.627	0.3362	0.361	0.0073	0.169
303.2	0.0824	5.060	0.2892	1.877	0.4648	0.585	0.1592	0.331	0.0043	0.168
313.2	0.1198	4.524	0.2632	1.891	0.5028	0.657	0.0990	0.347	0.0152	0.212
323.2	0.1698	4.497	0.3106	1.596	0.4525	0.734	0.0211	0.401	0.0461	0.255
333.2	0.1865	4.376	0.3375	1.625	0.4160	0.881	0.0557	0.284	0.0042	0.188

Temperatures are reported in K, amplitudes A_i are normalized and rates are in units of ns^{-1} .

Table 2.8: Rates and relative amplitudes for emission transients of DMPD–Pro–C343 in $\text{Pyrr}_{14}^+/\text{NTf}_2^-$.

T	Rel. A_1	k_1	Rel. A_2	k_2	Rel. A_3	k_3	Rel. A_4	k_4	Rel. A_5	k_5
278.2	0.0962	7.132	0.2282	1.837	0.4786	0.592	0.1901	0.312	0.0068	0.165
283.2	0.0793	5.746	0.3311	1.447	0.4637	0.531	0.0867	0.312	0.0392	0.223
293.2	0.1102	5.556	0.3848	1.398	0.4065	0.583	0.0983	0.260	0.0001	0.041
303.2	0.1704	4.387	0.4513	1.276	0.2817	0.620	0.0966	0.260	0.0001	0.027
313.2	0.1534	5.331	0.5152	1.489	0.2285	0.700	0.1023	0.270	0.0006	0.090
323.2	0.2116	4.612	0.6072	1.413	0.0633	0.619	0.0885	0.320	0.0293	0.215
333.2	0.2353	6.545	0.5570	1.799	0.1096	0.768	0.0976	0.273	0.0006	0.085

Temperatures are reported in K, amplitudes A_i are normalized and rates are in units of ns^{-1} .

Distributed Exponential Model for the Analysis of Emission Transients of DMPD–Pro–C343

Due to the propensity of ionic liquid systems to display heterogeneous kinetic behavior, we chose to apply a model based on a distribution of exponentials in contrast to a sum of discrete ones. The fits from both distributed and discrete exponential models are displayed in Figure 2.22. In either analysis, the results confirm that the observed fluorescence kinetics of DMPD–Pro–C343 are non-exponential in each of the four solvents for all observed temperatures from 278 to 333 K. The DMPD–Pro–C343 fluorescence decays in the ionic liquids require a very broad distribution of time constants, or multiple exponential terms, to obtain adequate fits. Fits to the fluorescence transients for DMPD–Pro–C343 in CH_3CN and CH_3OH require a somewhat narrower distribution of time constants or multiple discrete exponential components. For each of the four solvents, the slowest lifetimes have small amplitudes and are assigned to the intrinsic decay of the C343 excited state. In Figure 2.22, the probabilities for the distribution

fits are plotted *vs* the value of $\log(\tau)$ as solid curves. The normalized amplitudes for the discrete exponential fits obtained using Eq. 2.8 are represented by vertical lines capped by circles. For a given solvent, the graph ordinates for the discrete time constants and the distribution probabilities are the same for all temperatures. On inspection of Figure 2.22, several qualitative differences in DMPD–Pro–C343 emission kinetics are clear. The emission decays are generally slower in the two ionic liquids $\text{Pyrr}_{14}^+/\text{NTf}_2^-$ and $\text{N}_{1444}^+/\text{NTf}_2^-$ than for CH_3OH and CH_3CN . The distribution widths of emission time constants are broader in the ionic liquids than for CH_3CN and CH_3OH . Comparing the emission kinetics in the two ionic liquids, we observe that the overall width of the distribution is greater for $\text{Pyrr}_{14}^+/\text{NTf}_2^-$, which has more rapid solvation dynamics than $\text{N}_{1444}^+/\text{NTf}_2^-$.³⁷ The emission time constants become more rapid with increasing temperature. However, careful examination of the probability of lifetime distributions in Figure 2.22 reveals that the shift occurs primarily in one major band of probability. We define the effective electron-transfer rate $k_{ET,pk}$ from the fluorescence kinetics probability distribution function as $k_{ET,pk} = 1/\tau_{peak}$, where τ_{peak} is the lifetime value for the maximum probability. The values of $k_{ET,pk}$ obtained by following the peaks of the distributions are summarized in Table 2.9. An Arrhenius analysis of DMPD–Pro–C343 in the four solvents shows that the activation energies $E_{a,ET}$ for electron transfer in the two ionic liquids are approximately twice those for the two neutral solvents (see Figure 2.23).

Table 2.9: Values for the most probable electron-transfer rates k_{ET} in ns^{-1} for each solvent at seven different temperatures, obtained from the data in Figure 2.22

T (K)	$\text{Pyrr}_{14}^+/\text{NTf}_2^-$	$\text{N}_{1444}^+/\text{NTf}_2^-$	CH_3OH	CH_3CN
278.2	0.60	0.38	2.3	1.8
283.2	0.50	0.41	2.3	1.8
293.2	a	0.45	2.3	2.0
303.2	0.95	0.55	2.8	2.2
313.2	1.4	0.66	2.8	2.4
323.2	1.4	0.87	3.4	2.7
333.2	1.7	1.2	4.1	2.9

^a The data point for $\text{Pyrr}_{14}^+/\text{NTf}_2^-$ at 293.2 K was omitted because the broad asymmetric nature of the distribution cannot be analyzed the same way as the other distributions.

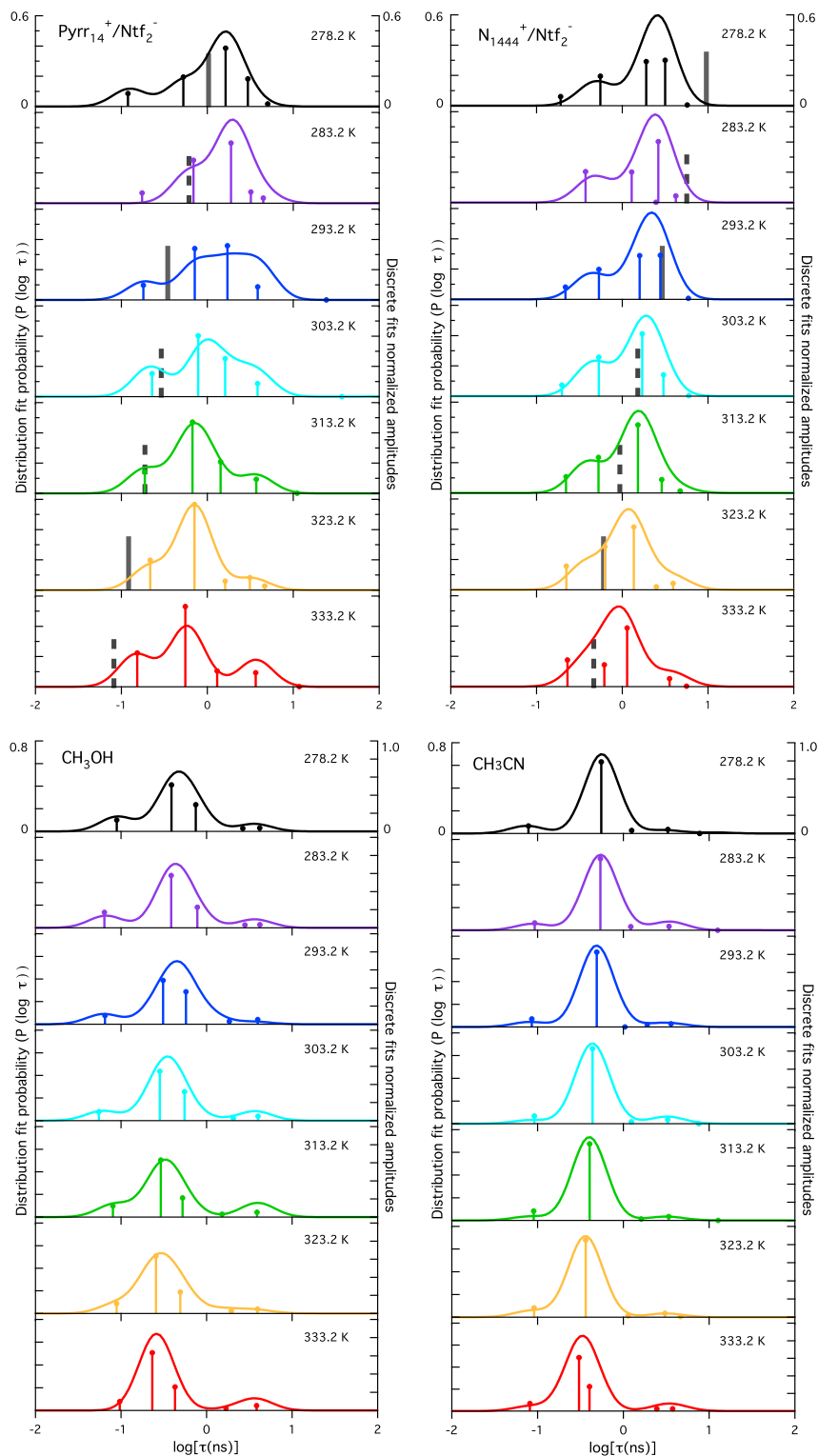


Figure 2.22: Distribution fits (solid curves) for DMPD-Pro-C343 in $\text{Pyrr}_{14}^{+}/\text{Ntf}_2^{-}$, $\text{N}_{1444}^{+}/\text{Ntf}_2^{-}$, CH_3OH , and CH_3CN from 278.2 to 333.2 K. Distribution fits are normalized to the total area for each data set with the lifetime probability represented on the left axes. Discrete fits are shown as vertical lines and circles. Axes for the normalized amplitudes of the discrete fits are labeled on the graph at the right. Note that the amplitudes of the distributions and discrete fit amplitudes are larger for CH_3OH and CH_3CN , and the distributions are more sharply defined. In the top two graphs, the solid gray bars represent average solvation times $\langle \tau_{\text{solv}} \rangle$ from the measurements on C153 in the same ILs by Funston *et al.*,³⁷ and the dotted bars represent extrapolated $\langle \tau_{\text{solv}} \rangle$ values for temperatures not measured in ref Funston.

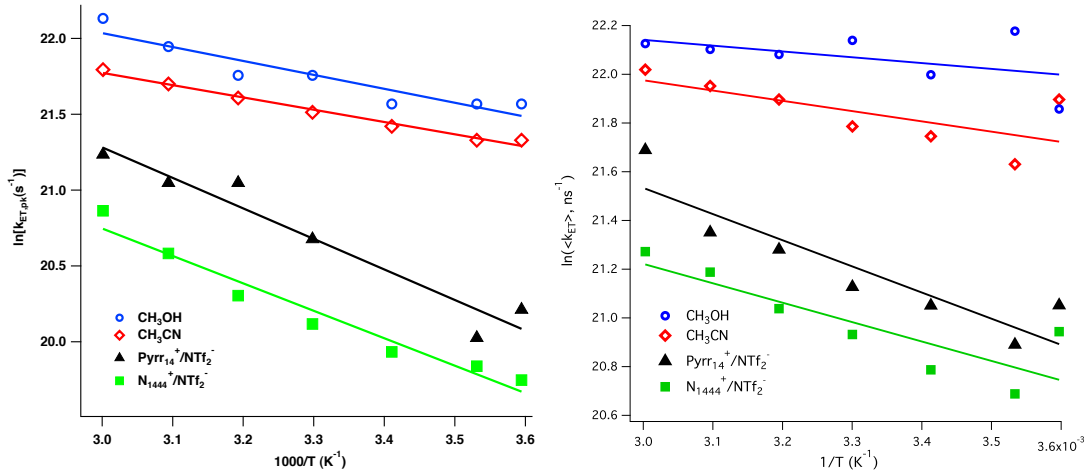


Figure 2.23: Arrhenius plots of DMPD-Pro-C343 electron-transfer rates in four solvents from 278.2 K to 333.2 K. The plot on the left is using $k_{ET,pk}$ values from the distribution fit and the plot on the right is using $\langle k_{ET} \rangle$ obtained from Eq.2.11. In the graph on the left, the data point for $\text{Pyr}_{14}^+/\text{NTf}_2^-$ at 293.2 K was not included when calculating the best-fit line because the distribution peak is not well defined for this data set.

The analysis using $k_{ET,pk}$ values from the distributed lifetime kinetics provides activation energies of 0.173 eV ($\text{Pyr}_{14}^+/\text{NTf}_2^-$), 0.156 eV ($\text{N}_{1444}^+/\text{NTf}_2^-$), 0.070 eV (CH_3CN), and 0.079 eV (CH_3OH). The activation energies for electron transfer of DMPD-Pro-C343 in the two ionic liquids are approximately twice those for the two neutral solvents. Using $\langle k_{ET} \rangle$ derived from the multiexponential fits (Figure 2.23, right), Arrhenius $E_{a,ET}$ values are lower: 0.092 eV ($\text{Pyr}_{14}^+/\text{NTf}_2^-$), 0.069 eV ($\text{N}_{1444}^+/\text{NTf}_2^-$), 0.036 eV (CH_3CN), and 0.020 eV (CH_3OH). Although the activation energies calculated using $\langle k_{ET} \rangle$ are smaller in every case, the scaling between the activation energies for the ILs and normal solvents follows the same trend. For all four solvents, the reaction barrier is substantially smaller than the activation energies for viscous flow, $E_{1/\eta}$, which indicates that it is unlikely for diffusive processes to play any role in electron-transfer gating for our D-B-A system. The electron-transfer kinetics in the ionic liquids $\text{Pyr}_{14}^+/\text{NTf}_2^-$ and $\text{N}_{1444}^+/\text{NTf}_2^-$ are broadly distributed. The distribution for $\text{Pyr}_{14}^+/\text{NTf}_2^-$ shows appreciable amplitude for the faster part of the distribution from about 120–160 ps, while the slower, dominant part of the distribution shifts from about 1.6 to 0.65 ns with increasing temperature. The electron-transfer kinetics distribution in $\text{N}_{1444}^+/\text{NTf}_2^-$ does not show any of the ~ 100 ps feature present

for CH_3OH CH_3CN , or $\text{Pyrr}_{14}^+/\text{NTf}_2^-$. For this IL, the part of the distribution assigned to electron transfer is bimodal, with the faster part of the distribution shifting from about 600 ps at 278.2 K to about 200 ps at 333.2 K; the peak of the slower part of the distribution shifts from about 2.5 ns at 278.2 K to about 1 ns at 333.2 K. The distribution of the ET kinetics of DMPD-Pro-C343 in the neutral solvents is the narrowest for CH_3CN . The distribution is centered at 600 ps for 278.2 K and decreases with increasing temperature to a value of about 300 ps at 333.2 K. A small fraction of the observed kinetics in CH_3CN is fit to shorter lifetimes distributed around 100 ps. The portion of the excited state kinetics of DMPD-Pro-C343 in CH_3OH assigned to electron transfer is slightly more complex. At 333.2 K, the kinetics distribution is similar to that for CH_3CN , while at lower temperatures the fraction of the distribution resulting from kinetics in the 50–100 ps range is larger than that for CH_3CN . The center of the DMPD-Pro-C343 kinetics distribution assigned to electron transfer in CH_3OH shifts from about 600 ps at 278.2 K to about 250 ps at 333.2 K. In both CH_3CN and CH_3OH , there is a small part of the kinetic distribution corresponding to the intrinsic excited-state decay of C343, as was noted above for the discrete exponential fitting. It is useful to compare the electron-transfer distributions with the time scales for solvation dynamics in the ionic liquids. Funston *et al.*³⁷ characterized the average times $\langle\tau_{\text{solv}}\rangle$ for solvent relaxation in $\text{N}_{1444}^+/\text{NTf}_2^-$ and $\text{Pyrr}_{14}^+/\text{NTf}_2^-$ over a range of temperatures using the solvatochromic fluorescence probe coumarin 153. The $\langle\tau_{\text{solv}}\rangle$ values at each temperature in both ILs are depicted in Figure 2.22 as vertical gray bars. It is important to keep in mind that the $\langle\tau_{\text{solv}}\rangle$ values emphasize the slowest part of the solvation dynamics. For $\text{Pyrr}_{14}^+/\text{NTf}_2^-$ at lower temperatures, $\langle\tau_{\text{solv}}\rangle$ lies in the middle of the distribution of electron-transfer rates. Notably, at lower temperatures, the average solvation dynamics in $\text{N}_{1444}^+/\text{NTf}_2^-$ are slower than even the small-amplitude components of the fluorescence transients that we assign to the excited-state lifetimes. For higher temperatures, $\langle\tau_{\text{solv}}\rangle$ for $\text{N}_{1444}^+/\text{NTf}_2^-$ approaches the time scales of the fastest electron-transfer kinetics. For $\text{N}_{1444}^+/\text{NTf}_2^-$, $\langle\tau_{\text{solv}}\rangle$ is slower than for $\text{Pyrr}_{14}^+/\text{NTf}_2^-$ by an order of magnitude. The solvation time scales for $\text{N}_{1444}^+/\text{NTf}_2^-$ span a greater range of the electron-transfer kinetics

distribution than for $\text{Pyrr}_{14}^+/\text{NTf}_2^-$. The dependence of the electron-transfer rate constants on solvent viscosities was considered by plotting a log-log graph of $k_{ET,pk}$ vs viscosity (Figure 2.24). The slopes of the power-law fits for the three liquids are -0.51 ± 0.07 ($\text{Pyrr}_{14}^+/\text{NTf}_2^-$), -0.86 ± 0.03 (CH_3CN), and -0.68 ± 0.10 (CH_3OH). The data for $\text{N}_{1444}^+/\text{NTf}_2^-$ show distinct curvature and thus do not fit well to a single power law, so two power-law fits were used: one for temperatures 303–333 K having a slope of -0.44 ± 0.06 and the second for the three data points between 278 and 293 K with a slope of -0.12 ± 0.01 . The behavior of $\text{N}_{1444}^+/\text{NTf}_2^-$ in the higher temperature range is similar to that for $\text{Pyrr}_{14}^+/\text{NTf}_2^-$, while at lower temperatures the ET rate constants show a weaker dependence on viscosity. The transition between these two regimes coincides with the crossover of the average solvation times $\langle\tau_{solv}\rangle$ and the peak electron-transfer time constants ($1/k_{ET,pk}$), as indicated in Figure 2.22. It appears that, within the range 278–293 K, a significant component of the electron-transfer process occurs to DMPD–Pro–C343 excited states that are not fully solvated and therefore could have different electron-transfer parameters. However, since both the solvation dynamics and electron-transfer rates calculated from fluorescence quenching data are both strongly heterogeneous, presently we do not have sufficient information to prove this is the case.

It was our aim in this study to select one ionic liquid, $\text{Pyrr}_{14}^+/\text{NTf}_2^-$, with solvation dynamics fast enough relative to electron transfer that it could be considered as a more classical conventional solvent, and another ionic liquid, $\text{N}_{1444}^+/\text{NTf}_2^-$, whose dynamical time scales overlap with electron transfer. While the latter goal was largely met, the ET and solvation time scales in $\text{Pyrr}_{14}^+/\text{NTf}_2^-$ still overlap to a certain extent, particularly at lower temperatures. Nevertheless, the differences between the observed kinetics in the two ionic liquids show the consequences of their dynamical differences. It is also important to remember that the solvation dynamics of the ionic liquids are distributed and are only crudely represented by the vertical bars, indicating $\langle\tau_{solv}\rangle$ in Figure 2.22, as well as the fact that some solvation components in ILs occur on picosecond and shorter time scales.⁴⁶ Thus, it is not yet possible to conclusively assign the observed electron-transfer behavior in the ionic liquids to either heterogeneities in

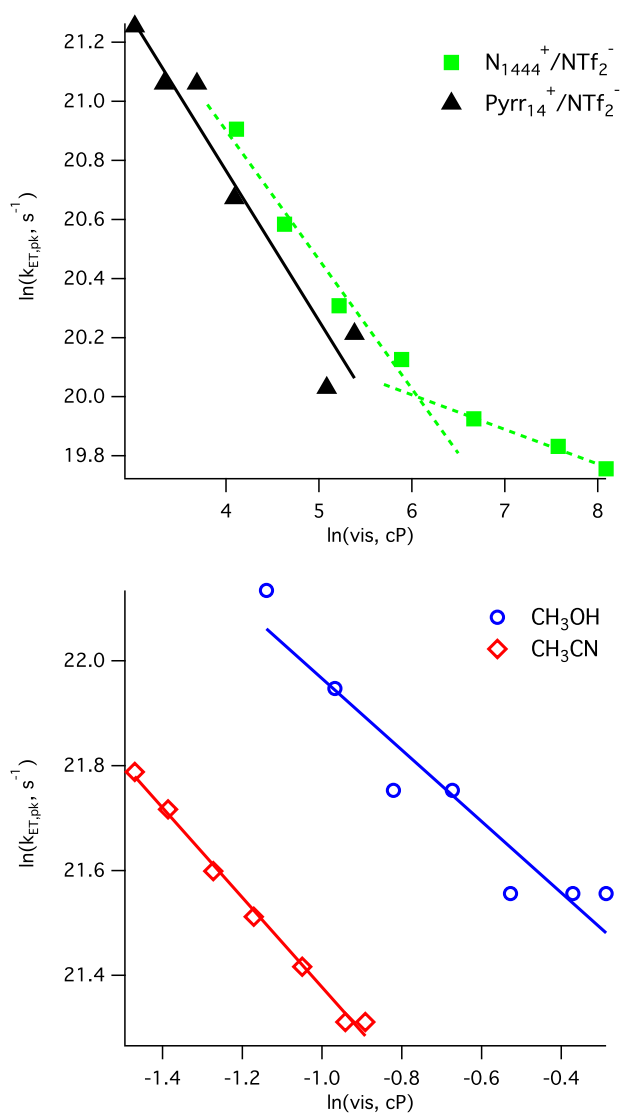


Figure 2.24: Plot of $\ln(k_{ET,pk})$ for electron transfer in DMPD-Pro-C343 *vs* $\ln(\text{viscosity, cP})$ in the ionic liquids (top) and the neutral solvents (bottom). Two (dotted) fit lines for $N_{1444}^{+}NTf_2^{-}$ are shown to indicate that a double power-law model may be more appropriate in that case.

static or dynamic solvation or to specific conformations of the molecule. This system would potentially be an interesting subject for a two-dimensional spectroscopy study of the kind reported by Sahu *et al.*⁸²

2.4.6 Analysis of the Observed Electron-Transfer Rates Using Marcus Theory

For the sake of simplicity in the analysis of our results by Marcus theory, we shall follow the behavior of the major peak of the kinetic distribution, keeping in mind that it effectively represents a distribution of rates and activation energies, and that there could be other, smaller components of the distribution that have their own characteristics.

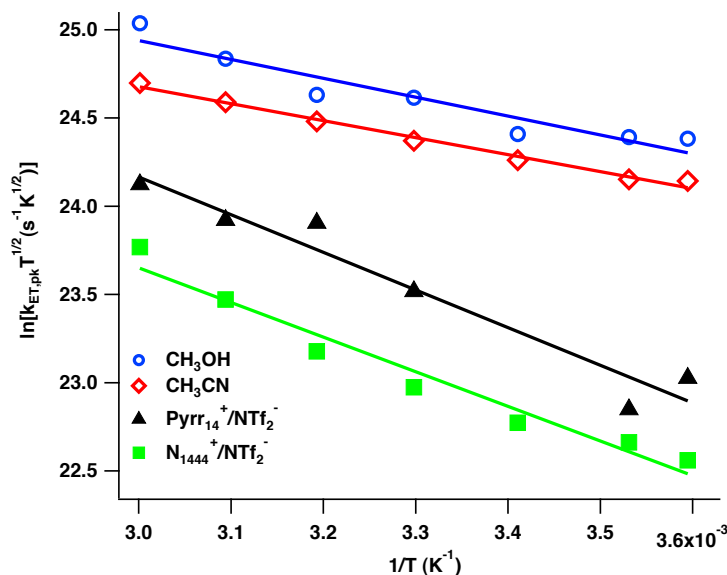


Figure 2.25: Plot of $\ln(k_{ET,pk} T^{1/2})$ vs $(1/T)$ for intramolecular electron transfer of DMPD-Pro-C343 in the four solvents. The data point for Pyrr₁₄⁺/NTf₂⁻ at 293.2 K was not included when calculating the best-fit line because the distribution peak is not well-defined for this data set.

The Marcus plots of $\ln(k_{ET,pk} T^{1/2})$ vs $(1/T)$ for DMPD-Pro-C343 in Figure 2.25 are obtained from the values of $k_{ET,pk}$ derived from the probability distributions in Figure 2.22 for each of the four solvents. (For this purpose, the entire temperature range was used for N₁₄₄₄⁺/NTf₂⁻. The data point for Pyrr₁₄⁺/NTf₂⁻ at 293 K is not plotted because the distribution peak is not well-defined for that temperature, see Figure 2.22) The data fit reasonably well to straight lines, from which values of ΔG^* can be calculated from the slopes and listed in Table 2. Generally, the ΔG^* values for the

ionic liquids are about twice the ΔG^* values for the neutral solvents. As was the case with the Arrhenius plots, the Marcus analysis using $\langle k_{ET} \rangle$ values from the multiexponential analysis gives smaller free energy barriers of 0.106 eV ($\text{Pyrr}_{14}^+/\text{NTf}_2^-$), 0.082 eV ($\text{N}_{1444}^+/\text{NTf}_2^-$), 0.049 eV (CH_3CN), and 0.034 eV (CH_3OH). Again, the scaling between the activation energies for the ILs and normal solvents follows the same trend.

We have reported the Arrhenius and Marcus results for the $\langle k_{ET} \rangle$ values obtained from the discrete multiexponential fitting because most readers are familiar with that method of fitting kinetics and comparable $\langle k_{ET} \rangle$ values would be obtained from the related stretched exponential model fitting. However, in the context of the distributed kinetics observed here, we consider that the discrete multiexponential fitting method does not represent the electron-transfer kinetics of the system as well as the distribution models, and we have higher confidence in the activation parameters obtained from $k_{ET,pk}$, as these represent the dominant feature in the rate distribution.

Using the ΔG^* values obtained above from $k_{ET,pk}$ and the relationship between ΔG^0 and λ given by Eq. 2.4, the estimates for the total reorganization energy λ given in Table 2.2 range from 1.02 to 1.14 eV. We note that the electron transfer in DMPD-Pro-C343 is in the inverted regime for all four solvents, since $-\Delta G^0 \gg \lambda$. The reorganization energy is typically considered as the sum of two terms: $\lambda = \lambda_i + \lambda_o$, where λ_i is the reorganization energy of the inner sphere, the D-B-A molecule, and λ_o is the outer sphere or the solvent reorganization energy. The λ_i for other qualitatively similar organic intramolecular D-B-A systems such as the Paddon-Row compounds (1,4-dimethox-naphthalene-bridge-1,1-dicyanoethylene) or the dimethoxynaphthalene-bridge-dicyanovinyl compounds studied by others^{18,83-85} are in the range from 0.35 to 0.55 eV. In Table 2.2, we provide λ_o values that are estimated from the steady-state Stokes shifts of DMPD-Pro-C343 in the four solvents.

We have estimated the Zusman adiabaticity parameter g in the two ILs in two extreme cases: the smallest value is for $\text{Pyrr}_{14}^+/\text{NTf}_2^-$ at 353 K, and the largest value is for $\text{N}_{1444}^+/\text{NTf}_2^-$ at 278 K, which correspond to the lowest and highest viscosities observed for the ILs in the range of experimental temperatures. For $\text{Pyrr}_{14}^+/\text{NTf}_2^-$ at 353 K, where the average solvation time constant, $\langle \tau_{solv} \rangle = 53.5$ ps,³⁷ $\lambda = 1.03$ eV, and

the smallest of the H_{DA} values calculated using GMH is 120 cm^{-1} , we obtain $g = 220$. For $\text{N}_{1444}^{+}/\text{NTf}_2^{-}$ at 278 K, $\langle \tau_{solv} \rangle = 9.8 \text{ ns}$,³⁷ $\lambda = 1.03 \text{ eV}$, and for a maximal value of $H_{DA} = 231 \text{ cm}^{-1}$ we obtain $g = 1.5 \times 10^5$. In both cases, $g \gg 1$, which shows that our system is in the adiabatic regime and therefore needs to be treated by the solvent-controlled ET model in the ILs. The adiabatic threshold value of H_{DA} obtained when $g = 1$ is calculated for these two cases, giving 8 cm^{-1} for $\text{Pyrr}_{14}^{+}/\text{NTf}_2^{-}$ at 353 K and 0.6 cm^{-1} for $\text{N}_{1444}^{+}/\text{NTf}_2^{-}$ at 278 K. These values imply that the adiabaticity threshold for the two ionic liquids is dramatically lower than the threshold for the neutral solvents;²³ thus, electron-transfer reactions in typical ILs may normally be expected to be in the solvent-controlled regime neglecting any diffusion effects.²⁶

2.5 Conclusions

The DMPD-Pro-C343 donor-bridge-acceptor complex is a useful tool for illustrating the differences in electron-transfer kinetics between ionic liquids and conventional solvents. The excited-state emission transients in the two ionic liquids studied are highly nonexponential and require a broad distribution of exponential decay rates to properly fit the decay kinetics. Analysis of the temperature dependence of the electron-transfer kinetics provides estimates of the activation for electron-transfer barriers, which are about double for the ionic liquids relative to the two neutral solvents. We have noted that electron-transfer reactions in ILs can be expected to be in the solvent-limited or adiabatic regime. The solvent relaxation observed for CH_3CN and over this range of temperatures should be complete within a time scale that is at least two orders of magnitude faster than the fastest part of the distribution of electron-transfer kinetics,⁴⁵ i.e., for CH_3CN and CH_3OH , solvent reorganization about the excited state is complete long before the electron-transfer reactions take place. This is not the case for the ionic liquids $\text{Pyrr}_{14}^{+}/\text{NTf}_2^{-}$ and $\text{N}_{1444}^{+}/\text{NTf}_2^{-}$, where the excited-state solvation dynamics^{37,41} overlap with the time scales for electron transfer. This entanglement of solvation and reaction dynamics for the ionic liquids is a general feature of many reactions in these media and is the most likely explanation for the broader and highly nonexponential distributions observed in the fluorescence kinetics. Such kinetics will

rarely be described adequately by simple rate schemes and will require more complex models such as the distribution of exponentials employed here. This work is a first attempt at applying this type of treatment to a kinetic process in ionic liquids, although it has been used extensively in other scientific communities, particularly biophysical dynamics.

Bibliography

- [1] R. A. Marcus. Chemical and electrochemical electron-transfer theory. *Annu. Rev. Phys. Chem.*, 15:155, 1964.
- [2] R. A. Marcus. Electron Transfer Reactions in Chemistry. Theory and Experiment. *Rev. Mod. Phys.*, 65(3):599–610, 1993.
- [3] R. A. Marcus and N. Sutin. Electron Transfers in Chemistry and Biology. *Biochim. Biophys.*, 811(3):265–322, 1985.
- [4] S. S. Isied. Long-range electron-transfer in peptides and proteins. *Progr. Inorg. Chem.*, 32:443–557, 1984.
- [5] J. R. Closs, G. L.; Miller. Intramolecular long-distance electron-transfer in organic-molecules. *Science*, 240:440–447, 1988.
- [6] M. Maroncelli, J. MacInnis, and G. R. Fleming. Polar solvent dynamics and electron-transfer reactions. *Science*, 243:1674–1681, 1989.
- [7] S. S. Skourtis, D. H. Waldeck, and D. N. Beratan. Fluctuations in biological and bioinspired electron-transfer reactions. *Ann. Rev. Phys. Chem.*, 61:461–485, 2010.
- [8] S. S. Isied, M. Y. Ogawa, and J. F. Wishart. Peptide-Mediated Intramolecular Electron Transfer: Long-Range Distance Dependence. *Chem. Rev.*, 92:381–394, 1992.
- [9] J. B. Issa, A. S. Salameh, Jr. E. W. Castner, J. F. Wishart, and S. S. Isied. Conformational analysis of the electron-transfer kinetics across oligoproline peptides using N,N-Dimethyl-1,4-benzenediamine donors and pyrene-1-sulfonyl acceptors. *J. Phys Chem. B*, 111:6878–6886, 2007.

- [10] R. A. Malak, Z. Gao, J. F. Wishart, and S. S. Isied. Long-range electron transfer across peptide bridges: The transition from electron superexchange to hopping. *J. Am. Chem. Soc.*, 126:1388, 2004.
- [11] H. B. Gray and J. R. Winkler. Electron transfer in proteins. *Annu. Rev. Biochem.*, 65:537, 1996.
- [12] K. Bobrowski and R. Lubis. Intermolecular charge-transfer involving tryptophan, tyrosine and 3 electron-bonded intermediates derived from methionine. *Int. J. Rad. Bio.*, 50:1039–1050, 1986.
- [13] M. N. Paddon-Row. Investigating long-range electron-transfer processes with rigid, covalently linked donor-(norbornylogous bridge)-acceptor systems. *Acc. Chem. Res.*, 27:18, 1994.
- [14] K. S. Schanze and K. Sauer. Photoinduced intramolecular electron-transfer in peptide-bridged molecules. *J. Am. Chem. Soc.*, 110:1180, 1988.
- [15] R. A. Marcus. On the theory of oxidation-reduction reactions involving electron transfer i. *J. Chem. Phys.*, 24:966, 1956.
- [16] J. Jortner. Temperature dependent activation energy for electron transfer between biological molecules. *J. Chem. Phys.*, 64:4860, 1976.
- [17] J. Jortner and M. Bixon. Intramolecular vibrational excitations accompanying solvent-controlled electron transfer reactions. *J. Chem. Phys.*, 88:167–170, 1988.
- [18] D. H. Zimmt, M. B.; Waldeck. Exposing Solvent’s Roles in Electron Transfer Reactions: Tunneling Pathway and Solvation. *J. Phys. Chem. A*, 107(19):3580–3597, 2003.
- [19] P. F. Barbara, T. J. Meyer, and M. A. Ratner. Contemporary issues in electron transfer research. *J. Phys. Chem.*, 100:13148–13168, 1996.
- [20] N. Sutin and C. Creutz. Electron-Transfer Reactions of Excited States. *J. Chem. Edu.*, 60:809–814, 1983.

- [21] J. E. Subotnik. Communication: Configuration interaction singles has a large systematic bias against charge-transfer states. *J. Chem. Phys.*, 135:071104, 2011.
- [22] R. Cave and M. D. Newton. Calculation of electronic coupling matrix elements for ground and excited state electron transfer reactions: Comparison of the generalized mulliken–hush and block diagonalization methods. *J. Chem. Phys.*, 106(22):9213–9226, 1997.
- [23] E. W. Castner, Jr., D. Kennedy, and R. J. Cave. Solvent as electron donor: Donor/acceptor electronic coupling is a dynamical variable. *J. Phys. Chem. A*, 104:2869–2885, 2000.
- [24] J. B. Issa, K. Korogh-Jespersen, and S. S. Isied. Conformational dependence of electronic coupling across peptide bonds: A ramachandran map. *J. Phys. Chem. C*, 114:20809–20812, 2010.
- [25] R. J. Cave and M. D. Newton. Generalization of the mulliken-hush treatment for the calculation of electron transfer matrix elements. *Chem. Phys. Lett.*, 249:15–19, 1996.
- [26] L. D. Zusman. Outer-sphere electron transfer in polar solvents. *Chem. Phys.*, 49:295–304, 1980.
- [27] D. R. MacFarlane, P. Meakin, J. Sun, N. Amini, and M. Forsyth. Pyrrolidinium imides: A new family of molten salts and conductive plastic crystal phases. *Journal of Physical Chemistry B*, 103:4164–4170, 1999.
- [28] H. Weingärtner, P. Sasisanker, C. Daguenet, P. J. Dyson, I. Krossing, J. M. Slatery, and T. Schubert. The dielectric response of room-temperature ionic liquids: Effect of cation variation?. *J. Phys. Chem. B*, 111:4775–4780, 2007.
- [29] K. A. Fletcher, I. A. Storey, A. E. Hendricks, S. Pandey, and S. Pandey. Behavior of the solvatochromic probes Reichardt’s dye, pyrene, dansylamide, Nile Red and 1-pyrenecarbaldehyde within the room-temperature ionic liquid bmimPF₆. *Green Chem.*, 3:210–215, 2001.

- [30] S. N. V. K. Aki, J. F. Brennecke, and A. Samanta. How polar are room-temperature ionic liquids? *Chem. Commun.*, 5:413–414, 2001.
- [31] P. K. Mandal and A. Samanta. Fluorescence studies in a pyrrolidinium ionic liquid: Polarity of the medium and solvation dynamics. *J. Phys. Chem. B*, 109:15172–15177, 2005.
- [32] R. Karmakar and A. Samanta. Solvation dynamics of coumarin-153 in a room-temperature ionic liquid. *J. Phys. Chem. A*, 106:4447–4452, 2002.
- [33] P. K. Chowdhury, M. Halder, L. Sanders, T. Calhoun, J. L. Anderson, D. W. Armstrong, X. Song, and J. W. Petrich. Dynamic solvation in room-temperature ionic liquids. *J. Phys. Chem. B*, 108:10245–10255, 2004.
- [34] H. Jin, G. A. Baker, S. Arzhantsev, J. Dong, and M. Maroncelli. Solvation and rotational dynamics of coumarin 153 in ionic liquids: Comparisons to conventional solvents. *J. Phys. Chem. B*, 117:7291–7302, 2007.
- [35] A. Paul and A. Samanta. Photoinduced Electron Transfer Reaction in Room Temperature Ionic Liquids: A Combined Laser Flash Photolysis and Fluorescence Study. *J. Phys. Chem. B*, 111:1957–1962, 2007.
- [36] S. Sarkar, R. Pramanik, D. Seth, P. Setua, and N. Sarkar. Photoinduced electron transfer (PET) from n,n-dimethylaniline to 7-amino coumarin dyes in a room temperature ionic liquid (RTIL): Slowing down of electron transfer rate compared to conventional solvents. *Chem. Phys. Lett.*, 477:102–108, 2009.
- [37] A. M. Funston, T. A. Fadeeva, J. F. Wishart, and E. W. Castner, Jr. Fluorescence probing of temperature-dependent dynamics and friction in ionic liquid local environments. *J. Phys. Chem. B*, 111:4963–4977, 2007.
- [38] E. W. Castner, Jr., J. F. Wishart, and H. Shirota. Intermolecular dynamics, interactions, and solvation in ionic liquids. *Acc. Chem. Res.*, 40:1217–1227, 2007.
- [39] N. Ito, S. Arzhantsev, and M. Maroncelli. The probe dependence of solvation

- dynamics and rotation in the ionic liquid 1-butyl-3-methyl-imidazolium hexafluorophosphate. *Chem. Phys. Lett.*, 396:83–91, 2004.
- [40] J. A. Ingram, R. S. Moog, N. Ito, R. Biswas, and M. Maroncelli. Solute rotation and solvation dynamics in a room-temperature ionic liquid. *J. Phys. Chem. B*, 107:5926–5932, 2003.
- [41] H. Jin, X. Li, and M. Maroncelli. Heterogeneous solute dynamics in room-temperature ionic liquids. *J. Phys. Chem. B*, 111:13473–13478, 2007.
- [42] P. K. Mandal, N. Sarkar, and A. Samanta. Excitation-wavelength-dependent fluorescence behavior of some dipolar molecules in room-temperature ionic liquids. *J. Phys. Chem. A*, 108:9048–9053, 2004.
- [43] C. Reichardt. Solvatochromic Dyes as Solvent Polarity Indicators. *Chem. Rev.*, 94:2319–2358, 1994.
- [44] C. Reichardt. Pyridinium n-phenoxide betaine dyes and their application to the determination of solvent polarities part 29 - polarity of ionic liquids determined empirically by means of solvatochromic pyridinium n-phenolate betaine dyes. *Green Chem.*, 7:339–351, 2005.
- [45] M. L. Horng, J. A. Gardecki, A. Papazyan, and M. Maroncelli. Subpicosecond Measurements of Polar Solvation Dynamics: Coumarin 153 Revisited. *J. Phys. Chem.*, 99:17311–17337, 1995.
- [46] M. Maroncelli, X.-X. Zhang, M. Liang, D. Roy, and N. P. Ernsting. Measurements of the complete solvation response of coumarin 153 in ionic liquids and the accuracy of simple dielectric continuum predictions. *Faraday Discuss.*, 154:409–424, 2012.
- [47] N. Ito, S. Arzhantsev, M. Heitz, and M. Maroncelli. Solvation dynamics and rotation of coumarin 153 in alkylphosphonium ionic liquids. *J. Phys. Chem. B*, 108:5771–5777, 2004.
- [48] J. V. Lockard and M. R. Wasielewski. Intramolecular electron transfer within a

- covalent, fixed-distance donor-acceptor molecule in an ionic liquid. *J. Phys. Chem. B*, 111:11638–11641, 2007.
- [49] M. Bodanszky. *Principles of Peptide Synthesis, 2nd ed.* Springer-Verlag, New York, 2nd edition, 1993.
- [50] A. K. Burrell, R. E. D. Del Sesto, S. N. Baker, T. M. McCleskey, and G. A. Baker. The large scale synthesis of pure imidazolium and pyrrolidinium ionic liquids. *Green Chemistry*, 9:449–454, 2007.
- [51] Y. Pan, L. E. Boyd, J. F. Kruplak, W. E. Jr. Cleland, J. S. Wilkes, and C. L. J. Hussey. Physical and transport properties of bis(trifluoromethylsulfonyl)imide-based room-temperature ionic liquids: application to the diffusion of tris(2,2-bipyridyl)ruthenium(ii). *Electrochem. Soc.*, 158:F1–F9, 2011.
- [52] H. Shirota and E. W. Castner Jr. Solvation in highly nonideal solutions: A study of aqueous 1-propanol using the coumarin 153 probe. *J. Chem. Phys.*, 112:2367–2376, 2000.
- [53] Y. Sun, E. W. Castner, Jr., C. L. Lawson, and P. G. Falkowski. Biophysical characterization of natural and mutant fluorescent proteins cloned from zooxanthellate corals. *FEBS Lett.*, 570:175–183, 2004.
- [54] C. D. Grant, M. R. DeRitter, K. E. Steege, T. A. Fadeeva, and E. W. Castner, Jr. Fluorescence probing of interior, interfacial, and exterior regions in solution aggregates of poly(ethylene oxide)-poly(propylene oxide)-poly(ethylene oxide) triblock copolymers. *Langmuir*, 21:1745–1752, 2005.
- [55] Wolfgang Becker. *Advanced time-correlated single photon counting techniques*, volume Publication info: Berlin ; New York : Springer, c2005. Physical descrip: xix, 401 p. : ill. (some col.) ; 25 cm. Series:Springer series in chemical physics,ISSN0172-6218 ; 81 of *Springer series in chemical physics*. Springer, New York, 2005.
- [56] MATLAB 7.10.0. MATLAB version 7.10.0. Natick, Massachusetts: The MathWorks Inc., 2010., 2010.

- [57] P. J. Steinbach, R. Ionescu, and C. R. Matthews. Analysis of kinetics using a hybrid maximum-entropy/nonlinear-least-squares method: Application to protein folding. *Biophys. J.*, 82:2244–2255, 2002.
- [58] A.K. Livesey and J.C. Brochon. Analyzing the Distribution of Decay Constants in Pulse-Fluorimetry using the Maximum Entropy Method. *Biophys. J.*, 52:693–706, 1987.
- [59] V. A. Lórenz-Fonfría and H. Kandori. Transformation of Time-Resolved Spectra of Lifetime-Resolved Spectra by Maximum Entropy Intervention of the Laplace Transform. *Appl. Spectrosc.*, 60:407–417, 2006.
- [60] Igor Pro 6.04. Wavemetrics Igor Pro 5.04b Edition. Wavemetrics, Inc. Lake Oswego, OR, 2009.
- [61] S. S. Skourtis and D. N. Beratan. Electron transfer contact maps. *J. Phys. Chem. B*, 101(7):1215–1234, 1997.
- [62] L. A. Curtiss and J. R. Miller. Distance Dependence of Electronic Coupling Through trans alkyl Chains: Effects of Electron Correlation. *J. Phys. Chem. A*, 102(1):160–167, 1998.
- [63] J. E. Subotnik, S. Yeganeh, R. J. Cave, and M. A. Ratner. Constructing diabatic states from adiabatic states: Extending generalized Mulliken-Hush to multiple charge centers with Boys localization. *J. Chem. Phys.*, 129(24):244101, 2008.
- [64] J. E. Ridley and M. C. Zerner. An intermediate neglect of differential overlap technique for spectroscopy: Pyrrole and the azines. *Theor. Chim. Acta*, 32:111, 1973.
- [65] M. J. S. Dewar, E. G. Zoebisch, E. F. Healy, and J. J. P. Stewart. Development and use of quantum mechanical molecular models. 76. am1: a new general purpose quantum mechanical molecular model. *J. Am. Chem. Soc.*, 107(13):3902–3909, 1985.

- [66] M. J. Frisch, G. W. Trucks, H. B. Schlegel, G. E. Scuseria, M. A. Robb, J. R. Cheeseman, G. Scalmani, V. Barone, B. Mennucci, G. A. Petersson, H. Nakatsuji, M. Caricato, X. Li, H. P. Hratchian, A. F. Izmaylov, J. Bloino, G. Zheng, J. L. Sonnenberg, M. Hada, M. Ehara, K. Toyota, R. Fukuda, J. Hasegawa, M. Ishida, T. Nakajima, Y. Honda, O. Kitao, H. Nakai, T. Vreven, J. A. Montgomery, Jr., J. E. Peralta, F. Ogliaro, M. Bearpark, J. J. Heyd, E. Brothers, K. N. Kudin, V. N. Staroverov, R. Kobayashi, J. Normand, K. Raghavachari, A. Rendell, J. C. Burant, S. S. Iyengar, J. Tomasi, M. Cossi, N. Rega, J. M. Millam, M. Klene, J. E. Knox, J. B. Cross, V. Bakken, C. Adamo, J. Jaramillo, R. Gomperts, R. E. Stratmann, O. Yazyev, A. J. Austin, R. Cammi, C. Pomelli, J. W. Ochterski, R. L. Martin, K. Morokuma, V. G. Zakrzewski, G. A. Voth, P. Salvador, J. J. Dannenberg, S. Dapprich, A. D. Daniels, . Farkas, J. B. Foresman, J. V. Ortiz, J. Cioslowski, and D. J. Fox. Gaussian 09 Revision B.01. Gaussian Inc. Wallingford CT 2009.
- [67] B. R. Brooks, R. E. Bruccoleri, B. D. Olafson, D. J. States, S. Swaminathan, and M. Karplus. CHARMM: A program for macromolecular energy, minimization, and dynamics calculations. *J. Comput. Chem.*, 4(2):187–217, 1983.
- [68] M. C. Zerner, J. E. Ridley, A. D. Bacon, W. D. Edwards, J. D. Head, J. McKelvey, J. C. Culberson, P. Knappe, M. G. Cory, B. Weiner, J. D. Baker, W. A. Parkinson, D. Kannis, J. Yu, N. Roesch, M. Kotzian, T. Tamm, M. M. Karelson, X. Zheng, G. Pearl, A. Broo, K. Albert, J. M. Cullen, J. Li, G. D. Hawkins, J. D. Thompson, C. P. Kelly, D. A. Liotard, C. J. Cramer, and D. G. Truhlar, ZINDO-MN1.2, Quantum Theory Project, University of Florida, Gainesville, and Department of Chemistry, University of Minnesota, Minneapolis, 2005.
- [69] M. Rust, J Lappe, and R.J. Cave. Multistate Effects in Calculations of the Electronic Coupling Element for Electron Transfer Using the Generalized Mulliken–Hush Method. *J. Phys. Chem. A*, 106:3930–3940, 2002.
- [70] IUPAC. Compendium of Chemical Terminology, 2nd ed. (the "Gold Book"). Compiled by A. D. McNaught and A. Wilkinson. Blackwell Scientific Publications, Oxford (1997). XML on-line corrected version: <http://goldbook.iupac.org> (2006-)

created by M. Nic, J. Jirat, B. Kosata; updates compiled by A. Jenkins. ISBN 0-9678550-9-8. doi:10.1351/goldbook.

- [71] R. M. Shirke, A. Chaudhari, N. M. More, and P. B. Patil. Dielectric measurements on methyl acetate plus alcohol mixtures at (288, 298, 308, and 318) K using the time domain techniques. *J. Chem. Eng. Data*, 45:917–919, 2000.
- [72] J.-F. Cote, D. Brouillette, J. E. Desnoyers, J.-F. Rouleau, J.-M. St.-Arnaud, and G. Perron. Dielectric constants of acetonitrile, gamma-butyrolactone, propylene carbonate, and 1,2-dimethoxyethane as a function of pressure and temperatures. *J. Solution Chem.*, 25:1163–1173, 1996.
- [73] K. Tominaga and G. C. Walker. Femtosecond Experiments on Solvation Dynamics of an Anionic Probe Molecule in Methanol. *J. Photochem. Photobiol. A: Chem.*, 87:127–133, 1995.
- [74] Mark A. Thompson. ArgusLab 4.0.1. Planaria Software LLC: Seattle, WA.
- [75] W. A. Henderson and S. Passerini. Phase behavior of ionic liquid-liquid mixtures: Pyrrolidinium cations and tfsi⁻ anions. *Chem. Mat.*, 16(15):2881–2885, 2004.
- [76] Alexander P. Demchenko. The red-edge effects: 30 years of exploration. *Luminescence*, 17:19–42, 2002.
- [77] A. Paul, P. K. Mandal, and A. Samanta. On the optical properties of the imidazolium ionic liquids. *J. Phys Chem. B*, 109:9148–9153, 2005.
- [78] Z. Hu and C. J. Margulis. Room-temperature ionic liquids: Slow dynamics, viscosity, and the red edge effect. *Acc. Chem. Res.*, 40(11):1097–1105, 2007.
- [79] Z. H. Hu and C. J. Margulis. Heterogeneity in a room-temperature ionic liquid: Persistent local environments and the red-edge effect. *Proc. Natl. Acad. Sci. U. S. A.*, 103:831–836, 2006.
- [80] Z. H. Hu and C. J. Margulis. A study of the time-resolved fluorescence spectrum and red edge effect of an⁺ in a room-temperature ionic liquid. *J. Phys. Chem. B*, 110:11025–11028, 2006.

- [81] E.-K. Park, B. Park, J.-H. Choi, K. Choi, and M. Cho. Chirality Transfer Effects in Proline-Substituted Coumarin Compounds. *J. Phys. Chem. B*, 113:11301–11305, 2009.
- [82] K. Sahu, S. J. Kern, and M. A. Berg. Heterogeneous reaction rates in an ionic liquid: Quantitative results from two-dimensional multiple population-period transient spectroscopy. *J. Phys. Chem. A*, 115:7984–7993, 2011.
- [83] K. W. Penfield, J. R. Miller, M. N. Paddon-Row, E. Cotsaris, A. M. Oliver, and N. S. Hush. Optical and Thermal Electron Transfer in Rigid Difunctional Molecules of Fixed Distance and Orientation. *J. Am. Chem. Soc.*, 109:5061–5065, 1987.
- [84] B. Paulson, K. Pramod, P. Eaton, G. Closs, and J. R. Miller. Long-Distance Electron Transfer through Rodlike Molecules with Cubyl Spacers. *J. Phys. Chem.*, 97:13042–13045, 1993.
- [85] A. M. Napper, N. J. Head, A. M. Oliver, M. J. Shephard, M. N. Paddon-Row, I. Read, and D. H. Waldeck. Use of U-shaped Donor-Bridge-Acceptor Molecules to Study Electron Tunneling through Nonbonded Contacts. *J. Am. Chem. Soc.*, 124:10171–10181, 2002.

Chapter 3

Differences in Intermediate Range Order Between NTf₂⁻-Anion Ionic Liquids with Alkyl- vs. Ether-Substituted Cations

3.1 Background on Structural Ordering of Ionic Liquids

A theoretical description of the liquid state can be given in terms of the potential of mean force, which is a function of the pair distribution function of the molecular species in the liquid. This pair distribution function is obtained from x-ray/neutron scattering experiments from the inverse Fourier transform of the structure function, $S(q)$ given below.¹

$$S(q) = \frac{I_{coh}(q) - \sum_i x_i f_i^2(q)}{\left[\sum_i x_i f_i(q) \right]^2}, \quad (3.1)$$

where $I_{coh}(q)$ is the coherent x-ray intensity, x_i is the atomic fraction and f_i is the atomic form factor, both for the atom type, i .

The liquid structure can also be obtained theoretically from molecular dynamics calculations. Kashyap, *et al.*² have used molecular dynamics simulations to reproduce experimental structure function data from x-ray scattering experiments and partition the $S(q)$. Their results showed that a first sharp diffraction peak (FSDP) or ‘pre-peak,’ one of the prominent features in the observed $S(q)$ of ILs, is an indication of intermediate charge ordering (commonly defined as ordering in region around 10 – 30 Å for ILs).

The heterogeneous structural ordering of ILs have been discussed by many groups both experimentally^{4–9} and computationally.^{2,10–14} Specifically, the role of the apolar hydrocarbon chain of the cation on the structural ordering of the ILs has been

studied extensively. Urahata and Ribeiro¹⁵ calculated the structure factors for imidazolium based IL series that showed a FSDP for the cations with the longest tails (octyl chain). Santos, *et al.*⁴ showed similar results with the 1-alkyl-1-methylpyrrolidinium bis(trifluoromethylsulfonyl)amide ($\text{Pyr}_{1,n}^+/\text{NTf}_2^-$) ILs where the pre-peak is absent for $n=4$ but is evident for $n=6, 8$, and 10 .

What happens to the IL structure if the nonpolar hydrocarbon tails on the cations are replaced by polar substituents? Extensive reports in the literature have shown that the physical properties of the ILs change when alkyl chains are substituted with polar substituents such as ethers,^{16–18} alkylsilyl,¹⁹ and alkylsiloxo groups.²⁰ For example, in the case for the NTf_2^- anion based ILs with phosphonium and ammonium cations, Shirota, *et al.*¹⁸ showed reduction of viscosity and increase of the surface tension when the octyl chain on the cation was substituted with a (2-ethoxyethoxy)ethyl group. They have attributed the difference in the surface tension to the stronger interionic interactions caused by the ether groups and the decrease in viscosity to the increased disorder of the ether substituted chains compared to the alkyl chains.¹⁸

Triolo, *et al.*⁶ have investigated the structural ordering of the NTf_2^- anion based ILs that have different polarities in the tails (alkyl vs. ether or hydroxy terminal chains) using x-ray scattering. They showed that the FSDP is absent for the ether or hydroxy terminal chain containing cations, while FSDP is present for the ILs with cations with alkyl chains. The reasons proposed for the difference in the $S(q)$ for the ether vs. alkyl substitutes, however, are different for the aliphatic phosphonium and ammonium based ILs than for the aromatic imidazolium based ILs. They suggested that for the imidazolium based ILs, the difference between the structural ordering in the ether vs. alkyl substituted ILs is likely to arise from intramolecular hydrogen bonding.⁶ For the aliphatic ILs, there is no evidence for a possible hydrogen bonding based on the electron potential fits using the electronic structure calculations.⁶

Two-dimensional (2D) NMR methods provide another way to study structural ordering in ILs.^{21–26} One class of 2D NMR methods uses the nuclear Overhauser effect (NOE) - described in detail below- to obtain useful information on the local structure of ILs. The local structures of imidazolium based ILs have been derived by using such

methods,^{21–25} often combined with computational methods. Mantz, *et al.*²¹ reported a nano-agglomeration of IL pairs for 1-ethyl-3-methylimidazolium chloride ($\text{emim}^+/\text{Cl}^-$) by demonstrating that the intermolecular distances between the $\text{emim}^+/\text{Cl}^-$ ion pairs were less than 4 Å. Mele, *et al.*²³ have reported that a short H - -F intermolecular proximity exists between the 1-*n*-butyl-3-methylimidazolium cation and the tetrafluoroborate anion. They also showed strong NOE signals arising from the interactions between the proton atoms on the methyl chain and the the butyl chain on the cation, indicating cation–cation intermolecular interactions.²³ Castiglione, *et al.*²⁶ obtained a similar result for the 1-butyl-1-methyl pyrrolidinium based ILs, where the ^{19}F atoms of the CF_3 groups on the (perfluoroalkylsulfonyl)imide based anions showed selective interactions with certain ^1H atoms of the the pyrrolidinium ring on the cations. These studies showed that there exists a preferred ordering for the anions and cations.^{21–27}

We have used 2D NMR Overhauser effect spectroscopy to further investigate the structural ordering of a series of four aliphatic ILs reported by Shirota, *et al.*¹⁸ and discussed by Triolo, *et al.*⁶ The two pairs of bis(trifluoromethylsulfonyl)amide (NTf_2^-) based ILs are composed of the following cations: triethyloctylammonium (N_{2228}^+), triethyloctylphosphonium (P_{2228}^+), (2-ethoxyethoxy)ethyltriethylammonium ($\text{N}_{222(2\text{O}2\text{O}2)}^+$), and (2-ethoxyethoxy) ethyltriethylphosphonium ($\text{P}_{222(2\text{O}2\text{O}2)}^+$). The structures of the IL ions are shown in Figure. 3.1.

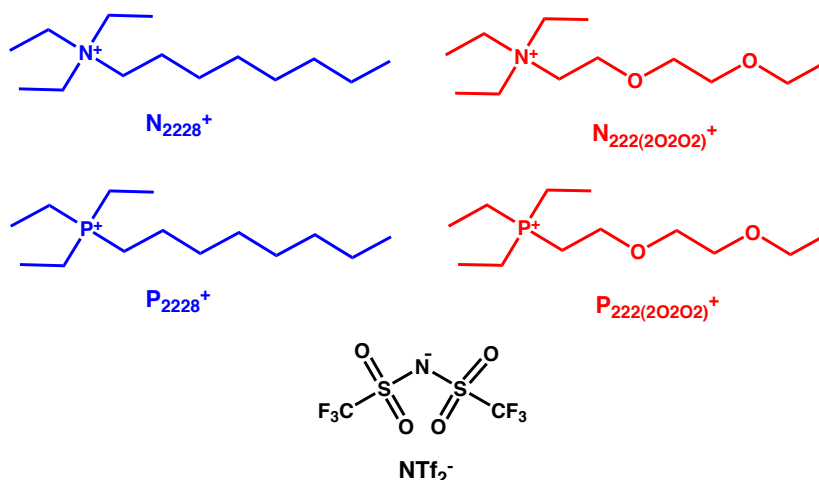


Figure 3.1: Structures of the four ionic liquids studied using 2D NMR Overhauser effect spectroscopy and x-ray scattering.

3.1.1 2D NMR Overhauser Effect Spectroscopy

Nuclear magnetic resonance (NMR) spectroscopy is a powerful technique used to determine the chemical structure of an unknown molecule using the magnetic properties of the nuclei including ^1H , ^{13}C , ^{15}N , ^{19}F , and ^{31}P . A sample is placed in a strong magnetic field, which splits the energies via the Zeeman effect, then the resonance frequencies resulting from different magnetic energy absorbed by different nuclei are observed. When the number of protons and the sum of the protons and neutrons are even, the nucleus has no magnetic properties. When the atomic number or the atomic number is odd or when both are odd, the nucleus is said to be spinning and the spin quantum number, S , is nonzero. Those nuclei with $S = 1/2$ give the sharpest spectral lines and therefore are most commonly used. Among the spin $1/2$ nuclei, proton (^1H) and fluorine (^{19}F) are favorable for detection because of their high natural abundances and gyromagnetic ratios.

Development of 2D NMR has allowed a depth of structural understanding beyond the basic connectivity of a molecule, by using coherence transfer between nuclei. Coherence transfers occur as a result of resonating frequencies of nuclei. Thus, additional information about the interactions between nuclei that are bonded or not bonded (through space) can be obtained. This not only reveals the intramolecular structure but also the structural ordering of molecules through the observation of the interactions of nuclei in a given sample.^{28,29} A basic 2D spectrum would involve stacking of plots from the repeated multiple pulse 1D sequence that vary in delay time. A simple way to understand how 2D NMR works is through an energy diagram for a two spin (α and β) system as shown in Figure 3.2 and knowing the general pulse sequence as described below.

A general 2D NMR technique uses a variation of the following sequence:

$$\textit{Preparation} - \textit{Evolution} (t_1) - \textit{Acquisition} (t_2) \quad (3.2)$$

During the *preparation* period, the spin system is perturbed with pulses on the nuclei allowing the system to relax. The sequence then enters the *evolution* time period, t_1 , with a $\pi/2$ pulse, where all the magnetizations with the 1D frequencies of A1, A2, X1, and X2 are labeled. With the second $\pi/2$ pulse, the magnetization frequencies are

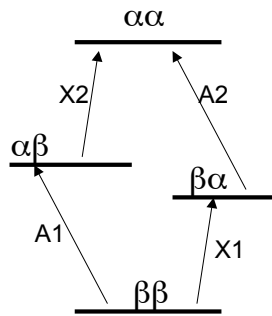


Figure 3.2: The energy diagram for an AX spin system, adopted from Lamber and Mazzola³⁰

transferred from one nucleus to another; for example, the magnetization frequency of A1 can be transferred to any of A2, X1 and X2 transitions. This happens during the *acquisition* time, t_2 . The resulting spectrum, then, contains off-diagonal peaks that represent frequencies that are modulated by other transition frequencies. For example, the frequency of A1 that was modulated with X1 during t_2 will yield a frequency peak, (ν_{A1}, ν_{X1}) on a two dimensional spectrum.

Among the 2D NMR methods, the one that interests us uses the nuclear Overhauser effect (NOE)–through space coherence. The NOE occurs when one nucleus is irradiated with a magnetic field, which then transfers nuclear spin polarization from one spin to another via cross dipole-dipole relaxation. This is different from common spin-spin coupling techniques because NOE interactions occur through space, not through bonds. One of the biggest application of NOESY (nuclear Overhauser effect spectroscopy) is in the study of protein structures and dynamics. For the structural studies of ILs, however, exact bond distances are not reported quantitatively but averaged ranges of distances are reported since liquids do not have static structures.

A typical pulse sequence for a NOE experiment is as follows:

$$\pi/2 - \text{Evolution } (t_1) - \pi/2 - \text{Mix } (\tau_m) - \pi/2 - \text{Acquisition } (t_2). \quad (3.3)$$

One may notice that there is an additional sequence period called *mix* or mixing time, τ_m added to the general 2D NMR sequence that was represented in Eq.3.2. The physics behind this pulse sequence is the same as that previously explained for the general 2D NMR, however for a NOE experiment, mixing time serves as the period when the frequency of magnetization of the irradiated nucleus is transferred to the observed nucleus.

The coherence transfer is then observed at a new frequency during the acquisition time (t_2). This transfer of frequencies allow for two-dimensional representation that yields cross-peaks. The NOESY pulse sequence used in this study is shown in Figure 3.3.

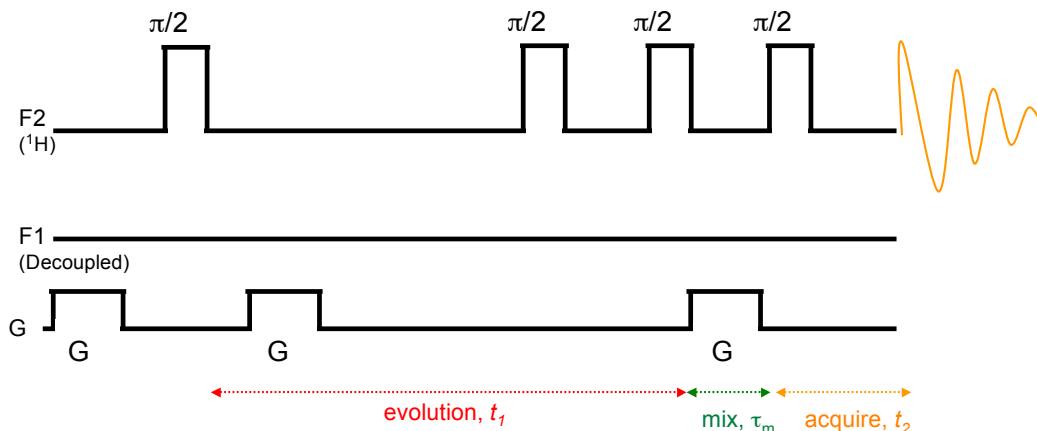


Figure 3.3: The 2D NMR NOESY pulse sequence used in this study. F1 is ^1H and G is for gradient pulses. The pulse sequence is a default pulse sequence given by the VNMRJ-2.2C software.

Because through space interactions can be observed, intermolecular interaction strengths can be determined with the NOESY by the following equation:³¹

$$\eta_A(B) = K(r_{AB})^{-6}, \quad (3.4)$$

where $\eta_A(B)$ is the NOE intensity of nucleus A following the irradiation of nucleus B, which gives saturation of spin. The internuclear distance is denoted as r_{AB} and K is a constant, “which includes the effects of molecular tumbling and alternative relaxation pathways; normally, the value of K is difficult to determine.”²¹ To calculate the internuclear distance, the ratio between two NOEs are compared. (assuming that K and other experimental conditions are the same for both NOE experiments). According to Eq. 3.4, there is a distance dependence of r_{AB}^{-6} for the NOE, allowing the nuclear distances $< 5 \text{ \AA}$ to have significant NOE intensity signals and to be assigned as nuclear interactions.³¹

In heteronuclear NOE spectroscopy (HOESY), two different nuclei are used. HOESY is particularly useful for elucidating the structural ordering of cations and anions in ILs because common ionic liquids often have cations with ^1H nuclei and anions with ^{19}F . Both ^1H and ^{19}F nuclei have predominant isotopes and large gyromagnetic ratios ($\gamma/2\pi$

= 42.576 MHz/T for ^1H and 40.053 MHz/T for ^{19}F); thus, they produce very strong NMR spectral lines. Therefore, intermolecular interactions between the cation and anion can readily be determined using this technique by observing the voids in the HOESY spectra (absence of the cation-anion interactions) and the cross-peaks in the HOESY spectra (strong interactions between the nearby cations and anions). When heteronuclear NOE is considered, a distinction must be made between the radio frequency (RF) irradiated nucleus (F1) and the observed nucleus (F2). The observed nucleus is often the sensitive nucleus, such as ^1H , and the RF-irradiated nucleus is usually the less sensitive heteronucleus, such as ^{19}F , ^{31}P , ^{15}N , and ^{13}C .

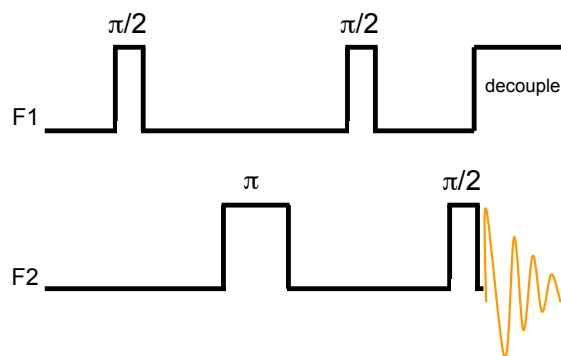


Figure 3.4: Basic 2D NMR HOESY pulse sequence developed by Rinaldi³² and Yu and Levy.^{33,34} F1 denotes the observed 'sensitive' nucleus and F2 denotes the irradiated 'insensitive' nucleus.

A basic HOESY sequence, first developed by Rinaldi³² and Yu and Levy,^{33,34} is shown in Figure 3.4. Because most 2D HOESY experiments suffer from t_1 noise artifacts, Bauer³⁵ developed a modified, inverse-HOESY pulse sequence that provides enhanced sensitivity using pulsed field gradients (PFG). The gradient strengths used are G1 and G3, which are determined by $G1/G3 = \gamma_{F1}/\gamma_{F2}$. We recall that γ is the gyromagnetic ratio and F2 represents the observed sensitive nucleus and F1 is the irradiated less sensitive heteronucleus. In the pulse sequence, G2 gradient is a "homospoil gradient, purging unwanted residual transverse magnetization present during the mixing period, and is not required to be any specific gradient strength."³⁶ The proposed PFG enhanced inverse-HOESY pulse sequence is shown in Figure 3.5.

A 2D HOESY pulse sequence that reduces t_1 noise even further was reported by Alam, *et al.*³⁶ This was done by adding an extra $\pi/2$ pulse before the third gradient

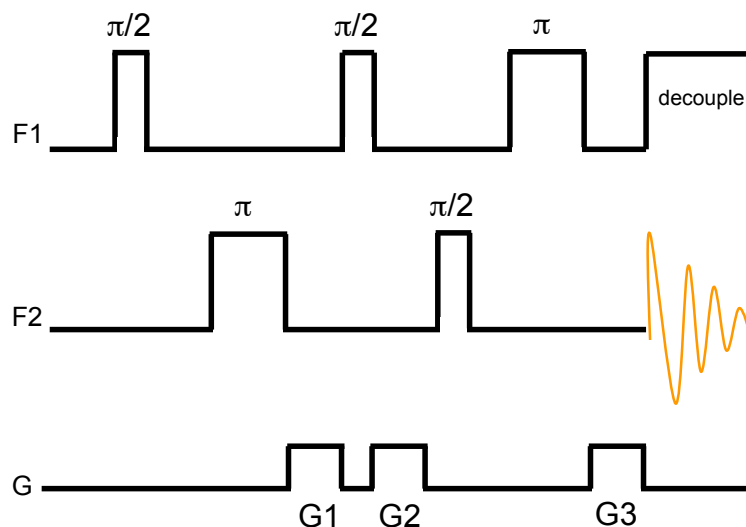


Figure 3.5: Pulse field gradient enhanced inverse-2D HOESY sequence developed by Bauer.³⁵ F1 is the RF irradiated less sensitive heteronucleus and F2 is the observed sensitive (often ^1H) nucleus. G represents the gradient strength; G1, G2, and G3 are the pulse field gradients.

pulse, G3, as shown in Figure 3.6. This pulse sequence shown in Figure 3.6 was used by Castiglione, *et al.*²⁶ to investigate the structural organization of pyrrolidinium-based ionic liquids, and they have demonstrated its effectiveness. The complete 2D HOESY pulse sequence used for the results reported hereafter is shown in Figure 3.7, which includes the preparation period that includes additional $\pi/2$ pulses and pulse field gradients to perturb the system before the acquisition.

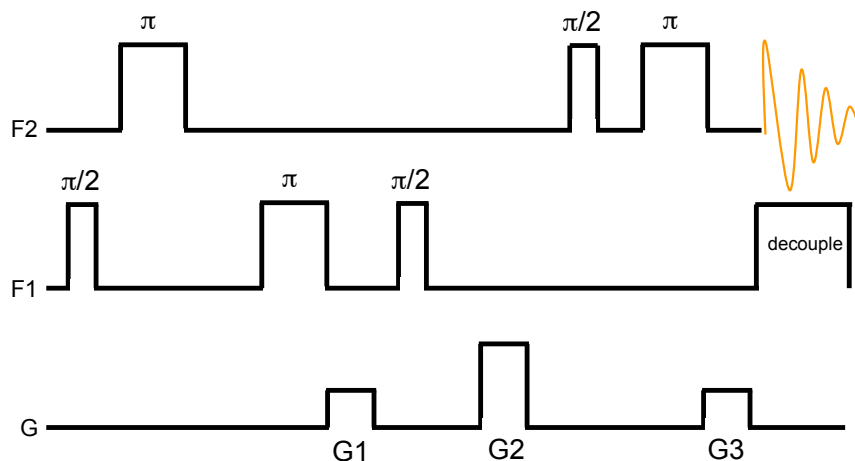


Figure 3.6: Sequence for pulse field gradient enhanced inverse-HOESY NMR by Alam, *et al.*³⁶ F1 is the RF irradiated less sensitive heteronucleus and F2 is the observed sensitive (often ^1H) nucleus. G represents the gradient strength; G1, G2, and G3 are the pulse field gradients.

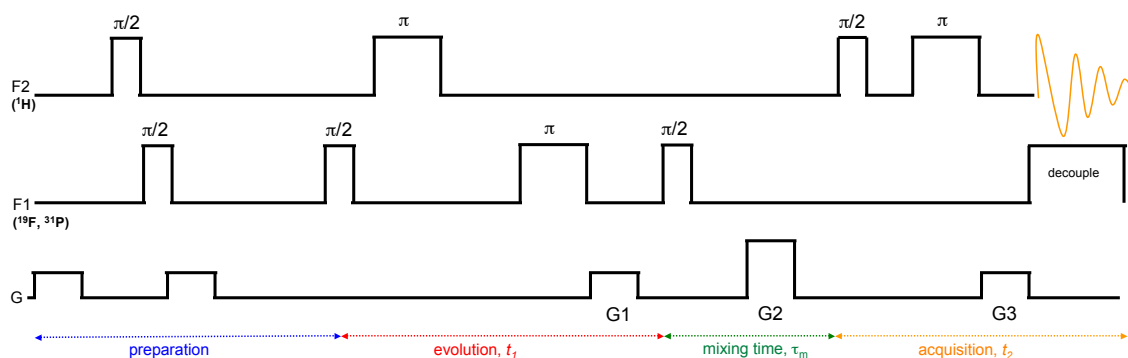


Figure 3.7: The complete 2D pulse field gradient enhanced inverse-HOESY sequence used in this study. The pulse sequence was developed by Alam.³⁶ F1 is the RF irradiated less sensitive heteronucleus (either ^{19}F or ^{31}P) and F2 is the observed ^1H nucleus. G represents the gradient strength; G1, G2, and G3 are the pulse field gradients.

3.2 Experimental Methods

3.2.1 Sample Preparation for NMR Spectroscopy

Ionic liquids are hygroscopic^{37–40} and their physical and chemical properties are sensitive to water content. This requires ILs to be preserved in a dry condition once they have been dried. All the ILs used in this study were provided by Prof. Shirota and were dried under vacuum ($\sim 10^{-2}$ Torr) for > 48 hours, ensuring the concentration of water to be < 10 ppm. The dried ILs were transferred to the NMR tubes (inner diameter 2.34 mm and outer diameter 3.30 mm, purchased from Wilmad-LabGlass, model no. 517-INNER) in an inert-atmosphere glove box (< 0.1 ppm H_2O). The NMR tubes were then flame sealed. The IL-containing NMR tube was put in a larger diameter NMR tube (outer diameter 4.20 mm and inner diameter 4.97 mm, purchased from Wilmad-LabGlass model, no. 517-OUTER) containing a small amount of D_2O for a chemical shift reference and lock frequency. A diagram showing the sample setup is shown in Fig. 3.8.

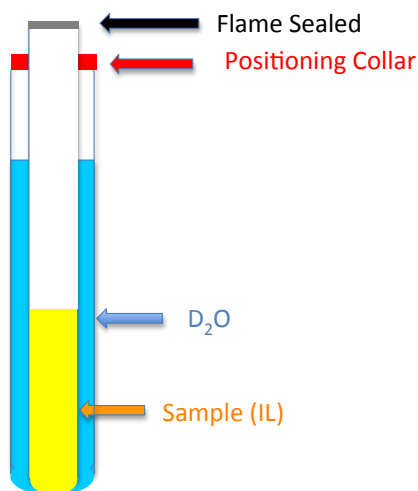


Figure 3.8: Diagram of the flame sealed coaxial NMR tube sample set up.

3.2.2 NMR Measurements

The ^1H , ^{19}F , and ^{31}P NMR spectra were recorded on both Varian 300 MHz and 400 MHz spectrometers. The Varian 300 MHz spectrometer is equipped with quad-nuclear probe with fast auto-switching between ^1H and ^{19}F frequencies, so the $\{^{19}\text{F}-^1\text{H}\}$ -HOESY measurements were done on this instrument. The Varian 400 MHz spectrometer is equipped with a four-nuclei switchable probe; $\{^{31}\text{P}-^1\text{H}\}$ -HOESY and $\{^{19}\text{F}-^{31}\text{P}\}$ -HOESY measurements were done on this instrument. 2D $\{^1\text{H}-^1\text{H}\}$ -NOESY and $\{^1\text{H}-^1\text{H}\}$ -ROESY experiments were also done on the 400 MHz instrument. The NMR experiments were all done at 313.1 K.

For each of the four ILs, a mixing time (t_m) window of 0 to 50 ms was used. Heimer, *et al.* reported that for the imidazolium cation and tetrafluoroborate anion based ILs, mixing times greater than 50 ms resulted in too much contribution from spin diffusion and gave hydrogen–hydrogen distances that are unrealistically too short.²⁵ Castiglione, *et al.* have also reported that mixing times shorter than 50 ms is the appropriate range for the pyrrolidinium based ILs.²⁶

The 2D $\{^1\text{H}-^1\text{H}\}$ -NOESY experiments were done using a mixing time of 40 ms. The pulse sequence used for 2D $\{^1\text{H}-^1\text{H}\}$ -NOESY was shown above in Figure 3.3, which was the default pulse sequence in VNMRJ-2.2C software used. The 2D HOESY

experiments were carried out using the previously reported procedures.²⁶ The inverse-detected HOESY pulse sequence used for all of the 2D NMR experiments was shown in Fig. 3.7. It was adapted from a previously reported sequence that suppresses t_1 spectral artifacts.³⁶ The 2D NMR experiments were done using a total of 128 increments were recorded in the t_1 dimensions with 8 scans for each experiment. The NMR data were analyzed using MestReNova NMR software.⁴¹

3.2.3 Electronic Structure Calculations of the Cation Charges

The electronic structure calculations of the NTf_2^- anion were reported previously.⁴² The geometry optimization and the effective charge calculations were also reported by Shirota, *et al.*¹⁸ for the four cations of the ILs studied in this research. However, to investigate beyond the all-*trans* conformations of the cations, we performed additional quantum calculations on these cations in several geometries. The DFT electronic structure computations were done using Gaussian 09⁴³ at the B3LYP⁴⁴/6-31+G(d,p) level.⁴⁵ The calculations were done both in the gas-phase and using a polarized continuum solvation model with static dielectric constant of 36. The geometry of each molecule was varied by starting with different dihedral angles (varying in increments of 20 degrees) in the octyl or 2-ethoxyethoxyethyl chains. The effective charges were calculated for the optimized geometries, using the Pop=CHelpG algorithm⁴⁶ to fit atom-centered charges to the electrostatic potential.

3.3 Results

3.3.1 Results from Overhauser Effect from 2D NMR Spectroscopy

The ^1H NMR spectra of $\text{P}_{2228}^+/\text{NTf}_2^-$, $\text{P}_{222(2\text{O}2\text{O}2)}^+/\text{NTf}_2^-$, $\text{N}_{2228}^+/\text{NTf}_2^-$, and $\text{N}_{222(2\text{O}2\text{O}2)}^+/\text{NTf}_2^-$ were previously reported by Shirota, *et al.*¹⁸ The 1D ^1H spectra with spectral assignments, along with the atom-numbered chemical structures of the cations, are displayed as insets along with each of the corresponding 2D NMR spectra in Figures 3.9 through 3.16. The 2D $\{^1\text{H}-^1\text{H}\}$ -NOESY spectra of $\text{P}_{2228}^+/\text{NTf}_2^-$, $\text{P}_{222(2\text{O}2\text{O}2)}^+/\text{NTf}_2^-$, $\text{N}_{2228}^+/\text{NTf}_2^-$, $\text{N}_{222(2\text{O}2\text{O}2)}^+/\text{NTf}_2^-$ are shown in Figure 3.9,

3.10, 3.11, and 3.12, respectively. For clarity, NOESY spectra are presented as color density plots with the color gradient defined in corresponding legend to the right of the graph. The results of NOESY experiments are not illuminating because only the intramolecular nuclei that are in proximity displayed cross-peaks. Although 2D NOESY can be used to distinguish intermolecular vs intramolecular interactions,²³ the signal overlap between the intermolecular and intramolecular NOEs can limit this technique for distinguishing cation-cation or anion-anion intermolecular structuring for ILs.²⁶ Therefore, we do not make such analyses with the NOESY data reported here. The 2D $\{^1\text{H}-^1\text{H}\}$ -NOESY spectra reported for the four ILs contain cross-peaks that arise from intramolecular NOE (from nuclei that are in proximity of the observed nuclei), and no clear intermolecular coherence signals are shown.

The 2D $\{^{19}\text{F}-^1\text{H}\}$ -HOESY experiment results for the four ILs are shown in Figures 3.13, 3.14, 3.15, and 3.16 and are summarized in Table 3.1 and Table 3.2 as normalized effective integration values per atom. The normalized effective integration values per atom are defined as the normalized integration value (I_i) divided by the number of proton nuclei giving rise to NOE (n_i): $(I_i / n_i) / \sum_i^j I_i / n_i \dots I_j / n_j$. normalized effective integration values per atom, for a range of mixing times from 0 to 50 ms. These values provide better sense of the heteronuclear NOE each proton nuclei on the cations experiences from the fluorine atoms on the anions. The results shown in the tables are also summarized as bar graphs in Figures 3.18 and 3.19.

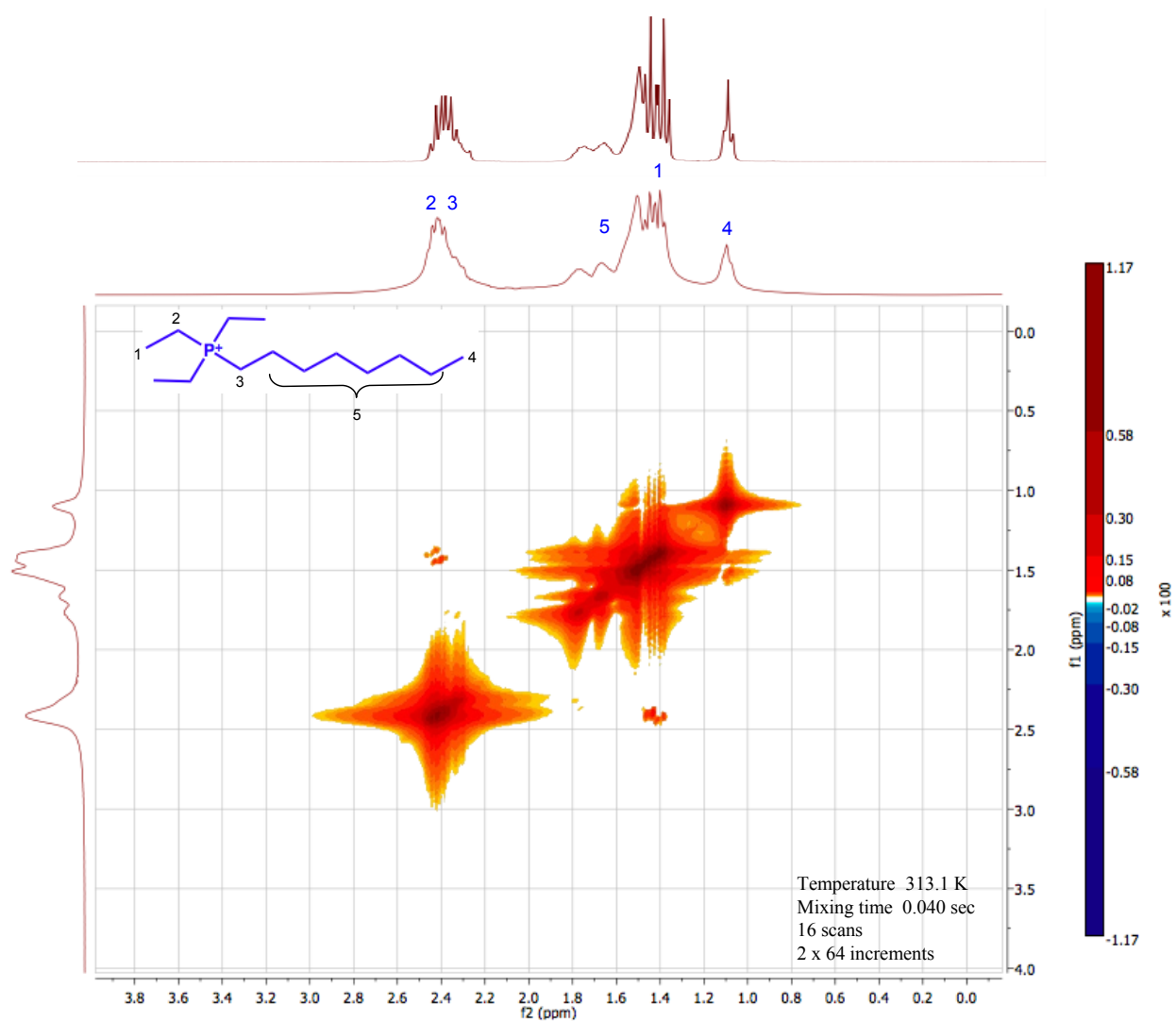


Figure 3.9: Color density plot of the 2D $\{^1\text{H}-^1\text{H}\}$ -NOESY spectrum of $P_{2228}^+/\text{NTf}_2^-$ taken with 40 ms mixing time at 313 K. F_2 axis is the observed ^1H spectra and F_1 is the irradiated ^1H spectra. High resolution 1D ^1H NMR spectrum is shown on top.

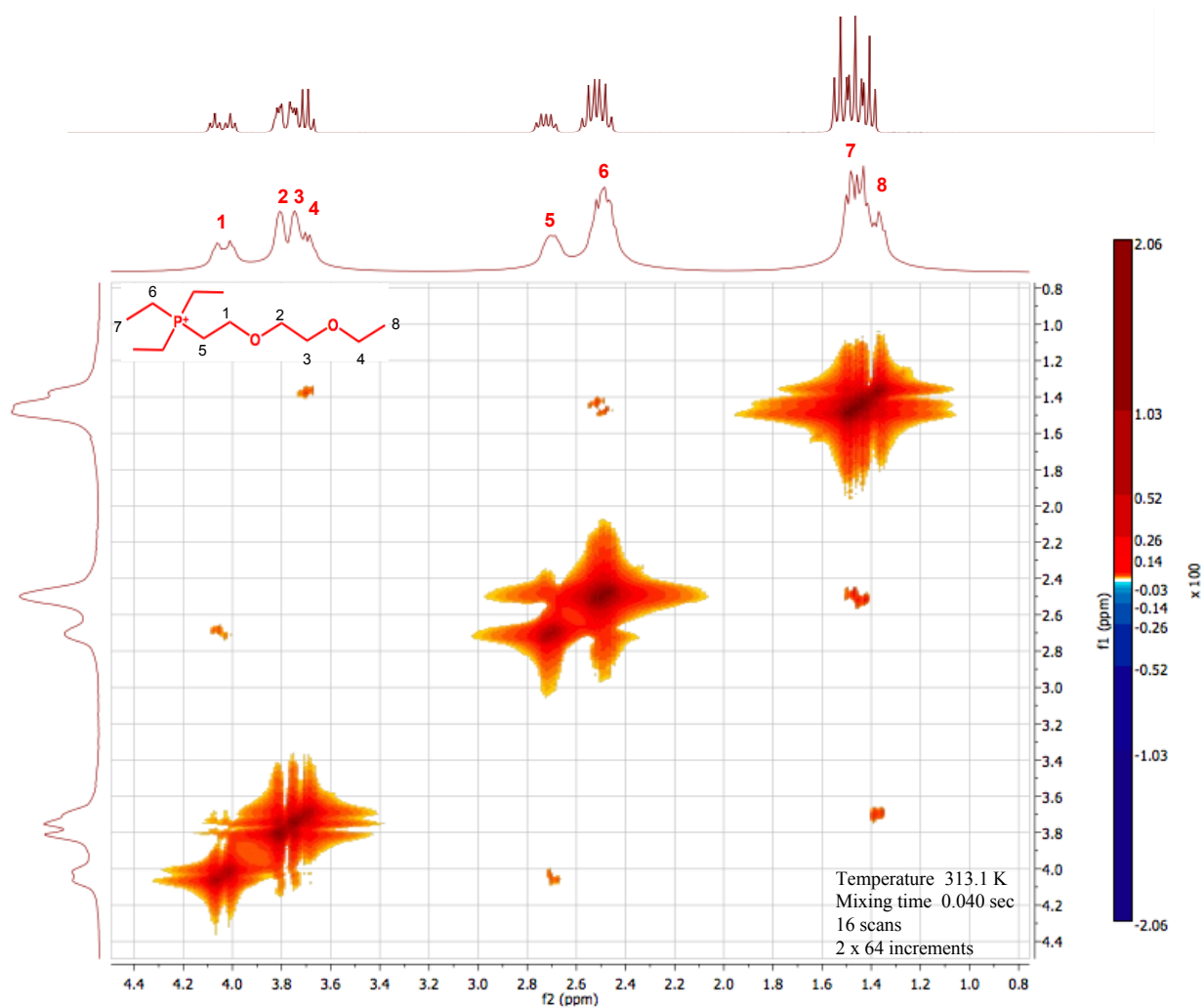


Figure 3.10: Color density plot of the 2D $\{^1\text{H}-^1\text{H}\}$ -NOESY spectrum of $\text{P}_{222}(\text{2O}_2\text{O}_2)^+/\text{NTf}_2^-$ taken with 40 ms mixing time at 313 K. F2 axis is the observed ^1H spectra and F1 is the irradiated ^1H spectra. High resolution 1D ^1H NMR spectrum is shown on top.

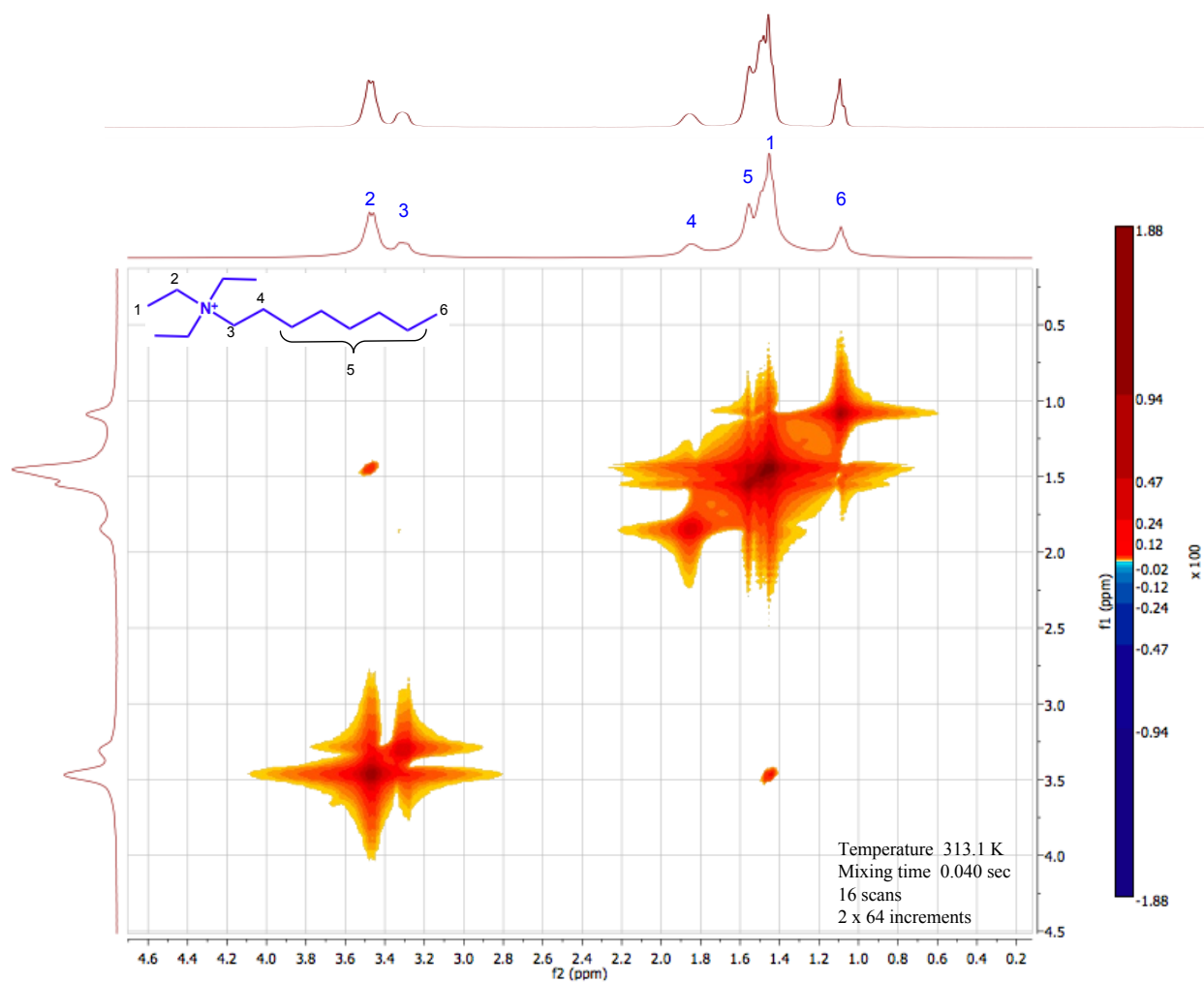


Figure 3.11: Color density plot of the 2D $\{^1\text{H}-^1\text{H}\}$ -NOESY spectrum of $\text{N}_{2228}^+/\text{NTf}_2^-$ taken with 40 ms mixing time at 313 K. F2 axis is the observed ^1H spectra and F1 is the irradiated ^1H spectra. High resolution 1D ^1H NMR spectrum is shown on top.

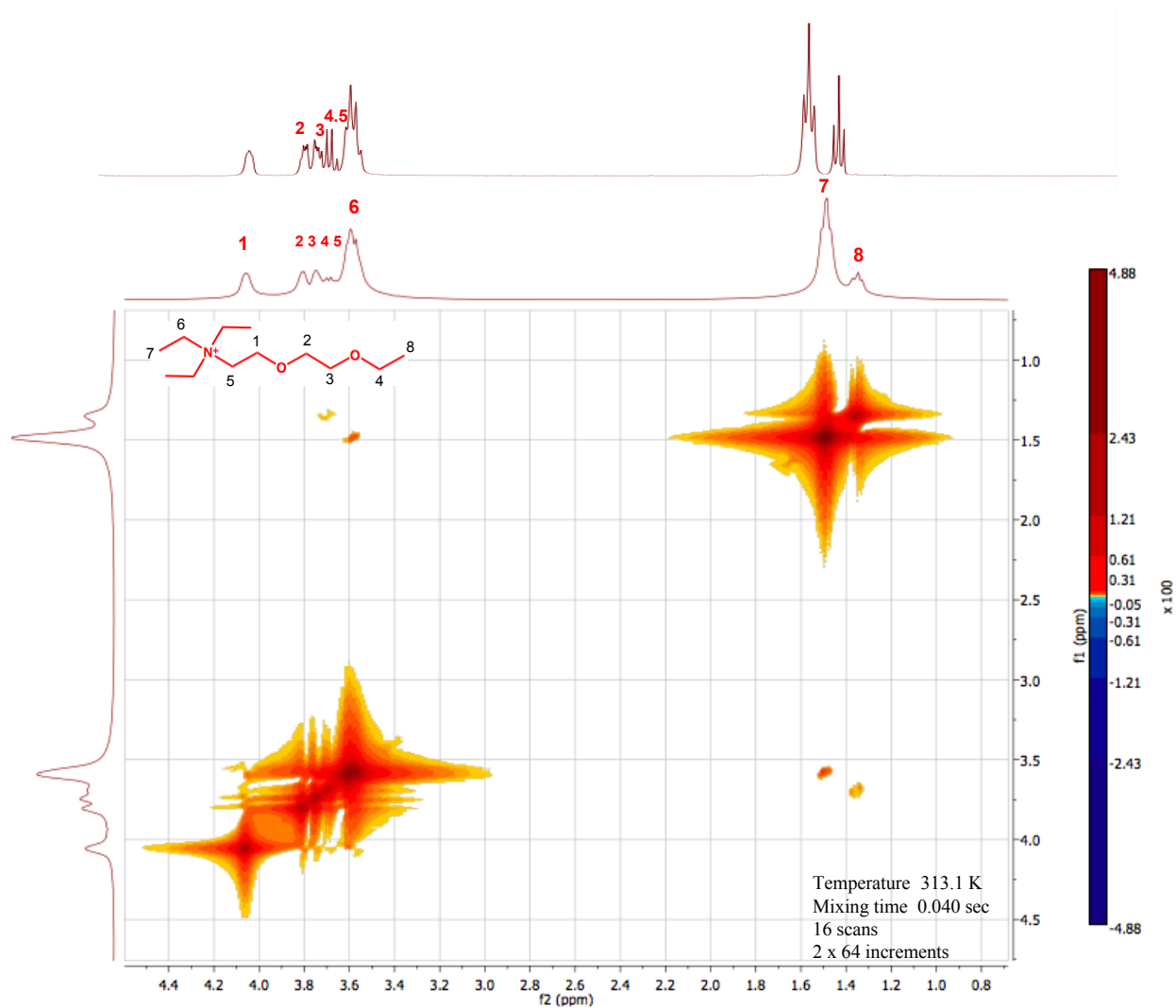


Figure 3.12: Color density plot of the 2D $\{^1\text{H}-^1\text{H}\}$ -NOESY spectrum of $\text{N}_{222}(\text{2O}_2\text{O}_2)^+/\text{NTf}_2^-$ taken with 40 ms mixing time at 313 K. F2 axis is the observed ^1H spectra and F1 is the irradiated ^1H spectra. High resolution 1D ^1H NMR spectrum is shown on top.

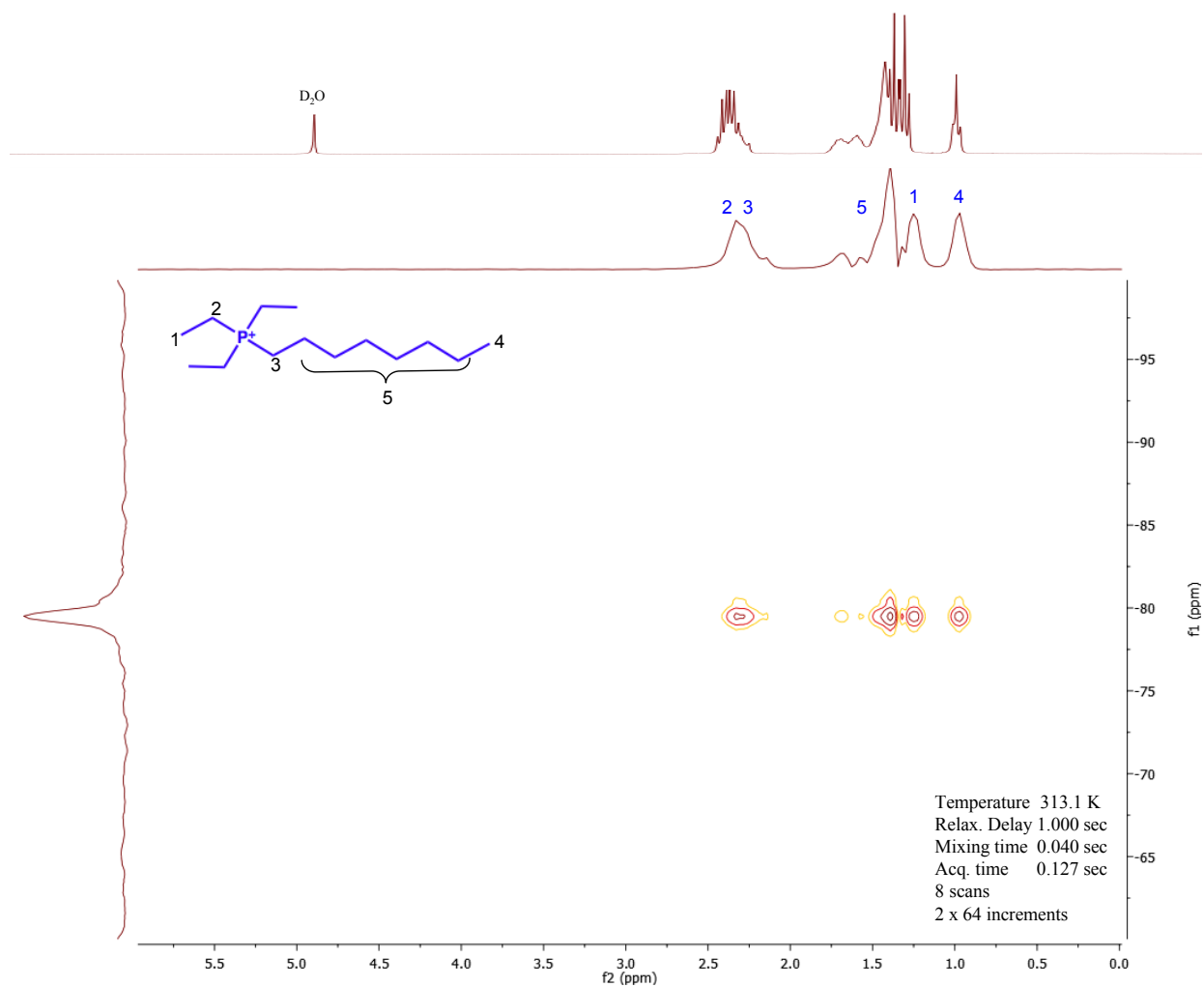


Figure 3.13: Contour plot of the $\{^{19}\text{F}-^1\text{H}\}$ -HOESY spectrum of $\text{P}_{2228}^+/\text{NTf}_2^-$. F2 axis is the observed ^1H spectra and F1 is the irradiated ^{19}F spectra. High resolution 1D ^1H NMR spectrum is shown on top.

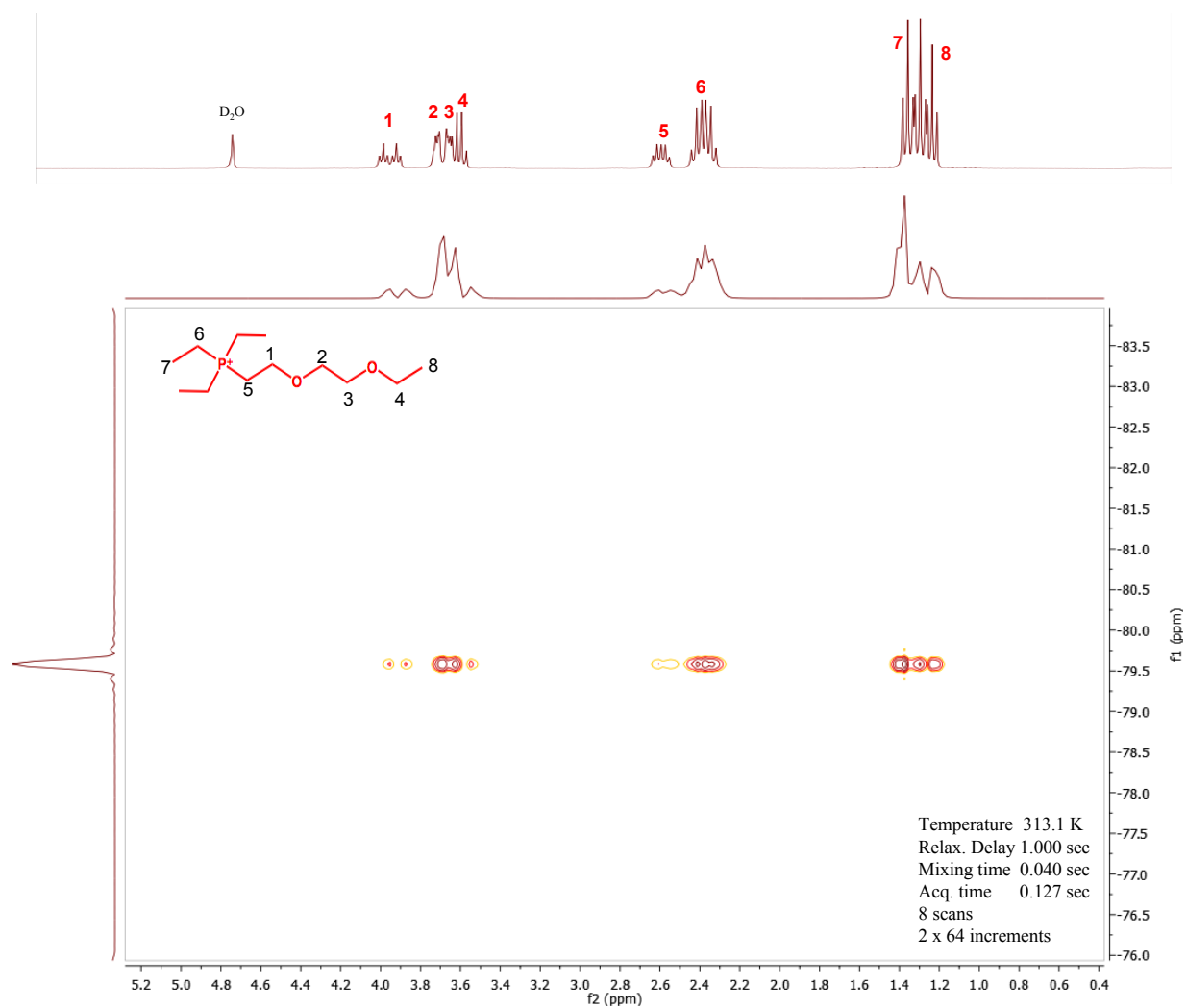


Figure 3.14: Contour plot of the $\{^{19}\text{F}-^1\text{H}\}$ -HOESY spectrum of $\text{P}_{222}(\text{2O}_2\text{O}_2)^+/\text{NTf}_2^-$. f_2 axis is the observed ^1H spectra and f_1 is the irradiated ^{19}F spectra. High resolution 1D ^1H NMR spectrum is shown on top

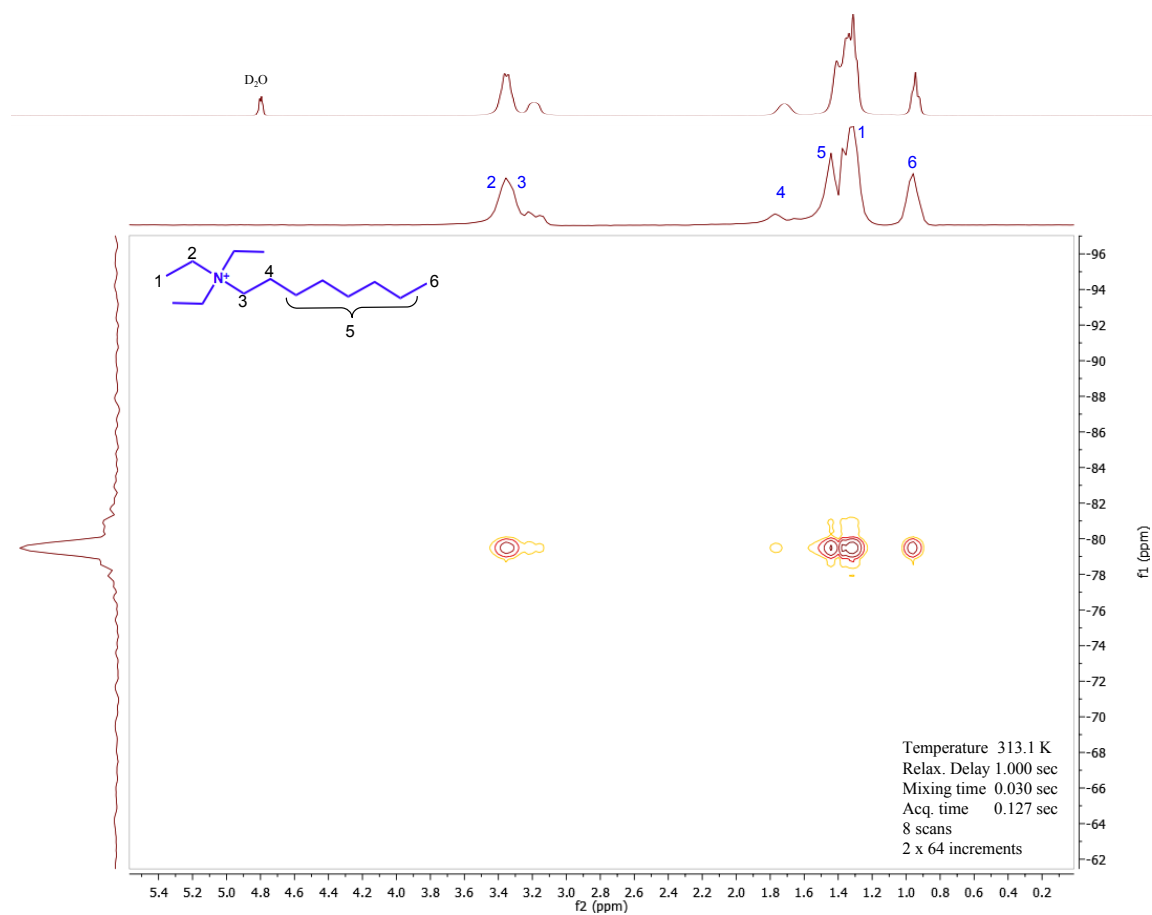


Figure 3.15: Contour plot of the $\{^{19}\text{F}-^1\text{H}\}$ -HOESY spectrum of $N_{2228}^+/\text{NTf}_2^-$. F2 axis is the observed ^1H spectra and F1 is the irradiated ^{19}F spectra. High resolution 1D ^1H NMR spectrum is shown on top

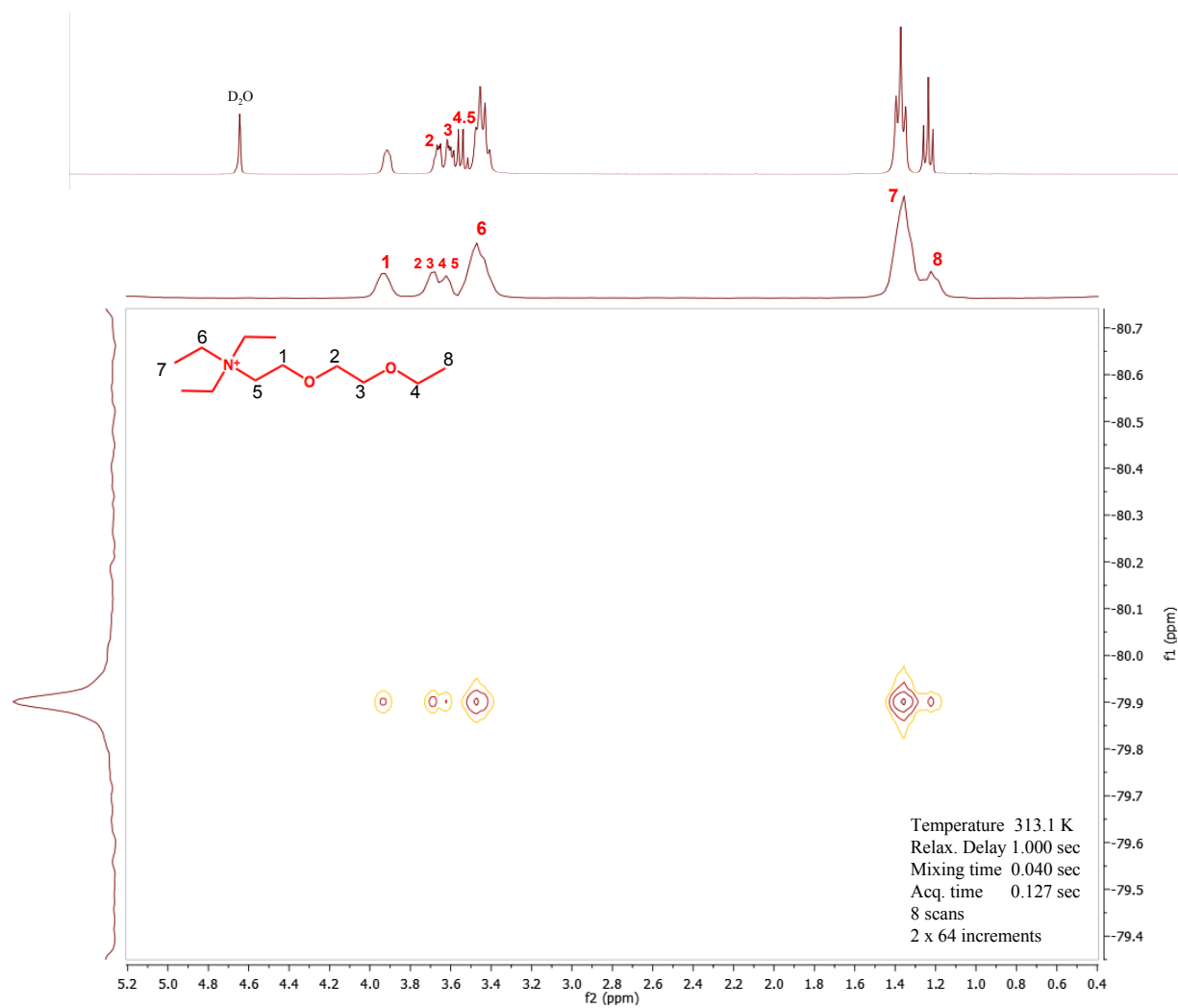


Figure 3.16: Contour plot of the $\{^{19}\text{F}-^1\text{H}\}$ -HOESY spectrum of $\text{N}_{222}(\text{2O}_2\text{O}_2)^+/\text{NTf}_2^-$. f_2 axis is the observed ^1H spectra and f_1 is the irradiated ^{19}F spectra. High resolution 1D ^1H NMR spectrum is shown on top

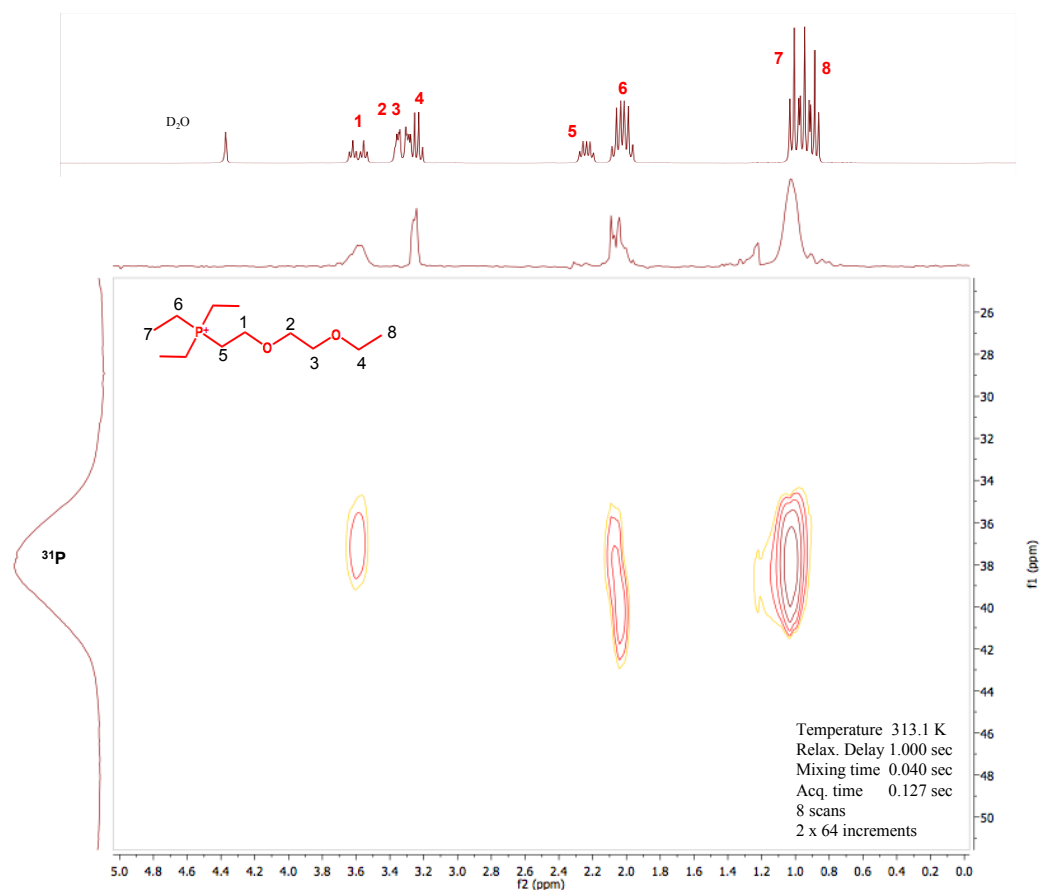


Figure 3.17: Contour plot of the $\{^{31}\text{P}-^1\text{H}\}$ -HOESY spectrum of $\text{P}_{222}(\text{2O}_2\text{O}_2)^+/\text{NTf}_2^-$. F2 axis is the observed ^1H spectra and F1 is the irradiated ^{31}P spectra. High resolution 1D ^1H NMR spectrum is shown on top

Table 3.1: Normalized effective integral value for each proton (normalized integration values divided by the number of protons) for each cation at different mixing times for P_{2228}^{+}/NTf_2^{-} and $P_{222(2O_2O_2)}^{+}/NTf_2^{-}$. The integral values were calculated and normalized using the default integration option by MestReNova 7.1.0. NMR software.

P2228+ (# protons)	9	8	3	12				
mixing time (ms)	H1	H2,3	H4	H5	total intensity			
0	9.23	15.92	6.44	15.69	47.28			
normalized	0.195	0.337	0.136	0.332	1.000			
divided by #H	0.022	0.042	0.045	0.028	0.137			
normalized intensity	0.159	0.308	0.332	0.202	1.000			
10	11.09	18.66	6.46	17.57	53.78			
normalized	0.206	0.347	0.120	0.327	1.000			
divided by #H	0.023	0.043	0.040	0.027	0.134			
normalized intensity	0.172	0.325	0.300	0.204	1.000			
20	106.13	175.46	88.53	203.35	573.47			
normalized	0.185	0.306	0.154	0.355	1.000			
divided by #H	0.948	0.909	1.133	1.069	4.059			
normalized intensity	0.185	0.306	0.154	0.355	1.000			
30	22.5	37.88	18.53	44.94	123.85			
normalized	0.182	0.306	0.150	0.363	1.000			
divided by #H	0.020	0.038	0.050	0.030	0.139			
normalized intensity	0.146	0.276	0.360	0.218	1.000			
40	80.93	46.18	76.28	158.58	361.97			
normalized	0.224	0.128	0.211	0.438	1.000			
divided by #H	0.025	0.016	0.070	0.037	0.148			
normalized intensity	0.168	0.108	0.476	0.247	1.000			
50	19.59	28.33	19.23	42.37	109.52			
normalized	0.179	0.259	0.176	0.387	1.000			
divided by #H	0.020	0.032	0.059	0.032	0.143			
normalized intensity	0.139	0.226	0.409	0.225	1.000			
P222(2O2O2)+ (# protons)	2	2	2	2	2	6	12	
mixing time (ms)	H1	H2	H3	H4	H5	H6	H7,8	total intensity
0	2.23	46.18	40.33	1.1	3.92	66.43	100.21	260.4
normalized	0.009	0.177	0.155	0.004	0.015	0.255	0.385	1.000
divided by #H	0.004	0.089	0.077	0.002	0.008	0.043	0.032	0.255
normalized intensity	0.017	0.348	0.304	0.008	0.030	0.167	0.126	1.000
10	12.09	105.67	93.04	6.3	23.39	183.91	243.86	668.26
normalized	0.018	0.158	0.139	0.009	0.035	0.275	0.365	1.000
divided by #H	0.009	0.079	0.070	0.005	0.018	0.046	0.030	0.256
normalized intensity	0.035	0.309	0.272	0.018	0.068	0.179	0.119	1.000
20	8.56	101.13	89.01	6.3	8	179.53	237.4	629.93
normalized	0.014	0.161	0.141	0.010	0.013	0.285	0.377	1.000
divided by #H	0.007	0.080	0.071	0.005	0.006	0.047	0.031	0.248
normalized intensity	0.027	0.324	0.285	0.020	0.026	0.192	0.127	1.000
30	8.56	101.13	89.01	6.3	8	179.53	237.4	629.93
normalized	0.014	0.161	0.141	0.010	0.013	0.285	0.377	1.000
divided by #H	0.007	0.080	0.071	0.005	0.006	0.047	0.031	0.248
normalized intensity	0.027	0.324	0.285	0.020	0.026	0.192	0.127	1.000
40	12.11	92.92	102.86	8.3	12.76	150.17	248.52	627.64
normalized	0.019	0.148	0.164	0.013	0.020	0.239	0.396	1.000
divided by #H	0.010	0.074	0.082	0.007	0.010	0.040	0.033	0.255
normalized intensity	0.038	0.290	0.321	0.026	0.040	0.156	0.129	1.000
50	11.05	82.39	69.37	6.24	7.34	148.51	247.08	571.98
normalized	0.019	0.144	0.121	0.011	0.013	0.260	0.432	1.000
divided by #H	0.010	0.072	0.061	0.005	0.006	0.043	0.036	0.233
normalized intensity	0.041	0.308	0.260	0.023	0.027	0.185	0.154	1.000

Table 3.2: Normalized effective integral value for each proton (normalized integration values divided by the number of protons) for each cation at different mixing times for N_{2228}^{+}/NTf_2^{-} and $N_{222(2O_2O_2)}^{+}/NTf_2^{-}$. The integral values were calculated and normalized using the default integration option by MestReNova 7.1.0. NMR software.

N2228+ (# protons)	9	6	2	2	10	3		
mixing time (ms)	H1	H2	H3	H4	H5	H6	total intensity	
0	117.42	59.55	1.34	1	39.88	35.96	255.15	
normalized	0.460	0.233	0.005	0.004	0.156	0.141	1.000	
divided by #H	0.051	0.039	0.003	0.002	0.016	0.047	0.157	
normalized intensity	0.325	0.247	0.017	0.012	0.099	0.299	1.000	
10	28.92	16.09	2.12	1.98	11.25	10.31	70.67	
normalized	0.409	0.228	0.030	0.028	0.159	0.146	1.000	
divided by #H	0.045	0.038	0.015	0.014	0.016	0.049	0.177	
normalized intensity	0.257	0.214	0.085	0.079	0.090	0.275	1.000	
20	84.11	58.92	4.22	1	44.37	38.45	231.07	
normalized	0.364	0.255	0.018	0.004	0.192	0.166	1.000	
divided by #H	0.040	0.042	0.009	0.002	0.019	0.055	0.169	
normalized intensity	0.239	0.252	0.054	0.013	0.114	0.328	1.000	
30	89.39	57.34	4.48	1	70.76	36.79	259.76	
normalized	0.344	0.221	0.017	0.004	0.272	0.142	1.000	
divided by #H	0.038	0.037	0.009	0.002	0.027	0.047	0.160	
normalized intensity	0.239	0.230	0.054	0.012	0.170	0.295	1.000	
40	423.95	319.3	36.7	51.35	389.76	226.67	1447.73	
normalized	0.293	0.221	0.025	0.035	0.269	0.157	1.000	
divided by #H	0.033	0.037	0.013	0.018	0.027	0.052	0.179	
normalized intensity	0.182	0.206	0.071	0.099	0.151	0.292	1.000	
50	310.04	115.14	1	1.18	371.87	80.39	879.62	
normalized	0.352	0.131	0.001	0.001	0.423	0.091	1.000	
divided by #H	0.039	0.022	0.001	0.001	0.042	0.030	0.135	
normalized intensity	0.290	0.162	0.004	0.005	0.313	0.226	1.000	
N222(2O2O2)+ (# protons)	2	2	2	4	6	9	3	
mixing time (ms)	H1	H2	H3	H4,5	H6	H7	H8	total intensity
0	1.59	1.33	1.14	0	30.3	43.8	1	79.16
normalized	0.020	0.017	0.014	0.000	0.383	0.553	0.013	1.000
divided by #H	0.010	0.008	0.007	0.000	0.064	0.061	0.004	0.155
normalized intensity	0.065	0.054	0.046	0.000	0.411	0.396	0.027	1.000
10	2.93	2.64	0	0	24.53	32.46	1	63.56
normalized	0.046	0.042	0.000	0.000	0.386	0.511	0.016	1.000
divided by #H	0.023	0.021	0.000	0.000	0.064	0.057	0.005	0.170
normalized intensity	0.135	0.122	0.000	0.000	0.378	0.334	0.031	1.000
20	18.61	8.08	1	0	105.44	164.11	4.65	301.89
normalized	0.062	0.027	0.003	0.000	0.349	0.544	0.015	1.000
divided by #H	0.031	0.013	0.002	0.000	0.058	0.060	0.005	0.170
normalized intensity	0.182	0.079	0.010	0.000	0.343	0.356	0.030	1.000
30	25.01	18.97	1	0	211.27	460.79	16.32	733.36
normalized	0.034	0.026	0.001	0.000	0.288	0.628	0.022	1.000
divided by #H	0.017	0.013	0.001	0.000	0.048	0.070	0.007	0.156
normalized intensity	0.109	0.083	0.004	0.000	0.308	0.448	0.048	1.000
40	1.03	2.48	1	0	13.75	27.11	2.36	47.73
normalized	0.022	0.052	0.021	0.000	0.288	0.568	0.049	1.000
divided by #H	0.011	0.026	0.010	0.000	0.048	0.063	0.016	0.175
normalized intensity	0.062	0.149	0.060	0.000	0.275	0.361	0.094	1.000
50	1	2.43	2.59	0	42.97	96.42	2.55	147.96
normalized	0.007	0.016	0.018	0.000	0.290	0.652	0.017	1.000
divided by #H	0.003	0.008	0.009	0.000	0.048	0.072	0.006	0.147
normalized intensity	0.023	0.056	0.060	0.000	0.329	0.493	0.039	1.000

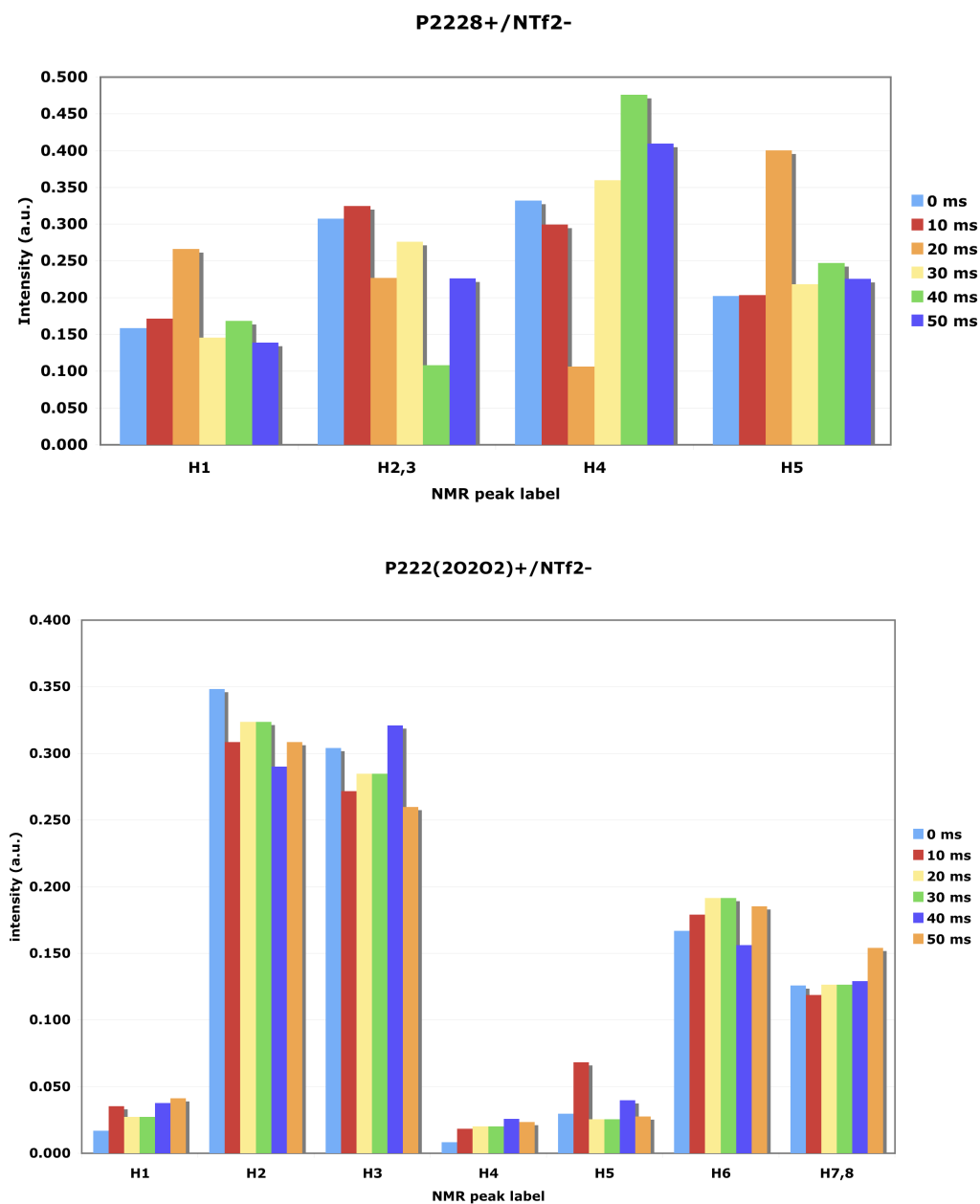


Figure 3.18: Histogram of intensity of each representative proton peak from ^1H NMR at each mixing time (indicated by different colors) for $\text{P}_{2228}^+/\text{NTf}_2^-$ (top) and $\text{P}_{222(2\text{O}_2\text{O}_2)}^+/\text{NTf}_2^-$ (bottom).

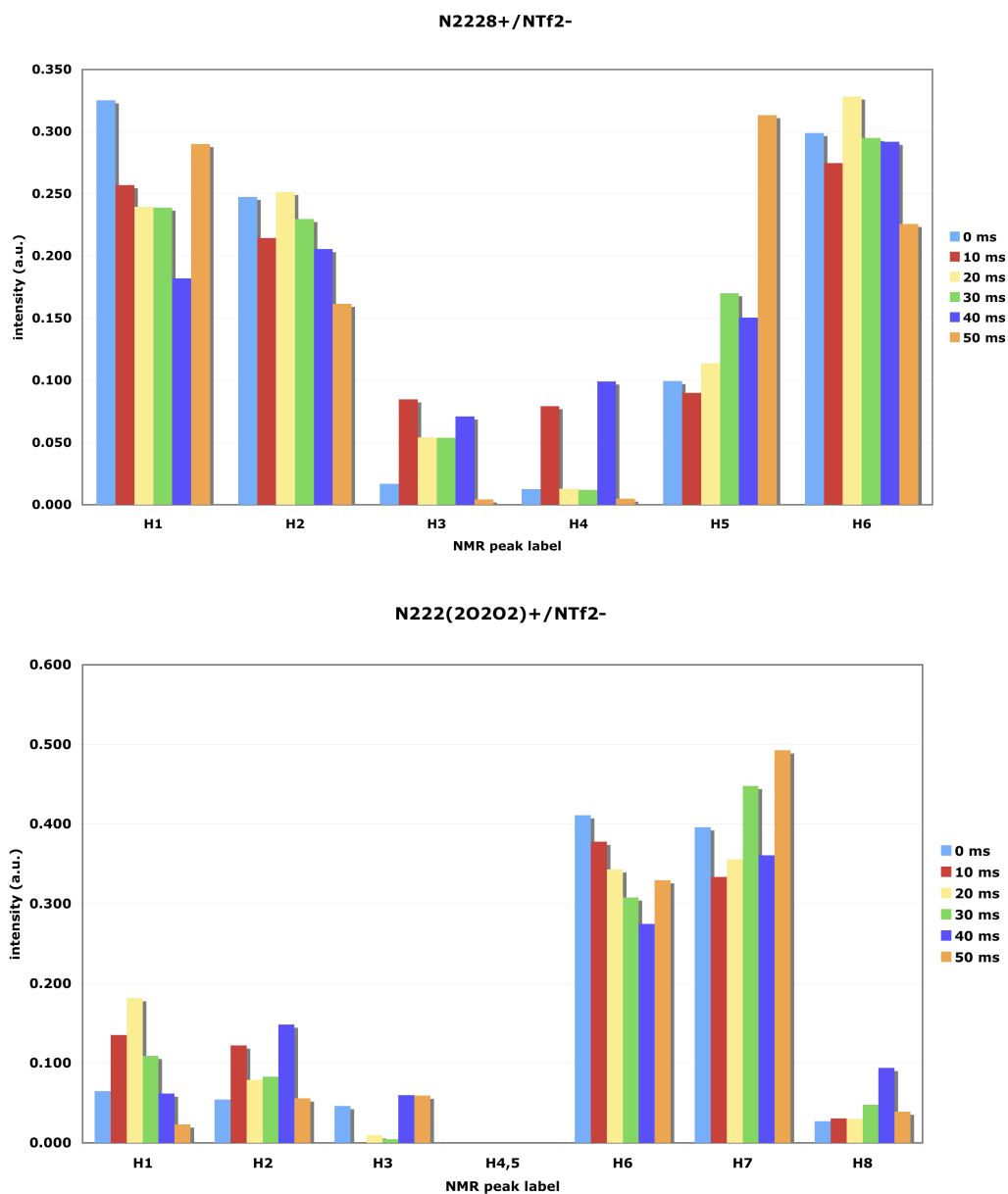


Figure 3.19: Histogram of intensity of each representative proton peak from ^1H NMR at each mixing time (indicated by different colors) for $\text{N}_{2228}^+/\text{NTf}_2^-$ (top) and $\text{N}_{222(2\text{O}_2\text{O}_2)}^+/\text{NTf}_2^-$ (bottom).

The 2D $\{^{19}\text{F}-^1\text{H}\}$ -HOESY spectra of $\text{P}_{2228}^+/\text{NTf}_2^-$ and $\text{P}_{222(2\text{O}2\text{O}2)}^+/\text{NTf}_2^-$ are shown in Figure 3.13 and 3.14, respectively. ^1H is the observed F2 nucleus and ^{19}F is the irradiated F1 nucleus. Because of the nature of HOESY experiments, which suffer from dephasing and incomplete coherence transfer, most of the spectral lines are broadened.^{35,36} Therefore, the 1D ^1H spectra are overlaid above each corresponding 2D HOESY spectrum aligned with the F2 axis for clarity. The protons in the cations are labeled for the sake of the analysis.

Examining the $\{^{19}\text{F}-^1\text{H}\}$ -HOESY spectra of $\text{P}_{2228}^+/\text{NTf}_2^-$, the strongest NOE signal occurs for the terminal methyl ^1H atoms on the octyl chains (H4) of the P_{2228}^+ cations and the ^{19}F atoms on the NTf_2^- anion. This particular cross-peak also increases with increased t_m , achieving its maximum at 40 ms. This shows that there is on average structural correlations on the ms timescale since the coherence transfer between the ^{19}F nuclei and the terminal methyl ^1H nuclei of the octyl chains increases over time. The methyl protons on the ethyl group (H2) of the cations also give NOE signals with the ^{19}F nuclei on the NTf_2^- anions, though not significantly. We note that the NMR peaks for the ^1H atoms located in the middle of the octyl chains (H5) and for the methyl ^1H atoms of the ethyl group (H1) are not well resolved in the 2D $\{^{19}\text{F}-^1\text{H}\}$ -HOESY spectra. However, we speculate that it is more likely that the cross-peak shown for H1/H5 atoms with the ^{19}F atoms does not arise from the H5- ^{19}F interactions but from the H1- ^{19}F interactions because the H1 atoms are closer to the positively charged phosphonium cation head, resulting more probabilities for the anions due to Coulombic charge ordering.

For $\text{P}_{222(2\text{O}2\text{O}2)}^+/\text{NTf}_2^-$, a different structural ordering is observed. Strong interactions are observed for the ^1H atoms located in between the two oxygens of the ether chains (H2 and H3) on the $\text{P}_{222(2\text{O}2\text{O}2)}^+$ cation with the ^{19}F atoms on the NTf_2^- anion. The evidence for this is the strong cross-peak intensities for the heteronuclear NOE signal observed for the H2 and H3 proton nuclei of the cations with the ^{19}F atoms of the anion that is significantly stronger than the NOE signal intensities rising from the terminal methyl ^1H atoms on the ether chains (H8) or the ethyl groups (H7) of the $\text{P}_{222(2\text{O}2\text{O}2)}^+$ cation interacting with the ^{19}F atoms on the NTf_2^- anion. This suggests

very close proximity of the ^{19}F atoms of the NTf_2^- anions to the middle of the ether chains of the $\text{P}_{222}(\text{2O2O2})^+$ cation, especially to the ^1H atoms bridging the two oxygen atoms (H2 and H3 protons). While the terminal methyl protons are expected to give strong cross-peaks with the ^{19}F atoms on the NTf_2^- anion based on the results demonstrated by $\text{P}_{2228}^+/\text{NTf}_2^-$, the fact that the ^1H atoms in the middle of the long ether chains produce the most intense cross-peak with the ^{19}F atoms of the anions is unexpected and surprising. When the normalized effective integration values of the $\{^{19}\text{F}-^1\text{H}\}$ -HOESY intensities are considered, the H2 and H3 protons give heteronuclear NOE signals that are more than ten times intense than that for the H4 protons of the same cation.

We also measured $\{^{31}\text{P}-^{19}\text{F}\}$ -HOESY and $\{^{31}\text{P}-^1\text{H}\}$ -HOESY spectra for the investigation of the ^{31}P nuclei interactions with the ^{19}F and ^1H nuclei of the phosphonium ILs. The ^{31}P peak was observed at 37.7 ppm for $\text{P}_{222}(\text{2O2O2})^+/\text{NTf}_2^-$ and at 39.3 ppm for $\text{P}_{2228}^+/\text{NTf}_2^-$. ^1H is the observed F2 nucleus and ^{31}P is the irradiated F1 nucleus. The HOESY experiments between the ^{31}P nuclei of the phosphonium cations with either the ^1H nuclei of the cation or ^{19}F nuclei of the anion were not illuminating. No cross-peaks between ^{31}P nuclei and ^{19}F nuclei were observed; $\{^{31}\text{P}-^1\text{H}\}$ peaks revealed only intramolecular correlations between the covalently linked protons to the phosphonium atom. The $\{^{19}\text{F}-^{31}\text{P}\}$ -HOESY spectrum of $\text{P}_{222}(\text{2O2O2})^+/\text{NTf}_2^-$ is shown in Figure 3.17.

The 2D $\{^{19}\text{F}-^1\text{H}\}$ -HOESY spectra of $\text{N}_{2228}^+/\text{NTf}_2^-$ and $\text{N}_{222}(\text{2O2O2})^+/\text{NTf}_2^-$ are shown in Figure 3.15 and 3.16. On inspection of $\text{N}_{2228}^+/\text{NTf}_2^-$ spectra, we find that the strongest cross-peak exists for the terminal methyl protons of the octyl chain on the cation (H6) with the ^{19}F atoms on the anion. Although the cross-peak for the protons in the middle of the octyl chain (H5) seem to be giving a significant NOE signal with the ^{19}F atoms on the anion just based on the figure, the normalized intensities per atom show that that is not the case. The protons on the ethyl group (H1 and H2) of the cation give stronger NOE signal with the ^{19}F atom of the anion than the H5 protons. The H4 and H3 protons on the N_{2228}^+ cation do not display any significant cross-peaks with the ^{19}F atoms on the NTf_2^- anion as was the case for $\text{P}_{2228}^+/\text{NTf}_2^-$.

For $N_{222(2O_2O_2)}^+/NTf_2^-$, the differences in the intensities of the cross-peaks are more obvious. The methyl protons of the ethyl group of the $N_{222(2O_2O_2)}^+$ cation (H7) give rise to very strong heteronuclear NOE signal with the ^{19}F atoms on the NTf_2^- anion, compared to other protons on the cation. This suggests that the anions are closer to the polar heads of the ammonium cations rather than to the ether chains, which is the case for $P_{222(2O_2O_2)}^+/NTf_2^-$. Another aspect of these $\{^{19}F-^1H\}$ -HOESY spectra for the $N_{222(2O_2O_2)}^+/NTf_2^-$ IL is the negligible NOE signals between the H4 protons with the ^{19}F atoms and the H5 protons with the ^{19}F atoms of the NTf_2^- anion. Similar results were shown for the $P_{222(2O_2O_2)}^+/NTf_2^-$ IL where the protons at the same location on the cation had very low (almost negligible) intensity NOE signals with the ^{19}F atoms on the NTf_2^- anion. This result shows that even though the ^{19}F atoms on the NTf_2^- might be in proximity of some of the protons on the ether chains, the ions are ordered in such way that ^{19}F nuclei give rise to NOE to selective protons on the ether chains of the cations, such as those located in between the two oxygens. This requires that we consider the effective charges on these atoms, and to address the question of whether the interactions between H2 and H3 with the ^{19}F atoms on NTf_2^- anions can be described as hydrogen bonds.

3.3.2 Results from the Electronic Structure Calculations on the Cations

The results obtained from the fits of the electrostatic potential for the atom-centered charges, the CHelpG algorithm applied to B3LYP/6-31+G(d,p) level geometry optimized molecules, are given in Table 3.3. The lowest energy conformations of the four ILs are shown in Figures 3.20, 3.21, 3.22 and 3.23. The values of the charges calculated from the fits of the electrostatic potential to atom-centered charges, using the CHelpG algorithm⁴⁶ are shown for each of the atoms. Although the initial dihedral angles for carbons 5-6-7-8 (or C5-O6-C7-C8 for the ether chains) were varied, all of the cations with octyl chains optimized at 66° and the ether chained ILs optimized at 92° for the chain dihedral angles between the atoms 5-6-7-8.

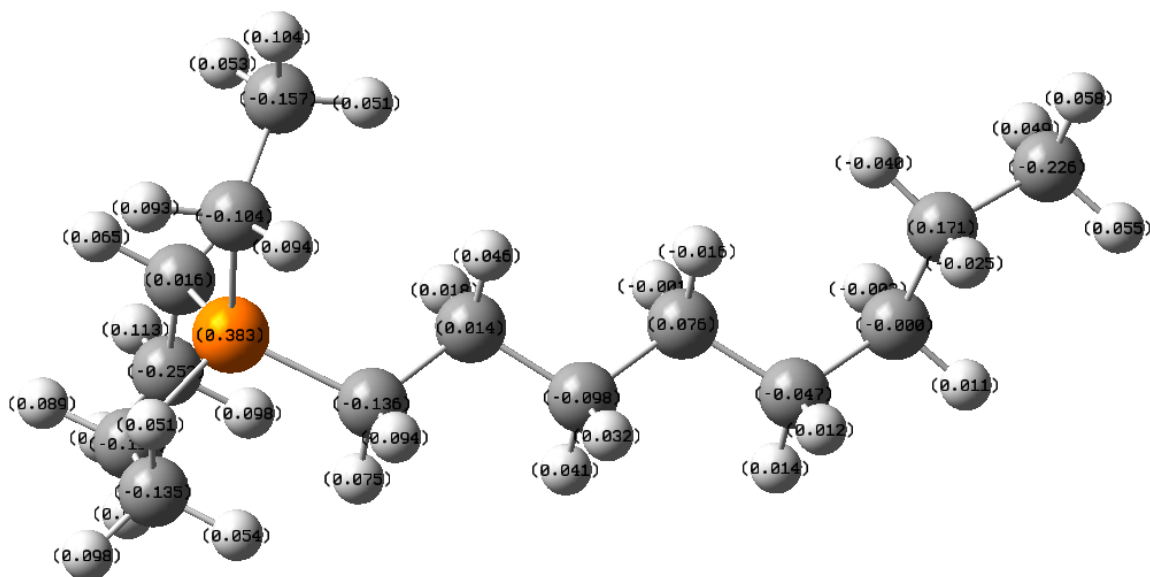


Figure 3.20: Optimized geometry of P_{2228}^+/NTf_2^- using in B3LYP/6-31+G(d,p) level in gas phase with the electrostatic potential charges calculated using the CHelpG algorithm.

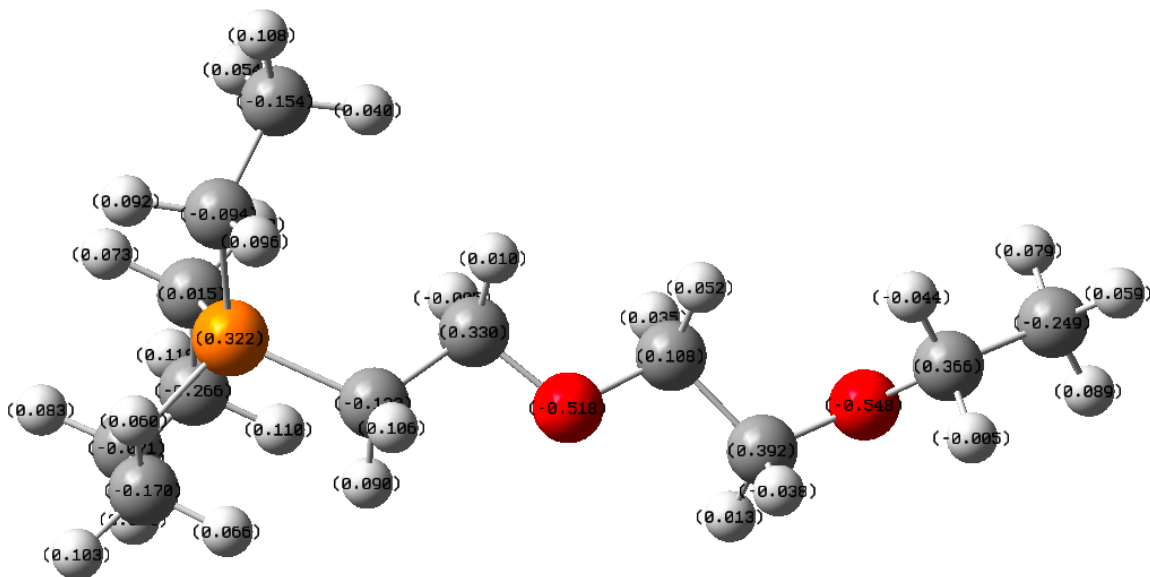


Figure 3.21: Optimized geometry of $P_{222(2O_2O_2)}^+/NTf_2^-$ using in B3LYP/6-31+G(d,p) level in gas phase with the electrostatic potential charges calculated using the CHelpG algorithm.

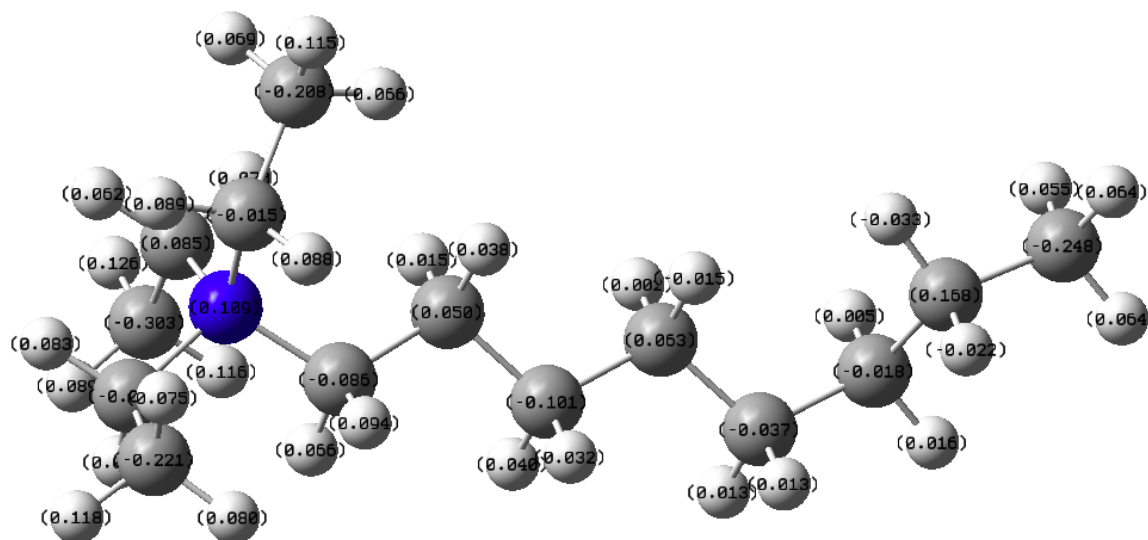


Figure 3.22: Optimized geometry of $\text{N}_{222\text{s}}^+/\text{NTf}_2^-$ using in B3LYP/6-31+G(d,p) level in gas phase with the electrostatic potential charges calculated using the CHelpG algorithm.

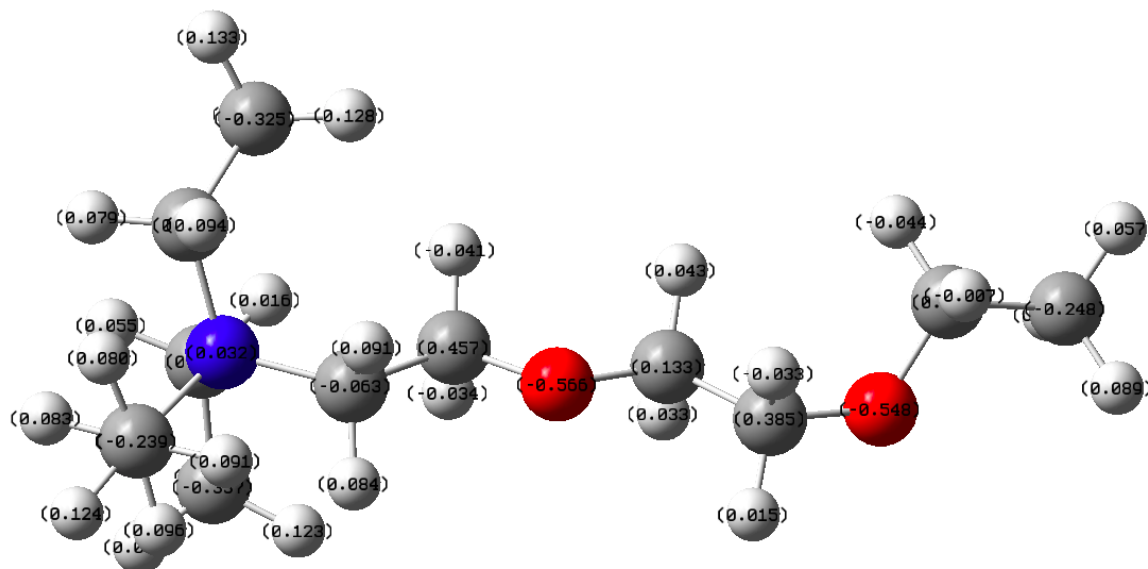


Figure 3.23: Optimized geometry of $\text{N}_{222(2\text{O}_2\text{O}_2)}^+/\text{NTf}_2^-$ using in B3LYP/6-31+G(d,p) level in gas phase with the electrostatic potential charges calculated using the CHelpG algorithm.

Table 3.3: Charges calculated from fits of the electrostatic potential to atom-centered charges, using the CHelpG algorithm⁴⁶ of the four cations, P_{2228}^+ , $P_{222(2O2O2)}^+$, N_{2228}^+ , and $N_{222(2O2O2)}^+$ optimized in *trans-gauche* geometry in gas phase.

	P2228	P222(2O2O2)	N2228	N222(2O2O2)
P1 / N1	0.383	0.322	0.109	0.032
C1	-0.136	-0.132	-0.086	-0.063
H1a	0.075	0.09	0.066	0.084
H1b	0.094	0.106	0.094	0.091
C2	0.014	0.33	0.05	0.457
H2a	0.018	-0.005	0.015	-0.034
H2b	0.046	0.01	0.038	-0.041
C3 / O3	-0.098	-0.518	-0.101	-0.566
H3a	0.041		0.04	
H3b	0.032		0.032	
C4	0.076	0.108	0.063	0.133
H4a	-0.001	0.035	0.002	0.033
H4b	-0.016	0.052	-0.015	0.043
C4	-0.047	0.392	-0.037	0.385
H5a	0.014	0.013	0.013	0.015
H5b	0.012	-0.038	0.013	-0.033
C6 / O6	0	-0.548	-0.018	-0.548
H6a	-0.002		0.005	
H6b	0.011		0.016	
C7 / O7	0.171	0.366	0.168	0.367
H7a	-0.04	-0.005	-0.033	-0.007
H7b	-0.025	-0.044	-0.022	-0.044
C8	-0.226	-0.249	-0.248	-0.248
H8a	0.049	0.089	0.055	0.08
H8b	0.058	0.079	0.064	0.089
H8c	0.055	0.059	0.064	0.057
SUM(chain)	0.175	0.19	0.238	0.25
C1'	-0.104	0.015	-0.015	0.034
H1'a	0.094	0.06	0.088	0.094
H1'b	0.093	0.073	0.089	0.079
C2'	-0.157	-0.266	-0.208	-0.325
H2'a	0.051	0.11	0.066	0.128
H2'b	0.053	0.075	0.069	0.102
H2'c	0.104	0.118	0.115	0.133
SUM(ethyl1)	0.134	0.185	0.204	0.245
C1''	0.016	-0.071	0.085	0.161
H1''a	0.063	0.091	0.07	0.016
H1''b	0.065	0.083	0.062	0.055
C2''	-0.252	-0.17	-0.303	-0.337
H2''a	0.098	0.066	0.116	0.123
H2''b	0.113	0.103	0.126	0.136
H2''c	0.072	0.06	0.089	0.094
SUM(ethyl2)	0.175	0.162	0.245	0.248
C1'''	-0.119	-0.094	-0.025	-0.011
H1'''a	0.095	0.096	0.097	0.096
H1'''b	0.089	0.092	0.083	0.083
C2'''	-0.135	-0.154	-0.221	-0.239
H2'''a	0.051	0.04	0.08	0.091
H2'''b	0.098	0.054	0.118	0.124
H2'''c	0.054	0.108	0.075	0.08
SUM(ethyl3)	0.133	0.142	0.207	0.224
SUM(ethyls+ P or N)	0.825	0.811	0.765	0.749
Sum(total)	1	1.001	1.003	0.999
E (HF)	-894.1245778	-965.9294275	-607.46899	-679.2724846

3.3.3 X-ray Scattering Results

The x-ray scattering data were measured at the Advanced Photon Source (APS) beam line 11-ID-C at Argonne National Laboratory directed by Dr. Benmore and Dr. Ren.⁴⁷ The data described in this study were taken by Dr. Cherry Santos, Dr. N. Sanjeeva Murthy, Matthew Sasso, and Prof. Edward W. Castner, Jr. Details on the experimental setup and the fitting method used are described by Santos, *et al.*⁴ The structure function $S(q)$ is shown in Figure 3.24. The $I(q)$ from which $S(q)$ is calculated shows the same range of scattering vectors as reported previously.⁶ The FSDP near 0.4 \AA^{-1} is apparent for the two ionic liquids with octyl-chain cations though it is absent for the isoelectric 2-ethoxyethoxyethyl homolog.

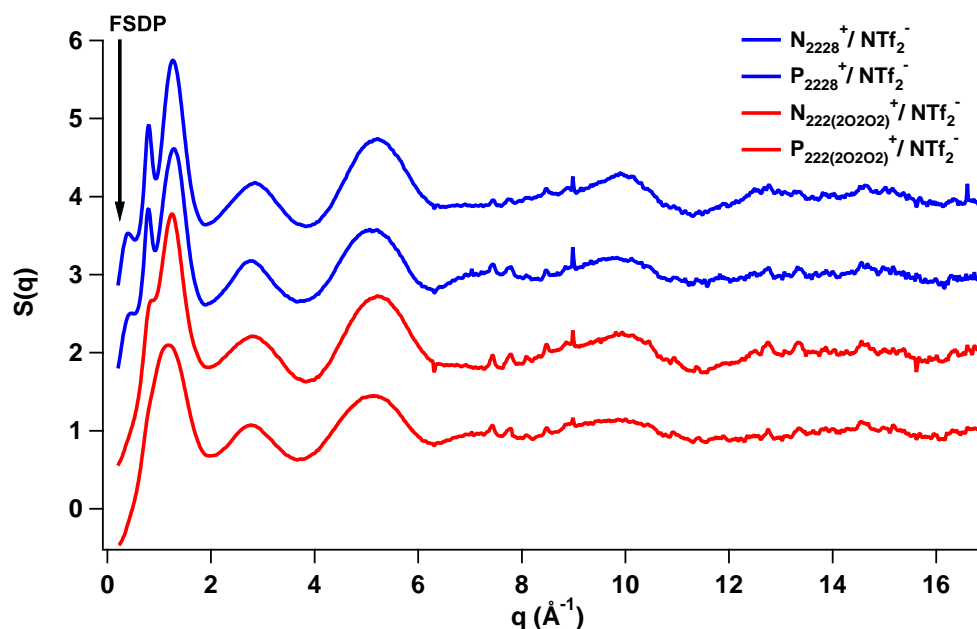


Figure 3.24: Structure function $S(q)$ calculated from $I(q)$, which is published previously.⁶ Structure functions of N_{2228}^{+} and P_{2228}^{+} in blue, $N_{222(2O2O2)}^{+}$ and $P_{222(2O2O2)}^{+}$ in red at 295 K. $S(q)$ is plotted for q from 0.2 to 17 \AA^{-1} . The curves are offset by 1.0 vertical units for N_{2228}^{+} , P_{2228}^{+} , and $N_{222(2O2O2)}^{+}$. Data measured at beamline 11-ID-C at the Advanced Photon Source. Thanks to Dr.Santos for calculating $I(q)$ and $S(q)$.

3.4 Discussion

The presence of a FSDP is a manifestation nanoscale ordering for these ILs, appearing as a peak in the x-ray or neutron structure factor in the range from 0.2 to 0.6 \AA^{-1} .^{4,5} We have previously reported the x-ray scattering intensities for $\text{P}_{2228}^{+}/\text{NTf}_2^{-}$, $\text{P}_{222(2\text{O}_2\text{O}_2)}^{+}/\text{NTf}_2^{-}$, $\text{N}_{2228}^{+}/\text{NTf}_2^{-}$, and $\text{N}_{222(2\text{O}_2\text{O}_2)}^{+}/\text{NTf}_2^{-}$. In Figure 2 of the previously published work by Triolo, *et al.*,⁶ the scattering vector near 0.4 \AA^{-1} was apparent for the ILs with octyl chains. For the pair of isoelectronic ether-substituted ILs, $\text{P}_{222(2\text{O}_2\text{O}_2)}^{+}$ and $\text{N}_{222(2\text{O}_2\text{O}_2)}^{+}$, no FSDPs are observed in the structure functions.

Comparing the results from the x-ray scattering with those from the 2D HOESY measurements may reveal possible structural ordering differences for the four ILs studied. One of the major differences we observed between the P_{2228}^{+} and $\text{P}_{222(2\text{O}_2\text{O}_2)}^{+}$ cation based ILs was the presence of the strong ^{19}F - ^1H cross-peaks of the ^1H atoms located between the ether oxygen atoms of the $\text{P}_{222(2\text{O}_2\text{O}_2)}^{+}$ cations relative to the weak cross-peaks of the ^1H protons on the octyl chains of P_{2228}^{+} cations. In addition, the existence of the cross-peaks for the ^1H protons on the terminal methyl of the octyl chain and the ethyl group of the N_{2228}^{+} cation with the ^{19}F atoms on the NTf_2^{-} anion support the idea that the anion-cation interaction exists near the polar heads and the end of the octyl tail. Additionally, the normalized intensities per atom for the NOE signals show that the anions are more evenly distributed around the cations for the alkyl substituted cation containing ILs; while the anions are significantly concentrated in certain areas of the cations (e.g. near the ethers for $\text{P}_{222(2\text{O}_2\text{O}_2)}^{+}$ and near the ethyl group for $\text{N}_{222(2\text{O}_2\text{O}_2)}^{+}$).

The difference between the octyl vs. ether chains is polarity and chain conformation. The possible explanation for such differences between the ILs with octyl and ether chain cations, especially for the phosphonium ILs, is the presence of electronegative oxygen groups effecting the nearby protons to be slightly more acidic than other protons. The proposed structural ordering for these ILs is as follows: the scattering vector near 0.4 \AA^{-1} that is only present for the ILs with octyl chain cations may indicate cation-cation tail segregation that does not exist in the ILs with the ether chain cations because

of the proximity of the anions near the center of the ethoxy groups. Computational studies by Kashyap, *et al.*[?] also support this hypothesis, where the probability density of the NTf_2^- anions is higher around the ether chain of the $\text{P}_{222(2\text{O}_2\text{O}_2)}^+$ cation than around the octyl chain of the P_{2228}^+ cation. The molecular level structural ordering proposed for the ether tail containing ILs is also different for ILs with imidazolium or pyrrolidinium ring cations.^{23,26} For both imidazolium and pyrrolidinium ring based ILs, the ^{19}F atoms of the anions were found to have long-lived associations with the protons on either the imidazolium or the pyrrolidinium rings.^{23,26} The phosphonium and ammonium ILs studied here also show similar ^{19}F nuclei to ^1H nuclei (near the polar head) structural ordering for the cations with nonpolar octyl chains; however, the ^{19}F atoms of the NTf_2^- anion showed selective associations with the ^1H atoms near the ethoxy group on the cations with ether chains. This may suggest that when nonpolar chains are substituted by polar components, the cation-anion intermolecular structural ordering of such ILs changes, affecting the macroscopic properties such as viscosity and surface tension.¹⁸

3.5 Conclusions

The two pairs of isoelectronic NTf_2^- anion ILs, $\text{N}_{2228}^+/\text{N}_{222(2\text{O}_2\text{O}_2)}^+$ and $\text{P}_{2228}^+/\text{P}_{222(2\text{O}_2\text{O}_2)}^+$, show significant differences in intermolecular interactions and liquid structure, as evident by differences in results from 2D NMR and X-ray scattering experiments. $\{^{19}\text{F}-^1\text{H}\}$ heteronuclear NOE spectra show that certain ^1H atoms on the cations show strong interactions with the ^{19}F atoms on the NTf_2^- anions. For $\text{P}_{222(2\text{O}_2\text{O}_2)}^+$ cations, protons that produce high intensity cross-peaks with the ^{19}F atoms are located on the methylene group bridging two oxygens on the ether chain. For the P_{2228}^+ cations, the terminal methyl protons on the ethyl group and the terminal methyl protons on the octyl chains display stronger interactions with ^{19}F atoms on the anion than other protons on the cations. These results indicate a different structural ordering for the two pairs of ILs: the ether substituted cations have anions near the tail group while the octyl chain cations prefer anions near the polar head or the end of the octyl chain, leaving the middle of the octyl chain free of anions in proximity. One hypothesis for the

strong interactions between the ^{19}F atoms on the anions with the ^1H atoms bridging the two oxygens in the ether chain of the cations is a possible hydrogen bond interactions between those hydrogen atoms with the oxygens on the sulfonyl group of the anion. A H-bond between the ^1H atoms on the cations and $\text{NTf}_2^- \text{SO}_2$ groups would place ^{19}F atoms of the anions in proximity with the hydrogens bridging the oxygens on the ether chain of the cation, producing a strong HOESY signal.

Previously reported x-ray scattering results on these ILs show that the FSDP that is prominent in certain ILs may come from different sources of interactions depending on the IL analyzed. When ILs with cations containing different alkyl chain length groups are compared, the presence of FSDP was attributed to the segregation of the nonpolar regions. Despite the identical cation chain lengths, polar chain containing ILs exhibit different structural ordering that can be attributed to the change in cation tail polarity. Based on the 2D NMR experiments reported here, anion-cation interaction is governed by the polarity of the tail group, i.e. anions have a stronger affinity for polar tails than nonpolar tails. This current investigation illustrated the complexity of structural ordering in ILs. Structural conformations play an integral role in ion mobility and charge transfer. Small variations in polarity, chain length, and polar head group all play crucial roles in IL structural ordering and must be understood before ILs become the standard medium for electron transfer media. We anticipate that a combination of X-ray or neutron scattering experiments, molecular simulations, and 2D NMR NOE experiments will be required to fully determine the interactions between the molecular ions and the overall bulk structure of ILs.

Bibliography

- [1] H. V. R. Annapureddy, H. K. Kashyap, P. M. D. Biase, and C. J. Margulis. What is the origin of the prepeak in the x-ray scattering of imidazolium-based room-temperature ionic liquids? *J. Phys. Chem. B*, 114:16838, 2010.
- [2] H. K. Kashyap, J. J. Hettige, H. V. R. Annapureddy, and C. J. Margulis. Saxs anti-peaks reveal the length-scales of dual positive-negative and polar-apolar ordering in room-temperature ionic liquids. *Chem. Comm.*, 48:5103–5105, 2012.
- [3] H. K. Kashyap, C. S. Santos, H. V. R. Annapureddy, N. S. Murthy, C. J. Margulis, and E. W. Castner, Jr. Temperature-dependent structure of ionic liquids: X-ray scattering and simulations. *Faraday Discuss.*, 154:133–143, 2012.
- [4] C. S. Santos, N. S. Murthy, G. A. Baker, and E. W. Castner, Jr. X-ray scattering from ionic liquids with pyrrolidinium cations. *J. Chem. Phys.*, 134:121101, 2011.
- [5] A. Triolo, O. Russina, H.-J. Bleif, and E. Di Cola. Nanoscale segregation in room temperature ionic liquids. *J. Phys. Chem. B*, 111:4641–4644, 2007.
- [6] A. Triolo, O. Russina, R. Caminiti, H. Shirota, H. Y. Lee, C. S. Santos, N. S. Murthy, and E. W. Castner, Jr. Comparing intermediate range order for alkyl- vs. ether-substituted cations in ionic liquids. *Chem. Comm.*, 48:4959–4961, 2012.
- [7] A. Triolo, O. Russina, B. Fazio, R. Triolo, and E. DiCola. Morphology of 1-alkyl-3-methylimidazolium hexafluorophosphate room temperature ionic liquids. *Chem. Phys. Lett.*, 457:362–365, 2008.
- [8] O. Russina, A. Triolo, L. Gontrani, R. Caminiti, D. Xiao, L. G. Hines, Jr., R. A. Bartsch, E. L. Quitevis, N. Pleckhova, and K. R. Seddon. Morphology and intermolecular dynamics of 1-alkyl-3-methylimidazolium

- bis(trifluoromethane)sulfonylamide ionic liquids: structural and dynamic evidence of nanoscale segregation. *J. Phys. Condens. Matter*, 21:424121, 2009.
- [9] C. Hardacre, J. D. Holbrey, S. E. J. McMath, D. T. Bowron, and A. K. Soper. Structure of molten 1,3-dimethylimidazolium chloride using neutron diffraction. *J. Chem. Phys.*, 118:273–278, 2003.
- [10] M. G. Del Popolo and G. A. Voth. On the structure and dynamics of ionic liquids. *J. Phys. Chem. B*, 108:1744–1752, 2004.
- [11] J. N. Canongia Lopes and A. A. H. Padua. Nanostructural organization in ionic liquids. *J. Phys. Chem. B*, 110:3330–3335, 2006.
- [12] Y. T. Wang, S. Izvekov, T. Y. Yan, and G. A. Voth. Multiscale coarse-graining of ionic liquids. *J. Phys. Chem. B*, 110:3564–3575, 2006.
- [13] Y. T. Wang and G. A. Voth. Unique spatial heterogeneity in ionic liquids. *J. Am. Chem. Soc.*, 127:12192–12193, 2005.
- [14] A. A. H. Pádua, M. F. Costa Gomes, and J. N. A. Canongia Lopes. Molecular-solutes in ionic liquids: A structural perspective. *Acc. Chem. Res.*, 40:1087–1096, 2007.
- [15] S. M. Urahata and M. C. C. Ribeiro. Structure of ionic liquids of 1-alkyl-3-methylimidazolium cations: A systematic computer simulation study. *J. Chem. Phys.*, 120:1855–1863, 2004.
- [16] H. Shirota and E. W. Castner, Jr. Physical properties and intermolecular dynamics of an ionic liquid compared with its isoelectronic neutral binary solution. *J. Phys. Chem. A*, 109:9388–9392, 2005.
- [17] O. Russina and A. Triolo. New experimental evidence supporting the mesoscopic segregation model in room temperature ionic liquids. *Faraday Discuss.*, 154:97–109, 2012.

- [18] H. Shirota, H. Fukazawa, T. Fujisawa, and J. F. Wishart. Heavy atom substitution effects in non-aromatic ionic liquids: Ultrafast dynamics and physical properties. *J. Phys. Chem. B*, 114:9400–9412, 2010.
- [19] H. Shirota and E. W. Castner Jr. Why are viscosities lower for ionic liquids with $\text{CH}_2\text{Si}(\text{CH}_3)_3$ vs. $\text{CH}_2\text{C}(\text{CH}_3)_3$ substitutions on the imidazolium cations? *J. Phys. Chem. B*, 109:21576–21585, 2005.
- [20] H. Shirota, J. F. Wishart, and E. W. Castner. Intermolecular interactions and dynamics of room temperature ionic liquids that have silyl- and siloxy-substituted imidazolium cations?. *J. Phys. Chem. B*, 111:4819–4829, 2007.
- [21] R. A. Mantz, P. C. Trulove, R. T. Carlin, and R. A. Osteryoung. ROESY NMR of basic ambient-temperature chloroaluminate ionic liquids. *Inorg. Chem.*, 34:3846–3847, 1995.
- [22] P. J. Dupont, A. Z. Suarez, R. F. De Souza, R. A. Burrow, and J. P. Kintzinger. C–H- π interactions in 1-n-butyl-3-methylimidazolium tetraphenylborate molten salt: Solid and solution structures. *Chem. Eur. J.*, 6:2377–2381, 2000.
- [23] A. Mele, C. D. Tran, and S. H. D. Lacerda. The structure of a room-temperature ionic liquid with and without trace amounts of water: The role of C–H center dot center dot center dot O and C–H center dot center dot center dot F interactions in 1-n-butyl-3-methylimidazolium tetrafluoroborate. *Angew. Chem., Int. Ed.*, 42:4364–4366, 2003.
- [24] D. Nama, P. G. A. Kumar, P. S. Pregosin, T. J. Geldbach, and P. J. Dyson. H-1, F-19-HOESY and PGSE diffusion studies on ionic liquids: The effect of co-solvent on structure. *Inorg. Chem. Acta*, 359:1907–1911, 2006.
- [25] N. E. Heimer, R. E. Desl Sesto, and R. Carper. Evidence for spin diffusion in a H,H-NOESY study of imidazolium tetrafluoroborate ionic liquids. *Magn. Reson. Chem.*, 42:71–75, 2004.

- [26] F. Castiglione, M. Moreno, G. Raos, A. Famulari, A. Mele, G. B. Appetecchi, and S. Passerini. Structural organization and transport properties of novel pyrrolidinium-based ionic liquids with perfluoroalkyl sulfonylimide anions. *J. Phys. Chem. B*, 113:10750–10759, 2009.
- [27] Andrea Mele. Noe experiments for ionic liquids- tools and strategies. *chimica oggi/Chemistry Today*, 28:48–55, 2010.
- [28] H. Kessler, M. Gehrke, and C. Griesinger. Two-dimensional NMR spectroscopy: Background and overview of the experiments. *Angew. Chem. Int. Ed. Engl.*, 27:490–536, 1988.
- [29] W. P. Aue, E. Bartholdi, and R. R. Ernst. Two-dimensional spectroscopy. Application to nuclear magnetic resonance. *J. Chem. Phys.*, 64:2229–2246, 1976.
- [30] J. B. Lambert and E. P. Mazzola. *Nuclear Magnetic Resonance Spectroscopy - An Introduction to principles, applications, and experimental methods*. Pearson Education, Inc., 2004.
- [31] D. Neuhaus and M. P. Williamson. *The Nuclear Overhauser Effect in Structural and Conformational Analysis*. Wiley VCH, New York, 2000.
- [32] P. L. Rinaldi and N. J. Baldwin. Carbon-13 deuteron polarization transfer studies: new NMR methods for isotropic labeling studies. *J. Am. Chem. Soc.*, 105:5167, 1983.
- [33] C. Yu and G. C. Levy. Solvent and intramolecular proton dipolar relaxation of the three phosphates of ATP: a heteronuclear 2D NOE study. *J. Am. Chem. Soc.*, 105:6994, 1983.
- [34] C. Yu and G. C. Levy. Intramolecular proton exchange in 9-hydroxyphenalen-1-one and methyl-9-hydroxyphenalen-1-one. *J. Am. Chem. Soc.*, 106:6533, 1984.
- [35] W. Bauer. Pulse field gradient ‘inverse’ hoesy applied to the isotope pairs H-1, P-31 and H-1, Li-7. *Magn. Reson. Chem.*, 34:532, 1996.

- [36] T. M. Alam, D. M. Pedrotty, and T. Boyle. Modified, pulse field gradient-enhanced inverse-detected hoesy pulse sequence for reduction of t1 spectral artifacts. *Magn. Reson. Chem.*, 40:361–365, 2002.
- [37] M. N. Kobrak. The chemical environment of ionic liquids: Links between liquid structure, dynamics, and solvation. In Stuart A. Rice, editor, *Adv. Chem. Phys., Volume 139*, chapter 2, pages 85–137. John Wiley and Sons, New York, 2008.
- [38] K. R. Seddon, A. Stark, and M. J. Torres. Influence of chloride, water, and organic solvents on the physical properties of ionic liquids. *Pure Appl. Chem.*, 72:2275–2287, 2000.
- [39] J. P. Hallett and T. Welton. Room-temperature ionic liquids: Solvents for synthesis and catalysis. 2. *Chem. Rev.*, 111:3508–3576, 2011.
- [40] H. Shirota and E. W. Castner Jr. Solvation in highly nonideal solutions: A study of aqueous 1-propanol using the coumarin 153 probe. *J. Chem. Phys.*, 112:2367–2376, 2000.
- [41] Mestrenova. version 7.1.0, Mestrelab Research SLMestrenova.
- [42] J. N. Canongia Lopes and A. A. H. Padua. Molecular force field for ionic liquids composed of triflate or bistriflylimide anions. *J. Phys. Chem. B.*, 108:16893–16898, 2004.
- [43] M. J. Frisch, G. W. Trucks, H. B. Schlegel, G. E. Scuseria, M. A. Robb, J. R. Cheeseman, Jr. Montgomery, J. A., T. Vreven, K. N. Kudin, J. C. Burant, J. M. Millam, S. S. Iyengar, J. Tomasi, V. Barone, B. Mennucci, M. Cossi, G. Scalmani, N. Rega, G. A. Petersson, H. Nakatsuji, M. Hada, M. Ehara, K. Toyota, R. Fukuda, J. Hasegawa, M. Ishida, T. Nakajima, Y. Honda, O. Kitao, H. Nakai, M. Klene, X. Li, J. E. Knox, H. P. Hratchian, J. B. Cross, C. Adamo, J. Jaramillo, R. Gomperts, R. E. Stratmann, O. Yazyev, A. J. Austin, R. Cammi, C. Pomelli, J. W. Ochterski, P. Y. Ayala, K. Morokuma, G. A. Voth, P. Salvador, J. J. Dannenberg, V. G. Zakrzewski, S. Dapprich, A. D. Daniels, M. C. Strain, O. Farkas, D. K. Malick, A. D. Rabuck, K. Raghavachari, J. B. Foresman, J. V. Ortiz, Q. Cui, A. G.

- Baboul, S. Clifford, J. Cioslowski, B. B. Stefanov, G. Liu, A. Liashenko, P. Piskorz, I. Komaromi, R. L. Martin, D. J. Fox, T. Keith, M. A. Al-Laham, C. Y. Peng, A. Nanayakkara, M. Challacombe, P. M. W. Gill, B. Johnson, W. Chen, M. W. Wong, C. Gonzalez, and J. A. Pople. *GAUSSIAN 09, Revision A.1*. Gaussian, Inc., Wallingford, CT, 2009.
- [44] A.l D. Becke. Density-functional thermochemistry. iii. the role of exact exchange. *J. Chem. Phys.*, 98:5648–5652, 1993.
- [45] G. A. Petersson, A. Bennett, T. G. Tensfeldt, M. A. Al-Laham, W. A. Shirley, and J. Mantzaris. A complete basis set model chemistry. I. The total energies of closed-shell atoms and hydrides of the first-row atoms. *J. Chem. Phys.*, 89:2193–2218, 1988.
- [46] C.t M. Breneman and K. B. Wiberg. Determining atom-centered monopoles from molecular electrostatic potentials. the need for high sampling density in formamide conformational analysis. *J. Comp. Chem.*, 11:361–373, 1990.
- [47] Advanced photon source. <http://www.aps.anl.gov/Beamlines/>.

Chapter 4

Ionic Liquids and Solids with Paramagnetic Anions

4.1 Introduction

Magnetic materials fascinate everyone regardless of age. The commonly observable form of magnetic behavior is ferromagnetism, which occurs when the spins of strongly interacting unpaired electrons align parallel to each other, resulting in a permanent magnetic field. In contrast, in a diamagnetic material all the electron spins are paired, and therefore the material has no net magnetic field. Paramagnetic materials contain unpaired electrons that weakly align in the presence of an external magnetic field but lose their alignment once the applied field is removed.

In 2004, Hayashi and Hamaguchi reported¹ the finding of a paramagnetic ferric chloride IL, which reacted to a magnet. Since then, many reports on paramagnetic ILs based on iron containing anions have been published.²⁻⁶ Del Sesto, *et al.* have reported paramagnetic ILs where the cations are paired with tetrahedral or octahedral symmetry transition metal anions.⁷ More recently, the world's first 'magnetic soap'⁸ was reported, which uses iron centered IL surfactants. IL-based materials are a vastly untapped area of research and with such exciting examples as these, continuing research and development in this area is paramount.

Four paramagnetic ionic compounds have been prepared and their magnetic, structural and thermal properties have been investigated.⁹ The four compounds are methylbutylpyrrolidinium tetrachloroferrate(III) ($\text{Pyr}_{14}^+/\text{FeCl}_4^-$), methyltributylammonium tetrachloroferrate(III) ($\text{N}_{1444}^+/\text{FeCl}_4^-$), butylmethylimidazolium tetrachloroferrate(III) ($\text{bmim}^+/\text{FeCl}_4^-$) and tetrabutylammonium bromotrichloroferrate(III) ($\text{N}_{4444}^+/\text{FeBrCl}_3^-$), and their structures are shown in Figure 4.1. Temperature-dependent studies of their

magnetic behaviors show that all four compounds are paramagnetic at ambient temperatures. Glass transitions are observed for only two of the four compounds, $\text{Pyrr}_{14}^+/\text{FeCl}_4^-$ and $\text{bmim}^+/\text{FeCl}_4^-$. Crystallographic data are reported for our two new compounds $\text{Pyrr}_{14}^+/\text{FeCl}_4^-$ and $\text{N}_{1444}^+/\text{FeCl}_4^-$. These structures are compared with the structure of $\text{N}_{4444}^+/\text{FeBrCl}_3^-$ that was reported by Kruszyński and Wyrzykowski.¹⁰

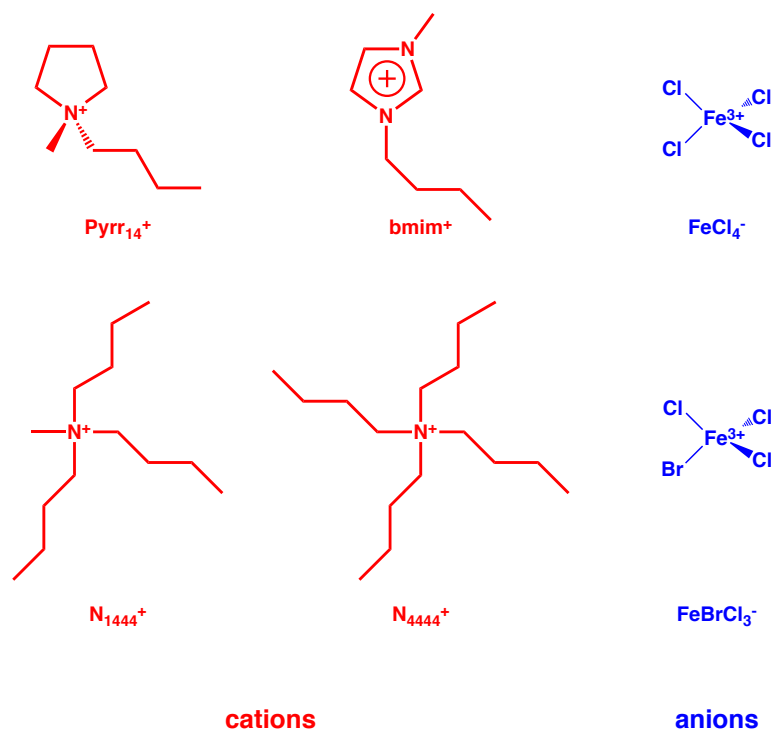


Figure 4.1: Paramagnetic ionic liquids and solids

4.2 Experimental methods

4.2.1 Synthesis

New Ionic Compounds: $\text{Pyrr}_{14}^+/\text{FeCl}_4^-$ and $\text{N}_{1444}^+/\text{FeCl}_4^-$

Microwave syntheses were done using a CEM Discover reactor. Reagents were obtained from several sources: 1-methylpyrrolidine (99%), acetonitrile (99.9%), $\text{FeCl}_3 \cdot 6\text{H}_2\text{O}$ (97%), anhydrous 1-chlorobutane (99.5%), anhydrous ethyl acetate (99.8%), anhydrous ethyl ether (99%) and methyltributylammonium chloride (98%) were purchased

from Sigma-Aldrich, Inc. HCl (37%) was purchased from Mallinckrodt Chemical, 1-chlorobutane from Eastman and ethanol (200 proof) from Pharmaco. All reagents were used as received without further purification.

Each of the four final products was dried in vacuum at 343 – 353 K for at least 24 hrs. to remove remaining solvent or water. Parent m/z ratios for both the cation and anion were confirmed using a Thermo Finnigan model LCQ Advantage electrospray ionization mass spectrometer. Recrystallization to produce crystals for X-ray diffraction was done in methanol by making a supersaturated solution at 325 – 345 K and allowing it to gradually cool at room temperature.

Pyrr₁₄⁺/FeCl₄[−] was synthesized by metathesis of methylbutylpyrrolidinium chloride (Pyrr₁₄⁺/Cl[−]) with FeCl₃·6H₂O using a similar method to the one previously reported by Evans *et al.*¹¹ Pyrr₁₄⁺/Cl[−] was prepared via microwave synthesis as follows.

1-methylpyrrolidine (141 mmol) and 1-chlorobutane (158 mmol) were mixed in a 80 ml microwave vessel with acetonitrile (153 mmol) as solvent. Reaction conditions used were: power 60 watt; temperature ramp 1 min; hold 20 min; 140 °C reaction temperature; maximum pressure set to 10.0 bar. The white precipitate product was filtered and washed with anhydrous ethyl ether. An 82% yield of Pyrr₁₄⁺/Cl[−] resulted. For the metathesis of Pyrr₁₄⁺/Cl[−] with FeCl₃·6H₂O, FeCl₃·6H₂O (9.99 mmol) was first dissolved in 37% HCl (3.29 x 10³ mmol). Precipitation of Pyrr₁₄⁺/FeCl₄[−] occurred instantly on addition of Pyrr₁₄⁺/Cl[−] (124 mmol). The Pyrr₁₄⁺/FeCl₄[−] precipitate was filtered and washed with cold ethyl acetate. The yield for Pyrr₁₄⁺/FeCl₄[−] was 76%.

N₁₄₄₄⁺/FeCl₄[−] was synthesized by a method similar to that described by Hay *et al.*¹² for the preparation of N₄₄₄₄⁺/FeCl₄[−]. FeCl₃·6H₂O (9.99 mmol) was dissolved in 37 % HCl (3.29 x 10³ mmol) after which methyltributylammonium chloride (136 mmol) was added to the yellow solution while stirring. The N₁₄₄₄⁺/FeCl₄[−] precipitate was filtered and washed with dry ethanol. The product yield was 91%.

Preparation of other ionic compounds

$N_{4444}^+/\text{FeBrCl}_3^-$ and $\text{bmim}^+/\text{FeCl}_4^-$: The $N_{4444}^+/\text{FeBrCl}_3^-$ ionic solid was prepared using the method reported by Kruszyński and Wyrzykowski.¹⁰ The room-temperature IL $\text{bmim}^+/\text{FeCl}_4^-$ was synthesized using a procedure previously reported by Hayashi, *et al.*¹

4.2.2 X-Ray Structure Determination

Single crystal x-ray diffraction was done by Dr. Thomas Emge at Rutgers University. X-ray diffraction data for $N_{1444}^+/\text{FeCl}_4^-$ and $\text{Pyrr}_{14}^+/\text{FeCl}_4^-$ were collected using a Bruker Smart APEX CCD diffractometer with graphite-monochromatized Mo $K\alpha$ radiation (incident x-ray wavelength, $\lambda_{xray} = 0.71073 \text{ \AA}$). For each structure, a crystal of approximately 0.0024 to 0.0027 mm^3 volume was immersed in Paratone-N oil and held at 100 K . The data were corrected for Lorentz and polarization effects and for absorption, the latter by using a multiscan (SADABS) method.¹³ The structure was solved by direct methods (SHELXS86).¹⁴ All non-hydrogen atoms were refined (SHELXL97) based on F_{obs}^2 .¹⁴ Crystallographic data and final R indices for $N_{1444}^+/\text{FeCl}_4^-$ and $\text{Pyrr}_{14}^+/\text{FeCl}_4^-$ are summarized in Table 4.1; full crystallographic information is provided in Crystallographic Information File (CIF) format in the Supplementary Information of the published manuscript.⁹

4.2.3 Vibrational Spectroscopy

Ambient room temperature ($294 \pm 1 \text{ K}$) Raman spectroscopy was performed using a Renishaw System 1000 dispersive micro-Raman spectrometer. The system has a 786 nm diode laser for sample illumination with a 1 cm^{-1} resolution and a Peltier-cooled CCD detector. Ambient room temperature ($294 \pm 1 \text{ K}$) Fourier-Transform infrared (FT-IR) absorption spectra were recorded using a Thermo Scientific Nicolet/Nexus 670 FT-IR spectrometer. The measured FT-IR spectra are shown in Figure 4.2.

Table 4.1: Crystallographic data for $N_{1444}^+/\text{FeCl}_4^-$ and $\text{Pyrr}_{14}^+/\text{FeCl}_4^-$ measured at 100 K.

Compound	$\text{Pyrr}_{14}^+/\text{FeCl}_4^-$	$N_{1444}^+/\text{FeCl}_4^-$
Empirical Formula	$\text{C}_{12}\text{H}_{24}\text{Cl}_4\text{FeN}$	$\text{C}_{13}\text{H}_{30}\text{Cl}_4\text{FeN}$
Formula Weight	379.97	398.03
Crystal System	hexagonal	orthorhombic
Space Group	$P6_3mc$	$Pca2_1$
a (Å)	8.223(1)	15.366(2)
b (Å)	8.223(1)	14.861(2)
c (Å)	13.030(2)	17.361(3)
α (deg)	90	90
β (deg)	90	90
γ (deg)	120	90
Cell Volume (Å ³)	763.0(2)	3964.2(11)
Z	2	8
D_{calcd} (Mg m ⁻³)	1.654	1.334
Abs coeff (mm ⁻¹)	1.671	1.289
F(000)	394	1672
No. Obs. Reflections ($I > 2\sigma(I)$)	573	11939
Goodness-of-fit on F^2	1.096	1.002
Data/restraints/parameters	573/24/34	11939/229/52
Final R Indices (Obs. Data)	$R_1 = 0.0978$, $wR_2 = 0.2643$	$R_1 = 0.0393$, $wR_2 = 0.0854$
Final R Indices (All Data)	$R_1 = 0.1013$, $wR_2 = 0.2690$	$R_1 = 0.0488$, $wR_2 = 0.0896$

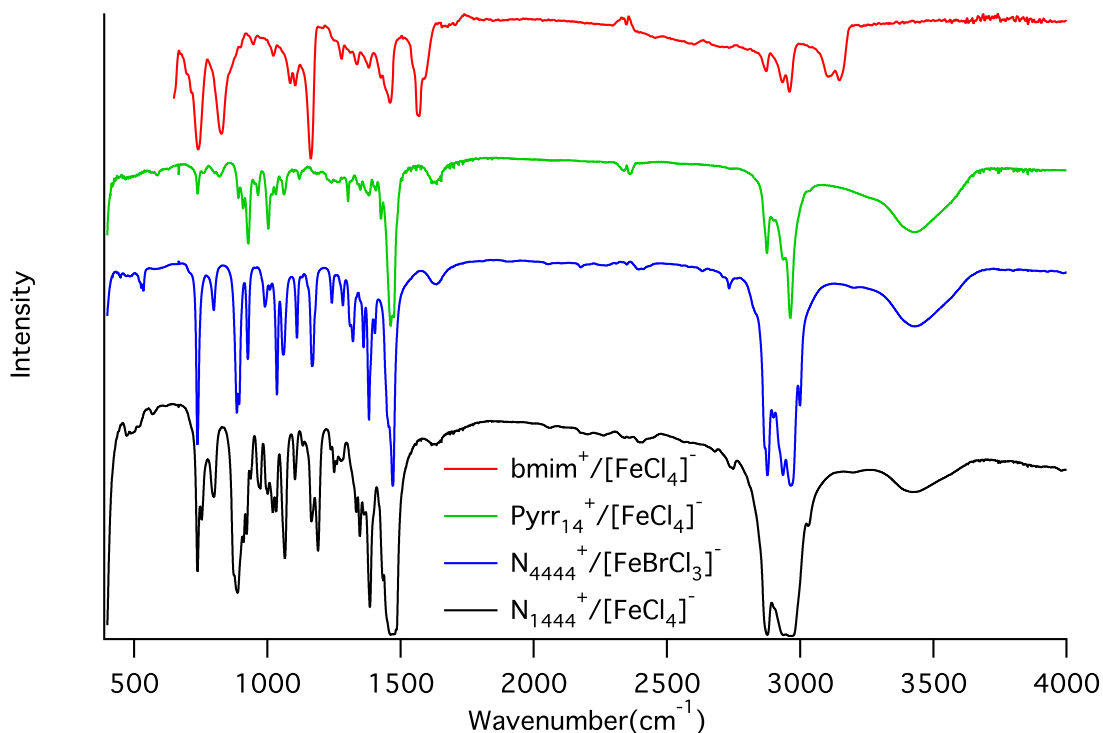


Figure 4.2: Infrared spectra of $\text{bmim}^+/\text{FeCl}_4^-$, $\text{Pyrr}_{14}^+/\text{FeCl}_4^-$, $N_{4444}^+/\text{FeBrCl}_3^-$ and $N_{1444}^+/\text{FeCl}_4^-$.

4.2.4 Thermal Measurements

Differential scanning calorimetry scans for $\text{bmim}^+/\text{FeCl}_4^-$, $\text{Pyrr}_{14}^+/\text{FeCl}_4^-$ and $\text{N}_{1444}^+/\text{FeCl}_4^-$ were taken using a LNCS-cooled TA Q100 differential scanning calorimeter (DSC). A Perkin-Elmer Pyris 1 DSC Q200 with DX instrument controller and with a nitrogen-purged sample chamber was used for $\text{N}_{4444}^+/\text{FeBrCl}_3^-$. Both instruments were pre-cooled and set at a heating/cooling rate of either 5 or 10 K/min with a minimum of 3 thermal cycles. Transition temperatures were determined using 4 - 10 mg samples. Samples for DSC experiments were prepared under ambient conditions except for the $\text{bmim}^+/\text{FeCl}_4^-$ sample, which was prepared in a nitrogen glove box.

4.2.5 Magnetic Properties

Temperature-dependent magnetic susceptibility (χ) measurements were made with a Quantum Design MPMS SQUID magnetometer. The magnetic susceptibilities of the samples were measured at a heating/cooling rate of 5 K/min, in an applied field of 1000 gauss and in the temperature range 5 to 350 K for $\text{N}_{1444}^+/\text{FeCl}_4^-$ and 5 to 400 K for $\text{N}_{4444}^+/\text{FeBrCl}_3^-$ and $\text{Pyrr}_{14}^+/\text{FeCl}_4^-$. Before conducting the susceptibility measurements, the samples were cooled from room temperature in the absence of external field. The temperature is read out by thermal diodes to an accuracy of ± 1 K. The samples were loaded into 0.13 mL Torpac gelatin capsules and the sample chamber was evacuated prior to measurement. The effective magnetic moment was calculated by the equation, $\mu_{eff} = \mu_B \sqrt{8C}$, which is dependent on the material specific Curie constant, $C = \mu_B \sqrt{\chi_M T}$, where χ_M is the molar magnetic susceptibility, T is temperature in Kelvin and μ_B is the Bohr magneton.

4.3 Results and Discussion

Single crystal diffractometry

Of the four paramagnetic ionic compounds discussed in this report, we determined the crystal structures of $\text{N}_{1444}^+/\text{FeCl}_4^-$ and $\text{Pyrr}_{14}^+/\text{FeCl}_4^-$. The $\text{N}_{4444}^+/\text{FeBrCl}_3^-$ and crystal structure has been reported previously by Kruszyński and Wyrzykowski.¹⁰

The most salient feature of the latter structure is that the iron-iron nearest neighbor spacings are 8.2 and 8.9 Å. No crystal structure is available for $\text{bmim}^+/\text{FeCl}_4^-$ since it melts at 262 K.

The structures of $\text{N}_{1444}^+/\text{FeCl}_4^-$ and $\text{Pyrr}_{14}^+/\text{FeCl}_4^-$ were solved and are illustrated in Figures 4.3 and 4.4. The X-ray diffraction data for $\text{Pyrr}_{14}^+/\text{FeCl}_4^-$ denotes a hexagonal space group. The disorder of the Pyrr_{14}^+ cation about the $(3)/m$ axis, a 3-fold axis intersecting with a mirror plane around the pyrrolidinium N atom, is most likely due to the fragile glass forming nature of this ionic liquid. It is likely that this disorder results from the presence of multiple low-energy crystal conformers. Because the crystal packing is determined by the tetrahalogenate anions, the butyl group on the Pyrr_{14}^+ cation fits into a three-fold symmetric site, leading to the observation of a crystal with ordered anions and three-fold disordered cations, as shown in Figure 4.3 (top). Figure 4.3 (bottom) illustrates that the crystal presents a layered structure, with an intra-layer iron-iron separation of 8.223 Å (the length of the a -axis) and an interlayer iron-iron spacing of 6.515(2) Å (half the length of the c -axis).

Examination of crystallographic data for tetramethyl- and tetraethyl-ammonium salts paired with small, symmetric metal halogenate anions shows that they all have layered structures.^{11,15–17} The interlayer spacing between metal centers in these structures is typically 6.6 Å, with intra-layer spacings between metals being typically 8.2 Å. Despite the length of the butyl group and quasi-rigid pyrrolidinium ring structure of Pyrr_{14}^+ , our X-ray data for $\text{Pyrr}_{14}^+/\text{FeCl}_4^-$ shows that the crystal packing is quite similar to the tetramethylammonium¹⁷ and tetraethylammonium^{11,15} crystal structures, with interlayer metal spacing of 6.5 Å and intra-layer metal atom spacings of 8.2 Å. All three structures show crystal packing in the $P6_3mc$ space group.

The structure of $\text{N}_{1444}^+/\text{FeCl}_4^-$ is shown in Fig. 4.4; for clarity, only one fourth of the unit cell is shown. The full unit cell with iron-iron distances labeled is shown in the Figure 4.5. The FeCl_4^- anions are represented in ball-and-stick format with orange Fe(III) centers and Cl atoms colored green; the planes containing the FeCl_4^- anions are parallel to the plane formed by the crystalline a and b axes and are colored

orange and light blue. The minimum iron-iron separation is 6.8 Å and the next near-neighbor distances range from 8.4 to 9.3 Å. The packing symmetry of the unit cell reveals two distinct conformations of the N_{1444}^+ cations. One N_{1444}^+ cation has butyl groups that each have a *gauche* conformation, leading to a propeller-like structure for this ion. The other N_{1444}^+ cation has one *trans* butyl conformation and two *gauche* butyl groups. To highlight this structure, the *trans* butyl groups have the hydrogens represented as magenta balls; these N_{1444}^+ cations project the *trans* butyl groups above the top yellow and central green planes that contain the $FeCl_4^-$ anions. The separations between cation hydrogen atoms and anion chlorine atoms all fall in the range between 2.8–3.0 Å.

4.3.1 Raman spectra

The ambient temperature Raman spectra are shown in Figure 4.6. Vibrational Raman spectra of our four ionic compounds in the range 100–500 cm^{-1} show the previously observed symmetric Fe-Cl $T_d : A_1$ stretch at $331.9 \pm 1.5 \text{ cm}^{-1}$ ^{4,18}. This assignment provides further verification of the presence of the $FeCl_4^-$ anion. The 260 cm^{-1} Fe–Br stretching band ν_{Fe-Br} is observed in the $N_{4444}^+/FeBrCl_3^-$ spectrum confirming the presence of a single bromine in the anion.¹⁹

4.3.2 Thermal properties

The thermal properties of $N_{4444}^+/FeBrCl_3^-$, $Pyrr_{14}^+/FeCl_4^-$ and $N_{1444}^+/FeCl_4^-$ were investigated by DSC over the temperature range 143 to 425 K. The ILs were cooled to 143 K, and either two or three heat/cool cycles were scanned to reveal the details of intermediate, history-dependent phase behavior. The complete sets of DSC scans are shown in Figure 4.7. $N_{4444}^+/FeBrCl_3^-$ and $N_{1444}^+/FeCl_4^-$ cannot be classified as ionic liquids since they have melting points higher than 100 °C. $N_{4444}^+/FeBrCl_3^-$ exhibits a solid-solid transition at 379 K and a melting point at 409 K. Glass transitions were not observable for $N_{4444}^+/FeBrCl_3^-$ and $N_{1444}^+/FeCl_4^-$ because these salts crystallize easily upon cooling and are very difficult to quench as glasses. During the cooling process, $N_{1444}^+/FeCl_4^-$ crystallizes into a state that is metastable at lower

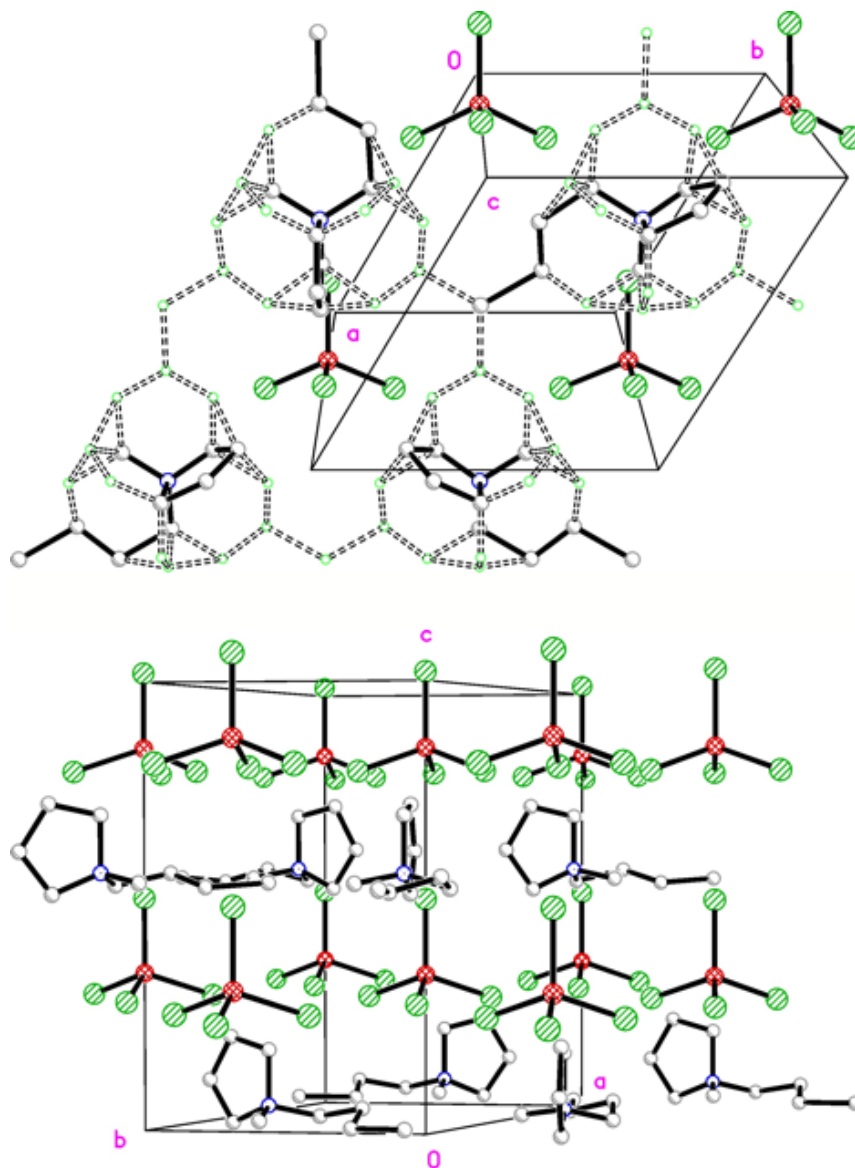


Figure 4.3: Molecular packing of Pyrr₁₄⁺/FeCl₄⁻ (top). Orientation of this view is approximately 15 degrees offset from the crystallographic *c*-axis. The FeCl₄⁻ anions are highly ordered, while the Pyrr₁₄⁺ cations are disordered. An arbitrarily chosen Pyrr₁₄⁺ conformation is indicated by the solid cation bonds; the remaining bonds in the disordered cation are shown by the open-dashed links (bottom). This view is offset approximately 10 degrees from the diagonal between the crystallographic *a* and *b* axes. Site disordered atoms have been removed to illustrate one arbitrarily chosen cation per site.

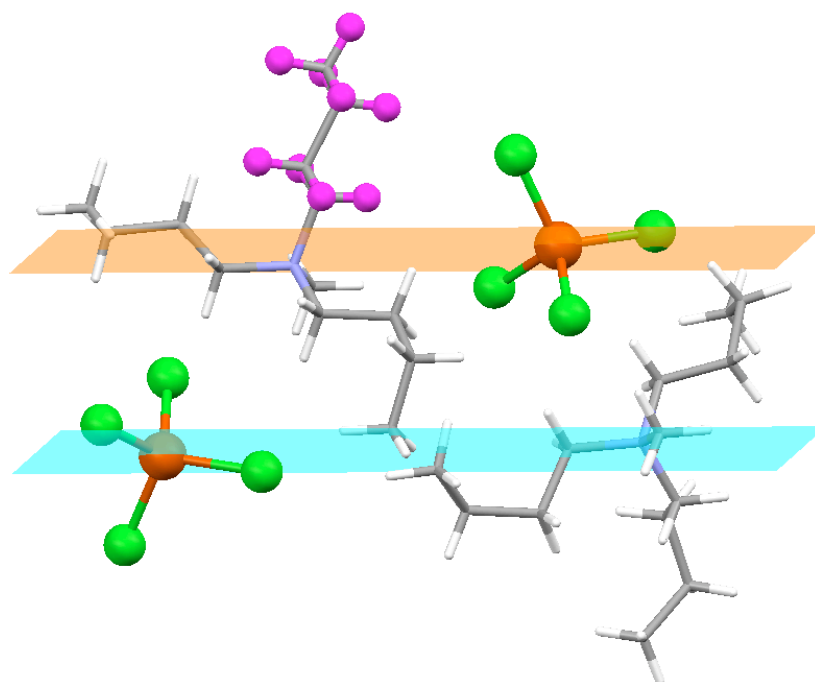


Figure 4.4: Molecular packing of $N_{1444}^+ / FeCl_4^-$. One-quarter of the total unit cell is shown. The orange and blue planes are orthogonal to the crystal *c*-axis. $FeCl_4^-$ anions are shown in ball-and-stick representation; iron atoms colored orange and chlorine atoms green. The lower N_{1444}^+ cation presents a propeller-like conformation with the three all-*gauche* butyl groups; the upper N_{1444}^+ cation shows one *trans* butyl group and two *gauche* butyl groups. The *trans* butyl group at top is labeled with magenta H atoms.

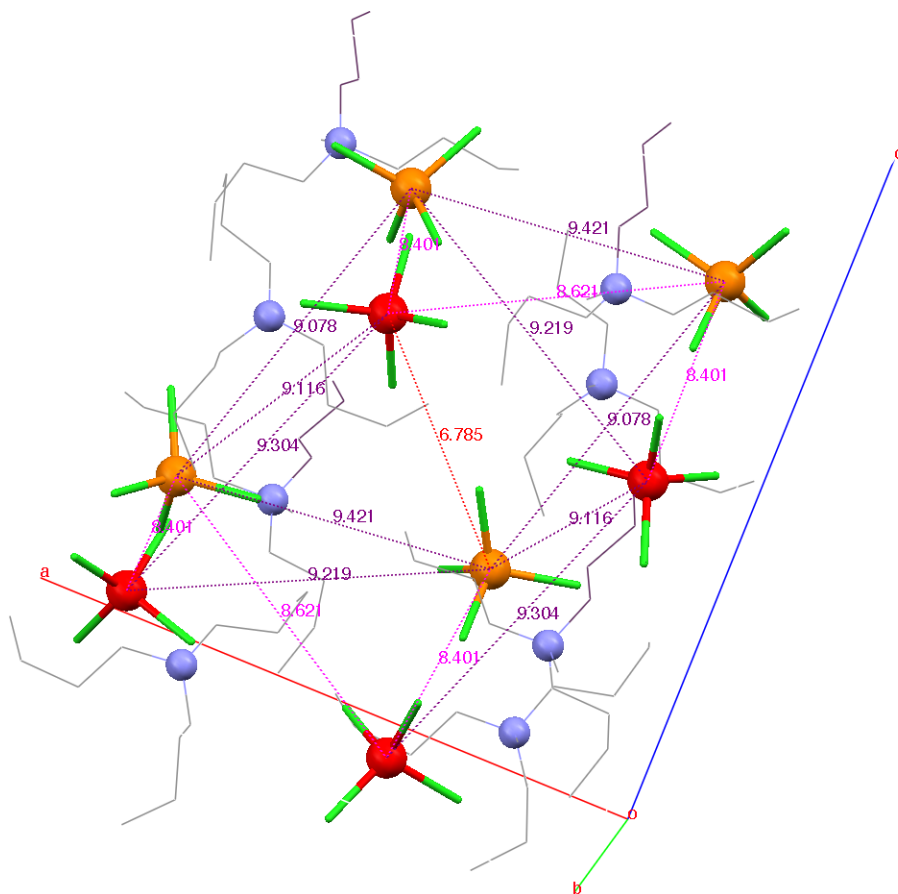


Figure 4.5: Diagram of the unit cell of $N_{1444}^+ / FeCl_4^-$ showing the distances between the iron atoms, depicted in red and orange to represent the two inequivalent positions. There is one relatively short separation of 6.785 Å per pair of inequivalent iron atoms. All other distances are greater than 8 Å.

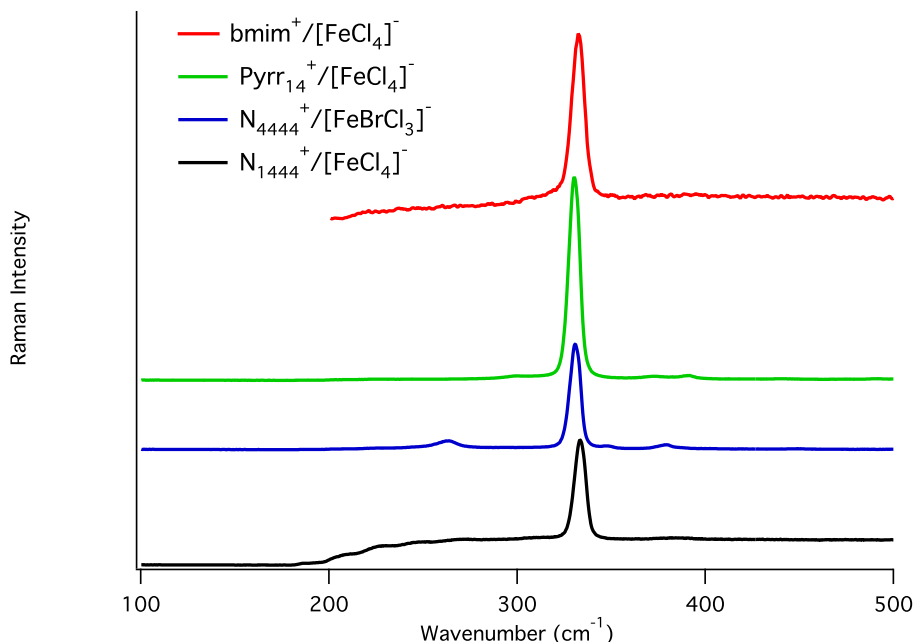


Figure 4.6: Raman spectra of $\text{bmim}^+/\text{FeCl}_4^-$, $\text{Pyrr}_{14}^+/\text{FeCl}_4^-$, $\text{N}_{4444}^+/\text{FeBrCl}_3^-$ and $\text{N}_{1444}^+/\text{FeCl}_4^-$. The FWHM for Raman line shapes are 4.689 cm^{-1} ($\text{bmim}^+/\text{FeCl}_4^-$), 4.157 cm^{-1} ($\text{Pyrr}_{14}^+/\text{FeCl}_4^-$), 3.976 cm^{-1} ($\text{N}_{4444}^+/\text{FeBrCl}_3^-$), and 4.253 cm^{-1} ($\text{N}_{1444}^+/\text{FeCl}_4^-$).

temperatures, which upon heating anneals through an exothermic process at 257 K. A transition between solid phases occurs at 301 K, a weak and history dependent annealing transition occurs at 317 K (approximately where $\text{N}_{1444}^+/\text{FeCl}_4^-$ undergoes snap crystallization when cooled) and a melting transition at 383 K. On the first scan of unmelted solid $\text{N}_{1444}^+/\text{FeCl}_4^-$, all of the previously-mentioned phase transitions are weak except for the melting transition at 383 K. On a related note, the thermal properties of $\text{N}_{4444}^+/\text{FeCl}_4^-$ were reported by Wyrzykowski *et al.*; a solid-solid transition at 379 K preceded the melting transition at 409 K.²⁰

We observed thermal behavior for $\text{bmim}^+/\text{FeCl}_4^-$ consistent with that reported previously by Yamamuro, *et al.*⁶ On heating $\text{bmim}^+/\text{FeCl}_4^-$, we found a reproducible melting transition at 262.4 K, preceded by a cold crystallization at about 240 K. This confirms the classification of $\text{bmim}^+/\text{FeCl}_4^-$ as a room temperature ionic liquid, as opposed to being persistently supercooled, for example. The glass transition onset temperature of $\text{bmim}^+/\text{FeCl}_4^-$ is 189 K. Similar thermal properties are seen for the IL $\text{Pyrr}_{14}^+/\text{FeCl}_4^-$, with a glass transition at 191 K, a solid-solid phase transition at 221 K, and a melting point at 354 K, well above room temperature but still qualifying

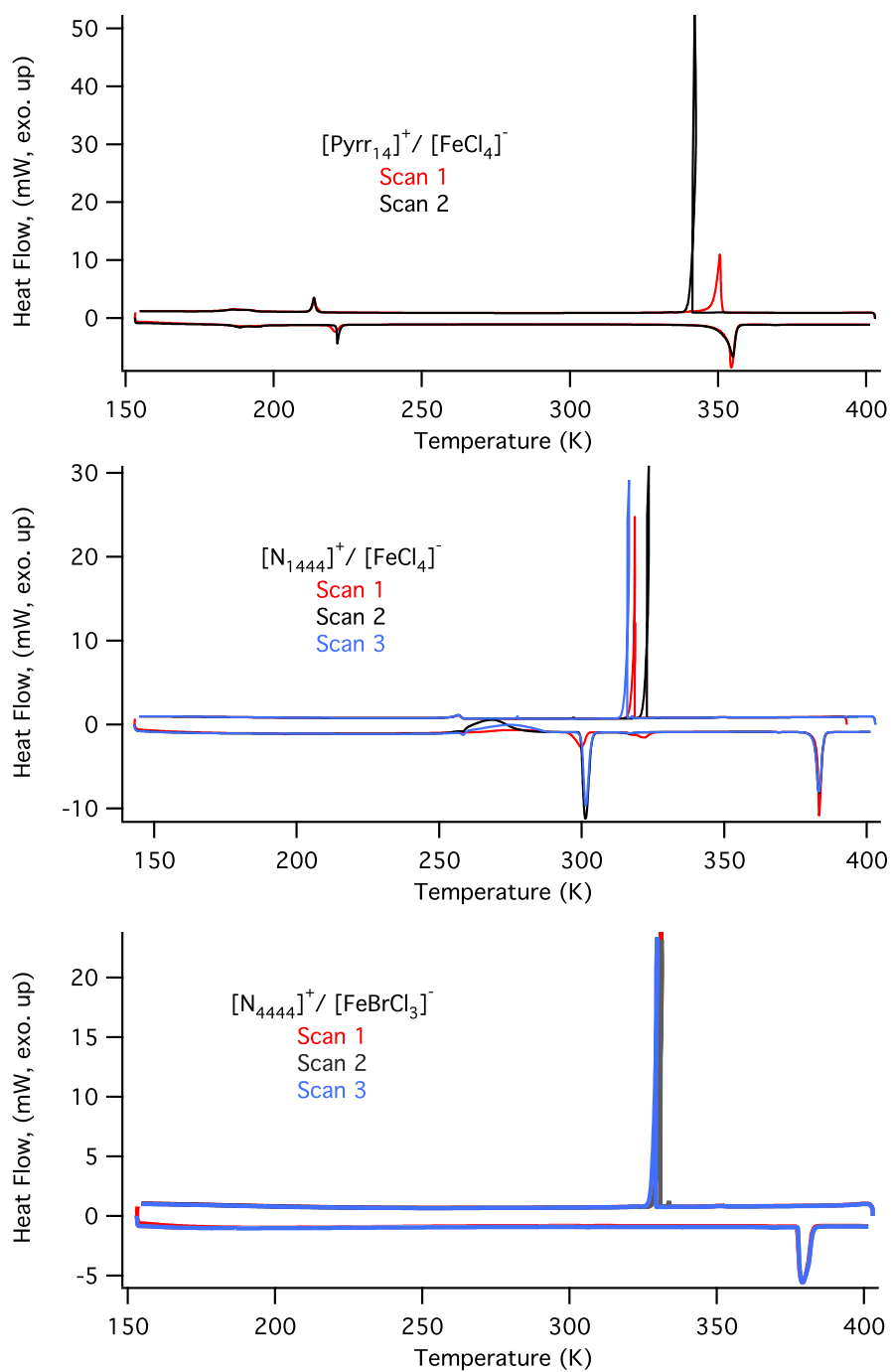


Figure 4.7: DSC scans of $\text{Pyrr}_{14}^+ / \text{FeCl}_4^-$, $\text{N}_{1444}^+ / \text{FeCl}_4^-$, and $\text{N}_{4444}^+ / \text{FeBrCl}_3^-$. The data in this figure show the repetitive DSC scans measured at Brookhaven National Laboratory. Upon detailed examination of the data for $\text{N}_{4444}^+ / \text{FeBrCl}_3^-$, the lack of an appreciable heat capacity increase after the transition at 379 K suggested that it was not a melting transition.

as an IL. Upon cooling, $\text{Pyrr}_{14}^+/\text{FeCl}_4^-$ recrystallizes abruptly between 350 and 342 K, and the solid-solid phase transition observed when heating is mirrored at 214 K in the cooling scans. Despite the existence of solid phases of $\text{Pyrr}_{14}^+/\text{FeCl}_4^-$ at low temperatures, there is enough disorder remaining to reveal the weak glass transition.

Table 4.2: DSC transition temperatures in K. Peak values are reported for the melting transitions, while all others are reported as onset temperatures. Entropies of fusion is in $\text{J mol}^{-1}\text{K}^{-1}$. Transition enthalpies are listed in parentheses (in kJ/mol) in the columns for T_{s-s} and T_m .

Cation ΔS_f	Anion	T_g	$T_{coldcryst/anneal}$	T_{s-s}^a	T_{anneal}	T_m
N_{4444}^+ 33.7	FeBrCl_3^-	–	–	379 (15.7)	–	409 (13.8)
bmim^+ 16.7	FeCl_4^-	189	240	–	–	262 (4.38)
Pyrr_{14}^+ 44.1	FeCl_4^-	191	–	221	–	354 (15.6)
N_{1444}^+ 44.4	FeCl_4^-	–	257	301 (19.7)	317	383 (17.0)

^a Transition between two solid phases.

4.3.3 Magnetic properties

Magnetic susceptibility measurements are plotted in Figure 4.8 as $\chi_M T$ vs. temperature for $\text{N}_{4444}^+/\text{FeBrCl}_3^-$, $\text{N}_{1444}^+/\text{FeCl}_4^-$ and $\text{Pyrr}_{14}^+/\text{FeCl}_4^-$. Magnetic susceptibilities for the room-temperature IL $\text{bmim}^+/\text{FeCl}_4^-$ were previously reported by Hamaguchi *et al.*¹ and Yoshida *et al.*² and the magnetic properties of $\text{N}_{4444}^+/\text{FeBrCl}_3^-$ were reported in detail by Wyrzykowski *et al.*¹⁷ All four compounds are paramagnetic at ambient temperatures. Paramagnetism is common in dilute transition-metal salts as the unpaired electrons interact weakly and their spins, which are randomly oriented at room temperature, align slightly in an external field. The Curie-Weiss Law (Eq. 4.1), was used to fit the data to find the material-dependent Curie and Weiss constants,

$$\chi = \frac{C}{T - \theta}, \quad (4.1)$$

where C is the Curie constant, T is the temperature in K and θ is the Weiss constant. The magnetic susceptibilities, effective magnetic moments and Curie constants are listed in Table 4.3. The calculated Weiss constants are reported in with the magnetic susceptibility spectra ($1/\chi_M$ vs. temperature) in Figure 4.9. We note that the Weiss constants are close to zero within the experimental uncertainties. The effective magnetic moments have been calculated and are in agreement with the $S = 5/2$ high-spin electronic state of Fe(III) which has a spin-only value of $5.92 \mu_B$. Figure 4.8 shows the product of molar susceptibility and temperature, $\chi_M T$, as a function of temperature. For clarity, only the heating curves are shown in Figure 4.8 since the cooling curves are superimposeable with the heating curves. In general, the $\chi_M T$ remains fairly constant over the temperatures investigated. The decrease in $\chi_M T$ for temperatures below 35 K for $N_{1444}^+/\text{FeCl}_4^-$ and $N_{4444}^+/\text{FeBrCl}_3^-$ is most significant for the latter compound. This drop in $\chi_M T$ with decreasing temperature is consistent with weakly antiferromagnetic behavior.²¹ However, there are no deviations from monotonic behavior of $\chi_M T$ with decreasing temperature, indicating the absence of a Néel temperature. Minor bumps in the magnetic susceptibilities for the other salts correspond with phase transitions observed in the DSC data. $N_{1444}^+/\text{FeCl}_4^-$ has a transition at 301 K that is matched by a jump in the value of $\chi_M T$. The solid-solid transition of $N_{4444}^+/\text{FeBrCl}_3^-$ observed at 379 K in the DSC scan corresponds with the increase in the $\chi_M T$ at the end of the measurement beginning at 381 K. The values we obtain for $N_{4444}^+/\text{FeBrCl}_3^-$ are in good agreement with those previously reported by Wyrzykowski *et al.*²²

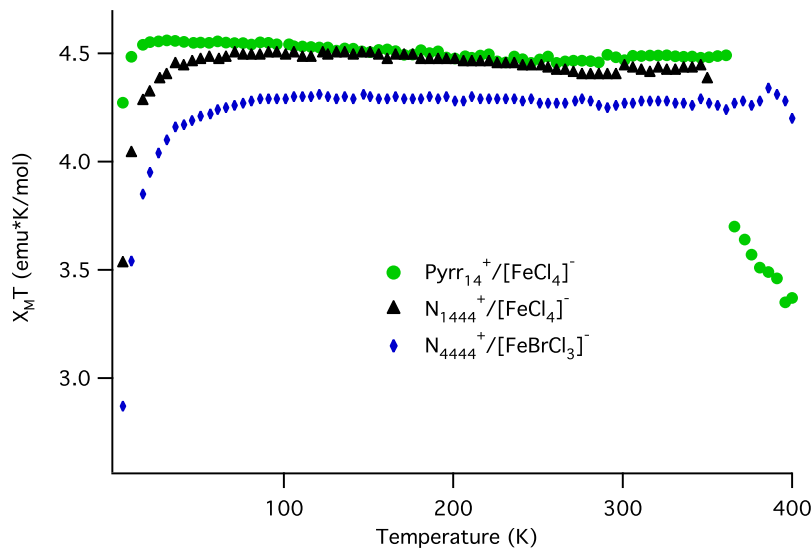


Figure 4.8: $\chi_M T$ vs. temperature for $N_{1444}^+/\text{FeCl}_4^-$, $\text{Pyr}_{14}^+/\text{FeCl}_4^-$ and $N_{4444}^+/\text{FeBrCl}_3^-$, for a heating and cooling rate of 5 K/min. Note that the sharp decrease in the value of $\chi_M T$ at 361 K for $\text{Pyr}_{14}^+/\text{FeCl}_4^-$ results from melting of the sample.

Table 4.3: Magnetic properties of $N_{1444}^+/\text{FeCl}_4^-$, $\text{Pyr}_{14}^+/\text{FeCl}_4^-$, and $N_{4444}^+/\text{FeBrCl}_3^-$.

Compound	$N_{1444}^+/\text{FeCl}_4^-$	$\text{Pyr}_{14}^+/\text{FeCl}_4^-$	$\text{bmim}^+/\text{FeCl}_4^-$	$N_{4444}^+/\text{FeBrCl}_3^-$
Curie Const. (emu-K/mol)	4.41	4.47	—	4.28 (5.06 ^c)
μ_{eff} (μ_B)	5.29	5.98	5.82 ^a	5.85
At 300 K:				
$\chi_M T$ (emu-K/mol)	4.42	4.47	4.11 ^b	4.27 (4.95 ^c)
μ_{eff} (μ_B)	5.95	5.98	5.73 ^b	5.84 (6.29 ^c)
At 100 K:				
$\chi_M T$ (emu-K/mol)	4.49	4.54	—	4.26
μ_{eff} (μ_B)	5.99	6.03	—	5.84
At 5 K:				
$\chi_M T$ (emu-K/mol)	3.53	4.27	—	2.81
μ_{eff} (μ_B)	5.31	5.84	—	4.79

^a Values from Yoshida *et al.*²

^b χ_M value at 300 K from Hayashi, *et al.*⁴ used to calculate $\chi_M T$ and μ_{eff} .

^c Values obtained using a 0.5 T external magnetic field by Wyrzykowski *et al.*²²

$N_{1444}^+/\text{FeCl}_4^-$ FW = 398.0 g/mol; $\text{Pyr}_{14}^+/\text{FeCl}_4^-$ FW = 339.9 g/mol; $N_{4444}^+/\text{FeBrCl}_3^-$ FW = 484.6 g/mol)

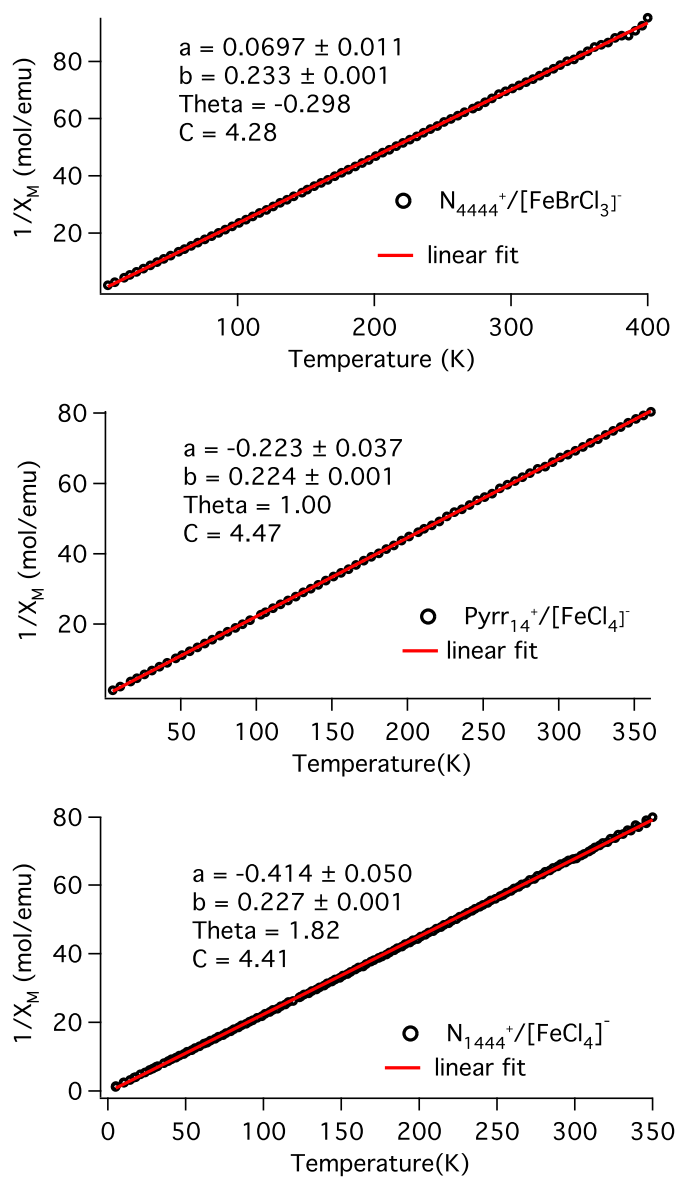


Figure 4.9: Inverse χ_M vs. temperature for $Pyr_14^+ / [FeCl_4]^-$, $N_{1444}^+ / [FeCl_4]^-$ and $N_{4444}^+ / [FeBrCl_3]^-$.

4.4 Conclusions

Four paramagnetic ionic compounds have been prepared: $\text{Pyrr}_{14}^+/\text{FeCl}_4^-$, $\text{N}_{1444}^+/\text{FeCl}_4^-$, $\text{N}_{4444}^+/\text{FeBrCl}_3^-$ and $\text{bmim}^+/\text{FeCl}_4^-$; the synthesis and characterization of the first two are reported here for the first time. While only $\text{bmim}^+/\text{FeCl}_4^-$ is liquid at ambient temperature, $\text{Pyrr}_{14}^+/\text{FeCl}_4^-$ qualifies as an ionic liquid with a melting point of 355 K. Though $\text{bmim}^+/\text{FeCl}_4^-$ and $\text{Pyrr}_{14}^+/\text{FeCl}_4^-$ have T_g values of 189 and 191 K, respectively, the melting temperature of the latter is 92 K above that of the former. This is apparently due to the much smaller enthalpy of fusion for the imidazolium salt (Table 4.2).

Paramagnetism in these ionic liquids and solids results from the Fe(III)-containing anions, with weak antiferromagnetism being observed near 5 K for all four compounds. The crystal structures of the two new compounds reveal somewhat unusual amounts of disorder. The $\text{Pyrr}_{14}^+/\text{FeCl}_4^-$ crystal shows a highly ordered hexagonal lattice for the FeCl_4^- anions, but threefold orientational disorder for the Pyrr_{14}^+ cations. The orthorhombic crystal structure found for $\text{N}_{1444}^+/\text{FeCl}_4^-$ shows that the two unique cations in the unit cell have different conformations of the butyl groups.

These and related paramagnetic ionic liquids and solids may provide the basis for strongly paramagnetic media that can exist in crystal, vitreous, liquid or solution conditions. Such paramagnetic and ionic media will likely find applications in separations chemistry, catalysis, and nanotechnology. In particular, FeCl_4^- ionic liquids seem well positioned for use as alternatives for FeCl_3 in Friedel-Crafts or Grignard reactions.

Bibliography

- [1] S. Hayashi and H. O. Hamaguchi. Discovery of a magnetic ionic liquid [bmim]FeCl₄. *Chemistry Letters*, 33:1590–1591, 2004.
- [2] Y. Yoshida, A. Otsuka, G. Saito, S. Natsume, E. Nishibori, M. Takata, M. Sakata, M. Takahashi, and T. Yoko. Conducting and magnetic properties of 1-ethyl-3-methylimidazolium (EMI) salts containing paramagnetic irons: Liquids [EMI](MCl₄)-Cl-III] (M = Fe and Fe_{0.5}Ga_{0.5}) and solid [EMI]₍₂₎[(FeCl₄)-Cl-II]. *Bul. Chem. Soc. Jpn.*, 78:1921–1928, 2005.
- [3] Y. Yoshida and G. Saito. Influence of structural variations in 1-alkyl-3-methylimidazolium cation and tetrahalogenoferrate(III) anion on the physical properties of the paramagnetic ionic liquids. *J. Mat. Chem.*, 16:1254–1262, 2006.
- [4] S. Hayashi, S. Saha, and H.-o. Hamaguchi. A new class of magnetic fluids: bmim[FeCl₄] and nbmim[FeCl₄] ionic liquids. *IEEE Transactions on Magnetics*, 42:12–14, 2006.
- [5] M. Okuno, H. Hamaguchi, and S. Hayashi. Magnetic manipulation of materials in a magnetic ionic liquid. *Appl. Phys. Lett.*, 89:132506, 2006.
- [6] O. Yamamuro, Y. Minamimoto, Y. Inamura, S. Hayashi, and H. O. Hamaguchi. Heat capacity and glass transition of an ionic liquid 1-butyl-3-methylimidazolium chloride. *Chem. Phys. Lett.*, 423:371–375, 2006.
- [7] R. E. Del Sesto, T. M. McCleskey, A. K. Burrell, G. A. Baker, J. D. Thompson, B. L. Scott, J. S. Wilkes, and P. Williams. Structure and magnetic behavior of transition metal based ionic liquids. *Chem. Comm.*, pages 447–449, 2008.
- [8] P. Brown, A. Bushmelev, C. P. Butts, J. Cheng, J. Eastoe, I. Grillo, R. K. Heenan,

- and A. M. Schmidt. Magnetic control over liquid surface properties with responsive surfactants. *Angew. Chem.*, 51:2414–2416, 2012.
- [9] B. M. Krieger, H. Y. Lee, T. J. Emge, J. F. Wishart, and E. W. Castner Jr. Ionic liquids and solids with paramagnetic anions. *Phys. Chem. Chem. Phys.*, 12:8919–8925, 2010.
- [10] R. Kruszyński and D. Wyrzykowski. Tetrabutylammonium bromotrichloroferrate(III). *Acta Crystallographica*, E62:m994–m996, 2006.
- [11] D. J. Evans, A. Hills, D. L. Hughes, and G. J. Leigh. Structures of tetraethylammonium tetrachloroferrate(III) and the mixed halide iron(III) complex, $[\text{NEt}_4][\text{FeBrCl}_3]$. *Acta Crystallographica*, C46:1818–1821, 1990.
- [12] M. T. Hay and S. J. Geib. Tetrabutylammonium tetrachloroferrate(iii). *Acta Crystallographica*, E61:m190–m191, 2005.
- [13] Bruker-AXS. *SADABS, Bruker Nonius Area Detector Scaling and Absorption Correction*. Bruker-AXS Inc., 2003.
- [14] G. M. Sheldrick. A short history of SHELX. *Acta Crystallographica Section A*, 64(1):112–122, 2008.
- [15] J. Trotter, F. W. B. Einstein, and D. G. Tuck. The crystal structure of tetraethylammonium tetrachloroindate(iii). *Acta Crystallographica*, B25:603–604, 1969.
- [16] M. Lenck, S. Dou, and A. Weiss. Tetraalkylammonium tetrachlorothallates (III) - X-ray, Cl-35-NQR, and H-1-NMR studies. *Zeitschrift für Naturforschung Section A - A Journal of Physical Sciences*, 46:777–784, 1991.
- [17] D. Wyrzykowski, R. Kruszynski, J. Mrozinski, and Z. Warnke. Structural and magnetic characteristics of tetramethylammonium tetrahalogenoferrates(III). *Inorg. Chim. Acta*, 361:262–268, 2008.
- [18] M. S. Sitze, E. R. Schreiter, E. V. Patterson, and R. G. Freeman. Ionic liquids based on FeCl_3 and FeCl_2 . Raman scattering and ab initio calculations. *Inorganic Chemistry*, 40:2298–2304, 2001.

- [19] S. K. Jain, B. S. Garg, and Y. K. Bhoon. Iron(III) complexes of 2-acetylpyridine-4-phenyl-3-thiosemi-carbazones: Magnetic, E.S.R. and spectral studies. *Transition Metal Chemistry*, 11:89–95, 1986.
- [20] D. Wyrzykowski, T. Maniecki, A. Pattek-Janczyk, J. Stanek, and Z. Warnke. Thermal analysis and spectroscopic characteristics of tetrabutylammonium tetrachloroferrate(III). *Therm. Acta*, 435:92–98, 2005.
- [21] A. Wold and K. Dwight. *Solid State Chemistry: synthesis, structure, and properties of selected oxides and sulfides*. New York: Chapman & Hall, 1993.
- [22] D. Wyrzykowski, R. Kruszynski, J. Kak, J. Mrozinski, and Z. Warnke. Magnetic characteristics of tetrabutylammonium tetrahalogenoferrates(III): X-ray crystal structure of tetrabutylammonium tetrabromoferrate(III). *Z. Anorg. Allg. Chem.*, 633:2071–2076, 2007.

Chapter 5

Summary and Future Directions

This thesis presents diverse perspectives on the physical chemistry of ILs. Chapter 2 details our study on intramolecular electron-transfer reactions using IL solvents, in which heterogeneous solvation dynamics were observed. These results motivated the in-depth study of the structural ordering of ILs using 2D NMR and x-ray scattering presented in Chapter 3. Finally, Chapter 4 discusses investigations of novel paramagnetic ionic materials and the practical applications of ILs in devices and smart materials. The results from this work illustrate limitless possibilities of using ILs because of their unique chemical and physical properties. Below, I comment on the results from each chapter and conclude with a discussion of future directions that are inspired by each research topic.

In Chapter 1, ILs were defined and the properties that make these liquids different from common neutral solvents were discussed. The research area of ILs has grown exponentially in the past decade due to the versatility of these new classes of liquids.^{1,2} While there are about six hundred conventional solvents that are used in industry, there are over 10^{18} combinations of cations and anions that can make up ILs.¹ Because of the large range of ILs that can be synthesized, researchers have shown that ILs with practically any desired properties can exist depending on which functional group is attached to either the cation or the anion. The rapidly evolving and growing field of ILs requires the researchers to always be up-to-date with the emerging informations and reviews.³

The investigation of charge transfer reactions in ILs is discussed Chapter 2. The unusual properties of ILs have led to studies that use these natural electrolytes in electron-transfer reactions, showing potential applications in light harvesting devices.

Our interest was to study how the solvation dynamics of ILs affect electron-transfer processes. We conducted comparative studies between ILs and neutral solvents on photoexcited intramolecular electron-transfer within a D–B–A system using time-correlated fluorescence spectroscopy and electrochemistry. The electron transfer system studied was the D–B–A molecule called DMPD–Pro–C343, where the photo-excited state of the C343 acceptor was reductively quenched by DMPD. The two ILs studied were $\text{Pyrr}_{14}^+/\text{NTf}_2^-$ and $\text{N}_{1444}^+/\text{NTf}_2^-$; the viscosity of $\text{N}_{1444}^+/\text{NTf}_2^-$ at room temperature is 8-fold larger than that of $\text{Pyrr}_{14}^+/\text{NTf}_2^-$. We compared ET kinetics in the ILs with those in the neutral solvents. In order to describe the highly non-exponential emission transients observed in ILs, a method of distribution fitting was developed. Broad distributions of ET kinetics were observed in the ILs while discrete rate processes were observed in the neutral solvents. The effective electron transfer rates are slower in the ILs than in the neutral solvents. The rates do correlate with viscosity, though not linearly. Analysis of the electrochemistry results shows that the electron transfer from $\text{D–B–A} \rightarrow \text{D}^+ \text{–B–A}^-$ in all four solvents is in the Marcus inverted regime ($-\Delta G > \lambda$) with the estimated reorganization energy, $\lambda \approx 1.2$ eV. The calculated Zusman adiabaticity parameters show a strong donor-acceptor coupling for DMPD-Pro-C343, placing this ET reaction clearly in the solvent-controlled regime for the ILs. The D–B–A molecule was found to be in the adiabatic electron-transfer regime with the electronic coupling H_{DA} for 3-state value of at least 120 cm^{-1} .

Our findings from the charge transfer studies demonstrated that electron transfer processes in ILs are complicated for several reasons. One of the reasons is because it is difficult to separate the fluorescence dynamics of the acceptor from the electron-transfer reaction. This resulted from the already heterogeneous solvation dynamics of ILs that overlaps with the electron transfer time scale. Whether this dynamic heterogeneity arises from heterogeneous structural ordering in the ILs or from reactions that occur at different rates for different sites is one of the areas that requires further investigation. Maroncelli and co-workers have shown^{4,5} that the solvation responses of ILs to the coumarin 153 fluorescent probe are broadly distributed. Others groups showed similar nonexponential solvation responses of ILs spanning time scales from sub-ps to tens of

ns.^{6–13} Sahu, *et al.*¹⁴ have applied a novel nonlinear optical method called multiple population-period transient spectroscopy to auramine in 3-butyl-1-methylimidazolium hexafluorophosphate. They reported that the “primary cause of rate heterogeneity is a long-lived local electric field acting on the charge redistribution during the reaction.” They have found that charge transfer reactions in ILs are sensitive to viscosity and total polarity of the solvent and those factors affect portions of solvation dynamics that make up the total solvation dynamics of the given solvent. More studies such as the ones from the Berg group^{14,15} need to be pursued to examine more closely the dynamically heterogeneous nature of ILs.

There are many areas that need further investigation on the topic of electron-transfer studies in ILs; one of them is to vary the electron-transfer complex by varying the length of the bridge. Issa *et al.*¹⁶ reported that increasing the number of the bridging molecules does not necessarily slow down the electron-transfer rate since the coupling between the donor and acceptor can vary in either direction due to the range of conformations the D–B–A compound can occupy with an increased number of proline spacers. How would IL solvents affect the conformational distribution of the proline-bridged donor-bridge-acceptor compound? Based on the findings from this research, my hypothesis is that the ET rates and rate distribution will be different in ILs relative to neutral solvents even when the length of the bridge is varied. In terms of the electronic coupling between the donor and acceptor, however, the transition threshold between nonadiabatic and adiabatic ET rates for the DMPD–Pro–C343 compound in ILs was calculated to be dramatically lower than the threshold reported by Zusman,¹⁷ putting our D–B–A system in the solvent controlled regime in ILs. This result leads us to hypothesize that even for the longer bridged D–B–A system, the ET reaction will remain in the solvent-controlled regime in ILs. However, to what extent the solvent coupling of the D–B–A ET process will affect the ET rate will need to be tested by experiment.

The kinds of IL solvent environment that the D–B–A compounds will be dissolved in will also effect the ET rate. Comparing the ET reaction dynamics in higher viscosity solvent systems such as glycerol with high viscosity ILs may clarify the relative effects of the viscosity and the ionic nature of the ILs. I believe that due to the polarity

inhomogeneity on the molecular level of the solvent, the ET rate (and conformation of the D–B–A molecule) will be affected. The heterogeneous solvation dynamic nature of the ILs will make such investigations complicated, but such comparisons would help us understand not only the intrinsic nature of the ILs but also of the ET system being studied.

The mechanistic details of the electron-transfer reaction for DMPD–Pro–C343 should be studied. What occurs after the forward photoinduced intramolecular electron transfer of the DMPD–Pro–C343 complex is a question that may be answered by using femtosecond transient absorption spectroscopy. By observing the rise of the signal from the absorption of the DMPD⁺ product rather than the decay of the C343 excited state, we could confirm the process of reductive quenching within the DMPD–Pro–C343* molecule. Also, femtosecond transient absorption spectroscopy will allow detection of processes too fast for TCSPC. Combining this with a series of pulse radiolysis and computational methods, designed to identify the spectra of the charge-separated states of DMPD–Pro–C343, we hope to understand the effects of the overlap between excited-state solvation dynamics and electron-transfer kinetics.

Chapter 3 is an effort to explore how dynamical heterogeneity might arise in ILs by looking at aspects of their structural heterogeneity. Experiments showing the difference in IL structural ordering for cations with short and long alkyl chains have been reported by many.^{18–21} The experimental results have been complemented by molecular dynamic simulations that illustrate the charge ordering and self aggregation of the alkyl tails.²² One of the features that indicates nanoscale structural ordering in ILs is the presence of the pre-peak in the x-ray scattering structure function.²³ This pre-peak is only apparent for the ILs with cations with longer alkyl chains^{24,25} and therefore it has been interpreted as evidence for tail aggregation. Our group, together with our collaborators, have taken this analysis a step further and have varied the polarity of the typical apolar chains of cations by substituting ether groups for alkyl chains.²⁶ As expected, the ILs with octyl chains displayed a pre-peak in the x-ray scattering function but the substitution of ether groups on the chain completely suppressed this first sharp diffraction peak.²⁶ To address the question of why this difference in x-ray

scattering data between alkyl- vs. ether- substituted cations exists, we used 2D-NMR to examine the structural ordering of these ILs.

The results from 2D-NMR nuclear Overhauser effect experiments were remarkable because there was a clear difference observed for where the anion fluorine atoms prefer to interact with the cation. For the ILs with cations with octyl chains, the fluorine atoms were interacting more closely with the protons near the polar head. This is a similar result to 2D-NMR experiments performed on imidazolium²⁷ and pyrrolidinium²⁸ based ILs -where the fluorine atoms were found in close proximity of the protons on cation rings but not on the alkyl tails. However, in the case of the ether group substituted cations, the fluorine atoms were found to have very strong interactions with the methylene protons between the two ether oxygen atoms. The results of the 2D-NMR experiments led us to hypothesize that the difference in structural ordering in the two types of ILs (one with non-polar alkyl chain and the other with a polar diether chain) results from differences in cation-anion ordering due to the preferential interaction of different sets of cation hydrogens with the anion.

What happens when cations or anions having different chain lengths are mixed? Combining shorter and longer chain length cations with the same anions and studying the self-diffusion behavior for each cation (and the anion) would elucidate the structure heterogeneity of the IL mixture. This kind of study may reveal which nanostructure ordering dominates the macrostructure of the IL as a whole. One hypothesis is that the tail aggregation of the longer chain containing ILs will form rigid structures that the diffusion of the shorter tail containing cations will have faster diffusion rate than the ILs with longer chains. What if polar and non-polar chains are mixed? The effect of the mixture of cations on the x-ray scattering change in the pre-peak, and 2D NMR studies where will one find the strongest crosspeaks with the anions, may reveal the heterogeneous structural ordering of ILs. The most exciting future research direction for me, however, would be time-dependent structure studies to determine if the structural heterogeneity is connected to the dynamic heterogeneity. The x-ray scattering and molecular dynamics studies both provide averaged time structures, spatially and temporally. Therefore, watching the structure change over time using techniques such

as quasi-elastic neutron scattering would shine new light onto our understanding of structural ordering in ILs. Time-dependent structural ordering has also been discussed recently.²⁹

Another area of studies that arose from the 2D-NMR research was the effect of water on the structural ordering of ILs. The effects of water on ILs have been reported by many.^{30–35} Others have used 2D NMR to explore the effects of solvents such as water, CH₃OH and CH₂Cl₂ on nanoscale structural ordering as the solvent molecules interact with the anions.^{27,36,37} Because studies to date have only considered ILs with ring systems, investigating such solvent-anion interaction using 2D-NMR and finding the structural ordering of non-ring tetrahedral cation systems such as phosphonium and ammonium based ILs will be useful in understanding the difference, if there exists any, between the structures of ILs based on different types of cations. In addition, it will be interesting to vary the physical properties of the ILs of interest, such as viscosity and surface tension, and look for a relationship between bulk properties and molecular scale structural ordering. What about the effects of cosolvents, such as acetonitrile and water on polar ILs? Another area that should be studied is to what extent the anions will compete with polar entities such as water in the neat IL to form the preferred structural ordering that exists in nearly dry IL.³⁸

The last chapter of this thesis reported on the development of novel paramagnetic ILs and solids. The research was begun with the goal of developing nanotubes filled with the novel paramagnetic ILs. It was our vision to develop possible magnetic materials such as nano motors and nano magnets. Since the work was published,³⁹ Brown,*et al.* reported the world's first magnetic soap.⁴⁰ Our work was another proof that ILs are versatile and the correct pairing of cations and anions will result in the IL desired.

ILs represent a significant contribution to the future of technology. Increasing global energy needs have forced alternative energy technologies into the mainstream with challenges of balancing our current energy needs with oil production and developing methods to reduce dependence on fossil fuels. Currently, there is a great deal of research on using ILs in such technologies. For example, batteries and capacitors can be improved by ILs because of their low volatility and high charge concentration, allowing

them to replace many of the organic solvent-based systems in existence today. In addition, their large electrochemical windows provide a broader range of energy that can be stored and used. In conjunction with solar energy, ILs suggest devices where both electrolyte and photoreactive material are housed by the same medium. The depletion of natural resources, increase of carbon footprints, and the threat of biomass accumulation will all be of the past when the unbounded potential of ILs becomes reality. It is our responsibility to not only advance technology but to protect life itself.

Bibliography

- [1] R. D. Rogers and K. R. Seddon. Ionic liquids - solvents of the future? *Science*, 302:792–793, 2003.
- [2] N. V. Plechkova and K. R. Seddon. Applications of ionic liquids in the chemical industry. *Chem. Soc. Rev.*, 37:123–150, 2008.
- [3] M. Petkovic, K. R. Seddon, L. P. N. Rebelo, and C. S. Pereira. Ionic liquids: a pathway to environmental acceptability. *Chem. Soc. Rev.*, 40:1383–1403, 2011.
- [4] H. Jin, X. Li, and M. Maroncelli. Heterogeneous solute dynamics in room-temperature ionic liquids. *J. Phys. Chem. B*, 111:13473–13478, 2007.
- [5] M. Maroncelli, X.-X. Zhang, M. Liang, D. Roy, and N. P. Ernsting. Measurements of the complete solvation response of coumarin 153 in ionic liquids and the accuracy of simple dielectric continuum predictions. *Faraday Discuss.*, 154:409–424, 2012.
- [6] J. A. Ingram, R. S. Moog, N. Ito, R. Biswas, and M. Maroncelli. Solute rotation and solvation dynamics in a room-temperature ionic liquid. *J. Phys. Chem. B*, 107:5926–5932, 2003.
- [7] N. Ito, S. Arzhantsev, M. Heitz, and M. Maroncelli. Solvation dynamics and rotation of coumarin 153 in alkylphosphonium ionic liquids. *J. Phys. Chem. B*, 108:5771–5777, 2004.
- [8] A. M. Funston, T. A. Fadeeva, J. F. Wishart, and E. W. Castner, Jr. Fluorescence probing of temperature-dependent dynamics and friction in ionic liquid local environments. *J. Phys. Chem. B*, 111:4963–4977, 2007.

- [9] P. K. Mandal, N. Sarkar, and A. Samanta. Excitation-wavelength-dependent fluorescence behavior of some dipolar molecules in room-temperature ionic liquids. *J. Phys. Chem. A*, 108:9048–9053, 2004.
- [10] A. Paul, P. K. Mandal, and A. Samanta. On the optical properties of the imidazolium ionic liquids. *J. Phys. Chem. B*, 109:9148–9153, 2005.
- [11] Z. Hu and C. J. Margulis. Room-temperature ionic liquids: Slow dynamics, viscosity, and the red edge effect. *Acc. Chem. Res.*, 40(11):1097–1105, 2007.
- [12] Z. H. Hu and C. J. Margulis. Heterogeneity in a room-temperature ionic liquid: Persistent local environments and the red-edge effect. *Proc. Natl. Acad. Sci. U. S. A.*, 103:831–836, 2006.
- [13] Z. H. Hu and C. J. Margulis. A study of the time-resolved fluorescence spectrum and red edge effect of an in a room-temperature ionic liquid. *J. Phys. Chem. B*, 110:11025–11028, 2006.
- [14] K. Sahu, S. J. Kern, and M. A. Berg. Heterogeneous reaction rates in an ionic liquid: Quantitative results from two-dimensional multiple population-period transient spectroscopy. *J. Phys. Chem. A*, 115:7984–7993, 2011.
- [15] C. Khurmi and M. A. Berg. Dispersed kinetics without rate heterogeneity in an ionic liquid measured with multiple population-period transient spectroscopy. *J. Phys. Chem. Lett.*, 1:161–164, 2010.
- [16] J. B. Issa, A. S. Salameh, Jr. E. W. Castner, J. F. Wishart, and S. S. Isied. Conformational analysis of the electron-transfer kinetics across oligoproline peptides using N,N-Dimethyl-1,4-benzenediamine donors and pyrene-1-sulfonyl acceptors. *J. Phys. Chem. B*, 111:6878–6886, 2007.
- [17] L. D. Zusman. Outer-sphere electron transfer in polar solvents. *Chem. Phys.*, 49:295–304, 1980.
- [18] A. Triolo, O. Russina, H.-J. Bleif, and E. Di Cola. Nanoscale segregation in room temperature ionic liquids. *J. Phys. Chem. B*, 111:4641–4644, 2007.

- [19] A. Triolo, O. Russina, B. Fazio, R. Triolo, and E. DiCola. Morphology of 1-alkyl-3-methylimidazolium hexafluorophosphate room temperature ionic liquids. *Chem. Phys. Lett.*, 457:362–365, 2008.
- [20] O. Russina, A. Triolo, L. Gontrani, R. Caminiti, D. Xiao, L. G. Hines, Jr., R. A. Bartsch, E. L. Quitevis, N. Pleckhova, and K. R. Seddon. Morphology and intermolecular dynamics of 1-alkyl-3-methylimidazolium bis(trifluoromethane)sulfonylamide ionic liquids: structural and dynamic evidence of nanoscale segregation. *J. Phys. Condens. Matter*, 21:424121, 2009.
- [21] C. Hardacre, J. D. Holbrey, S. E. J. McMath, D. T. Bowron, and A. K. Soper. Structure of molten 1,3-dimethylimidazolium chloride using neutron diffraction. *J. Chem. Phys.*, 118:273–278, 2003.
- [22] J. N. Canongia Lopes and A. A. H. Padua. Nanostructural organization in ionic liquids. *J. Phys. Chem. B*, 110:3330–3335, 2006.
- [23] A. A. H. Pádua, M. F. Costa Gomes, and J. N. A. Canongia Lopes. Molecular-solutes in ionic liquids: A structural perspective. *Acc. Chem. Res.*, 40:1087–1096, 2007.
- [24] S. M. Urahata and M. C. C. Ribeiro. Structure of ionic liquids of 1-alkyl-3-methylimidazolium cations: A systematic computer simulation study. *J. Chem. Phys.*, 120:1855–1863, 2004.
- [25] C. S. Santos, N. S. Murthy, G. A. Baker, and E. W. Castner, Jr. X-ray scattering from ionic liquids with pyrrolidinium cations. *J. Chem. Phys.*, 134:121101, 2011.
- [26] A. Triolo, O. Russina, R. Caminiti, H. Shirota, H. Y. Lee, C. S. Santos, N. S. Murthy, and E. W. Castner, Jr. Comparing intermediate range order for alkyl- vs. ether-substituted cations in ionic liquids. *Chem. Comm.*, 48:4959–4961, 2012.
- [27] A. Mele, C. D. Tran, and S. H. D. Lacerda. The structure of a room-temperature ionic liquid with and without trace amounts of water: The role of C-H center dot

- center dot center dot O and C-H center dot center dot center dot F interactions in 1-n-butyl-3-methylimidazolium tetrafluoroborate. *Angew. Chem., Int. Ed.*, 42:4364–4366, 2003.
- [28] F. Castiglione, M. Moreno, G. Raos, A. Famulari, A. Mele, G. B. Appetecchi, and S. Passerini. Structural organization and transport properties of novel pyrrolidinium-based ionic liquids with perfluoroalkyl sulfonylimide anions. *J. Phys. Chem. B*, 113:10750–10759, 2009.
- [29] General discussion. *Faraday Discuss.*, 154:189–220, 2012.
- [30] K. R. Seddon, A. Stark, and M. J. Torres. Influence of chloride, water, and organic solvents on the physical properties of ionic liquids. *Pure Appl. Chem.*, 72:2275–2287, 2000.
- [31] S. N. Baker, G. A. Baker, C. A. Munson, F. Chen, E. J. Bukowski, A. N. Cartwright, and F. V. Bright. Effects of solubilized water on the relaxation dynamics surrounding 6-propionyl-2-(N,N-dimethylamino)naphthalene dissolved in 1-butyl-3-methylimidazolium hexafluorophosphate at 298 K. *Ind. Eng. Chem. Res.*, 42:6457–6463, 2003.
- [32] H. V. R. Annapureddy, Z. Hu, J. Xia, and C. J. Margulis. How does water affect the dynamics of the room-temperature ionic liquid 1-hexyl-3-methylimidazolium hexafluorophosphate and the fluorescence spectroscopy of coumarin-153 when dissolved in it? *J. Phys. Chem. B*, 112:1770–1776, 2008.
- [33] S. Baldelli. Influence of water on the orientation of cations at the surface of a room-temperature ionic liquid: a sum frequency generation vibrational spectroscopic study. *J. Phys. Chem. B*, 107:6148–6152, 2003.
- [34] L. Cammarata, S. G. Kazarian, P. A. Salter, and T. Welton. Molecular states of water in room temperature ionic liquids. *Phys. Chem. Chem. Phys.*, 3:5192–5200, 2001.

- [35] C. G. Hanke and R. M. Lynden-Bell. A simulation study of water-dialkylimidazolium ionic liquid mixtures. *J. Phys Chem. B*, 107:10873–10878, 2003.
- [36] N. E. Heimer, R. E. Del Sesto, and R. Carper. Evidence for spin diffusion in a H,H-NOESY study of imidazolium tetrafluoroborate ionic liquids. *Magn. Reson. Chem.*, 42:71–75, 2004.
- [37] P. J. Dupont, A. Z. Suarez, R. F. De Souza, R. A. Burrow, and J. P. Kintzinger. C–H- π interactions in 1-n-butyl-3-methylimidazolium tetrphenylborate molten salt: Solid and solution structures. *Chem. Eur. J.*, 6:2377–2381, 2000.
- [38] H. K. Kashyap, H. V. R. Annapureddy, F. O. Raineri, and C. J. Margulis. How is charge transport different in ionic liquids and electrolyte solutions? *J. Phys. Chem. B*, 115:13212–13221, 2011.
- [39] B. M. Krieger, H. Y. Lee, T. J. Emge, J. F. Wishart, and E. W. Castner Jr. Ionic liquids and solids with paramagnetic anions. *Phys. Chem. Chem. Phys.*, 12:8919–8925, 2010.
- [40] P. Brown, A. Bushmelev, C. P. Butts, J. Cheng, J. Eastoe, I. Grillo, R. K. Heenan, and A. M. Schmidt. Magnetic control over liquid surface properties with responsive surfactants. *Angew. Chem.*, 51:2414–2416, 2012.

Appendix A

Appendix

A.1 Details of the TCSPC data analysis

Nonlinear least-squares (NLS) fit and sum of Gaussian (G-) function fit regularized with an entropy function were done on MATLAB¹ with the optimization program, `fmincon.m`, where active set method was dominantly used. Igor Pro² method that has been used and explained previously³ was used to confirm the NLS fitting on MATLAB. NLS fitting was done with four and five exponentials so that the following reduced- χ^2 value is minimized:

$$\chi_R^2 = \frac{1}{N - N_p} \sum_{i=1}^N \frac{(y(t_i - s) - I(t_i))^2}{I(t_i)} \quad (\text{A.1})$$

where

$$I(t_i) = \sum_{j=1}^{n_e} A_j \int_0^{t_f} e^{-(t_i-p)/\tau_j} R(p) dp + B \quad (\text{A.2})$$

represents the fluorescence output at t_i predicted by a multi-exponential function (MEF) model convoluted with the instrument response function (IRF) and biased by a constant; s denotes a time shift that has to be optimized; $N_p = 2n_e + 2$ is the number of parameters to optimize. The results of NLS fit were used to generate the *a priori* distribution for the entropy function and initial parameters of the G-functions. Although satisfactory reduced- χ^2 value can be achieved for NLS fit with just four exponential fits, all the calculations were done with five exponential fits because it generally gives a better MEM-Gaussian distribution fitting sometimes with an extra non-meaningful decay rate that has negligible amplitude, for it forces the fitting to converge to a certain

distribution that conforms to the initial NLS fit.

The MEM-Gaussian distribution fit minimizes the following function:

$$-S + \alpha \chi_R^2 \quad (\text{A.3})$$

where the Chi2 term is defined with

$$I(t_i) = \int_{-\infty}^{\infty} g(\log \tau) \left(\int_0^{t_f} e^{-(t_i-p)/\tau} R(p) dp \right) d \log \tau + B \quad (\text{A.4})$$

and the entropy term is defined as

$$S = \sum_{m=1}^M (g(\log \tau_m) - \hat{g}_m - g(\log \tau_m) \ln(g(\log \tau_m)/\hat{g}_m)) \quad (\text{A.5})$$

with \hat{g} as the *prior* distribution of g . The distribution function g was assumed to be represented by a sum of G-functions such that

$$g(\log \tau) = \sum_{j=1}^{n_e} A_j \exp \left(-\frac{1}{2} \frac{(\log \tau - \log \tau_{mean,j})^2}{\sigma_j^2} \right). \quad (\text{A.6})$$

the calculations were done at 100 points within the $\log \tau$ range (in this case from -2 to 2). The initial $\tau_{mean,j}$ values were set to be the τ value from the NLS fit; the initial values of σ_j was set to be user's choice such that $\sigma_j = (\log \tau_{max} - \log \tau_{min})/W = 4/W$; and the amplitudes were initially set so that the area of each G-function is equivalent to the height of the corresponding exponential function. The *priori* distribution was also given by a sum of G-functions with initial parameters described above except the W value. The MEM-Gaussian distribution fitting is different from the conventional MEM fitting in that most MEM fittings set initial *a priori* function to be a constant. Since we have *a priori* knowledge of the rate distribution, it would make more sense to start with such function, however, we made the *prior* function somewhat wide (setting $W = 20$) to make sure that it is not biasing the fitting too much. Optimum parameters of the G-functions plus B and s were found using `fmincon.m` until (A.3) is minimized.

Bibliography

- [1] MATLAB 7.10.0. MATLAB version 7.10.0. Natick, Massachusetts: The MathWorks Inc., 2010., **2010**.
- [2] Igor Pro 6.04. Wavemetrics Igor Pro 5.04b Edition. Wavemetrics, Inc. Lake Oswego, OR, **2009**.